Title
Manipulating Light-Matter Interactions in Photopolymerization-based Microscale 3D Printing

Author
You, Shangting

Publication Date
2019

UNIVERSITY OF CALIFORNIA SAN DIEGO

Manipulating Light-Matter Interactions in Photopolymerization-based Microscale 3D Printing

A dissertation submitted in partial satisfaction of the
Requirements for the degree Doctor of Philosophy

in

Nanoengineering

by

Shangting You

Committee in charge

Professor Shaochen Chen, Chair
Professor Shengqiang Cai
Professor Zhaowei Liu
Professor Donald Sirbuly
Professor Liangfang Zhang

2019

The Dissertation of Shangting You is approved, and it is acceptable in quality and form for publication on microfilm and electronically:

Chair

University of California San Diego

2019

TABLE OF CONTENTS

SIGNATURE PAGE iii

TABLE OF CONTENTS iv

LIST OF ABBREVIATIONS viii

LIST OF FIGURES x

LIST OF TABLES xii

ACKNOWLEDGEMENTS xiii

VITA xv

ABSTRACT OF DISSERTATION xvii

Chapter 1 Introduction 1

1.1 Motivation 1

1.2 3D Printing Techniques 2

1.3 Photopolymerization-based 3D Printing 3

1.3.1 Point-scanning Methods 4

1.3.2 Plane-projecting Methods 7

1.3.3 Volumetric Photopolymerization Methods 11

1.3.4 Summary 13

1.4 Fabrication Resolution of Plane-projecting Methods 14

1.4.1 Diffraction Limit 15

1.4.2 Optical Aberrations 16

1.4.3 Material Absorption 16

1.4.4 Light Scattering 17

1.4.5 Molecular diffusion 18

1.5 Research Objectives 19

Acknowledgements 20

Reference 20

Chapter 2 High-fidelity 3D Printing using Flashing Photopolymerization 25

Abstract 25

2.1 Introduction 25

2.2 High Fidelity 3D Printing 29

2.3 Theory and Mechanism 33

2.3.1 Material Scattering 33

2.3.2 Photopolymerization Kinetics 35

2.4 Conclusions 38

2.5 Experimental Section 39

Acknowledgements 41

Supplementary Information 42

Reference 47

Chapter 3 Mitigating Scattering Effects Using Machine Learning 51

Abstract 51

3.1 Introduction 51

3.2 Experimental Setup 53

3.2.1 Modeling DLP-based 3D Printing 53

3.2.2 Neural Network 55

3.3 Methods 57

3.4 Results and Discussion 61

3.5 Conclusions 66

Acknowledgements 67

Supplementary Information 67

Reference 71

Chapter 4 Projection Printing using Patterned Evanescent Field 75

Abstract 75

4.1 Introduction 75

4.2 Results and Discussion 78

4.2.1 Polymerization Effect of Evanescent Field 78

4.2.2 Direct Printing System Setup 80

4.2.3 Holography Algorithm 82

4.2.4 Surface Topography of the Printed Patterns 85

4.3 Methods 86

4.4 Conclusions 87

Acknowledgements 88

Reference 89

Chapter 5 Conclusions and Future Perspectives 92

5.1 Conclusions 92

5.2 Perspectives 93

Reference 95

LIST OF ABBREVIATIONS

2PP: two-photon polymerization

AA: adaptive-additive

AI: artificial intelligence

CGH: computer generated hologram

CLIP: continuous liquid interface production

CT: computed tomography

CW: continuous wave

DLP: digital light processing

DMD: digital micromirror device

FPP: flashing photopolymerization

FTIR: Fourier-transform infrared

GS: Gerchberg–Saxton

IAD: inverse adding-doubling

IR: infrared

LAP: lithium phenyl-2,4,6-trimethylbenzoylphosphinate

LCD: liquid crystal display

LED: light emitting diode

MRAF: mixed-region amplitude freedom

NA: numerical aperture

NN: neural network

PDMS: polydimethylsiloxane

PEGDA: poly(ethylene glycol) diacrylate

SEM: scanning electron microscope

SLM: spatial light modulator

STED: stimulated emission depletion

TEMPO: 2,2,6,6-tetramethylpiperidine 1-oxyl

TIR: total internal reflection

UV: ultraviolet

LIST OF FIGURES

Figure 1.1| Typical setups of various types of photopolymerization-based 3D printing techniques……………………………………………………………………………………4

Figure 2.1| Flashing photopolymerization 3D printing………………………………………..30

Figure 2.2| Resolution test for the CW exposure mode and FPP exposure mode………………..33

Figure 2.3| Scattering changes during polymerization…………………………………………34

Figure 2.4| PEGDA photopolymerization simulation of the CW exposure mode and the FPP exposure mode…………………………………………………………………...……38

Figure 2.S1| Zoom-in view of images in Figure 2.2……………………………………………42

Figure 2.S2| Appearance of the slab samples…………………………………………………43

Figure 2.S3| Optical setup for visualizing the opacification during polymerization……….….45

Figure 2.S4| Scattering changes during polymerization………………………………………45

Figure 3.1| Schematic of the 3D printer and the printed structures……………………………55

Figure 3.2| Data flow and architecture of the neural network…………………………………56

Figure 3.3| Comparison of the targets, the NN-suggested masks, and the microscopic images of the printed structures……………………………………………………..…………………62

Figure 3.4| Printed structures using NN-suggested masks and identical masks ………………...64

Figure 3.5| Printed structures using NN-suggested masks and identical masks …………..……..65

Figure 3.S1| Comparison between 3D printing of non-scattering material and scattering material……………………………………………………………………………………..68

Figure 3.S2| Examples of the training digital masks…………………………………………...69

Figure 3.S3| Comparison between the two-NN design and the master-only design …………... 70

Figure 3.S4| Plot of errors versus episodes……………………………………………………71

Figure 4.1| Comparison of the polymer pattern thickness between the propagating field and the evanescent field………………………………………………………………………………..80

Figure 4.2| The optical setup of the ultrathin surface patterning system……………………...81

Figure 4.3| Block diagram of the 3D-MRAF algorithm………………………………………85

Figure 4.4| The optical profiler images of the patterned structure…………………………………...86

LIST OF TABLES

Table 2.1| Material properties and kinetic parameters of PEGDA ………………………….…..40

Table 2.S1| Free radical generation rates and corresponding illumination intensity……………..47

ACKNOWLEDGEMENTS

I would like to sincerely thank many people, without whom this thesis would not have been possible.

First, it has really been a pleasure and honor to work for Dr. Shaochen Chen, who always inspires and supports my ideas. And I want to thank Dr. Wei Zhu for his guidance.

Then, I would like to thank my dissertation committee members, Dr. Liangfang Zhang, Dr. Donald Sirbuly, Dr. Zhaowei Liu, Dr. Shengqiang Cai, for their time and comments.

I would also like to thank all the current and former members in our lab including Dr. Pengrui Wang, Dr. Xuanyi Ma, Dr. David Berry, Dr. Claire Yu, Dr. John Warner, Dr. Justin Liu, Dr. Jiawen Li, Peter Chung, Henry Hwang, Kathleen Miller, Jacob Schimelman, Min Tang, Jiaao Guan, Zheng Zhong, Wisarut Kiratitanaporn, Dai Xue, Haixu Shen, and Jeffrey Alido.

I would also like to thank my collaborators, including Dr. Daniel Wanspraseurt and Dr. Hao Su.

Last, I would like to thank all my friends and family members for their love and support.

Chapter 1, in part, is adapted from the published book chapter, “Microstereolithography”, S. You, K. Miller, S. Chen. *Biofabrication and 3D Tissue Modeling*, 2019. The dissertation author was the primary investigator and author of this book chapter.

Chapter 2, in full, is a reprint of the published article, “High-fidelity 3D printing using flashing photopolymerization”, S. You, P. Wang, J. Schimelman, H.H. Hwang, S. Chen. *Additive Manufacturing*, 2019. The dissertation author was the primary investigator and author of this paper. This work was supported in part by National Institutes of Health (R21AR074763, R33HD090662, and R01EB021857) and National Science Foundation (NSF) (CMMI-1644967). Part of the work is performed at San Diego Nanotechnology Infrastructure (SDNI) of UCSD, a member of the

National Nanotechnology Coordinated Infrastructure (NNCI), which is supported by NSF (Grant ECCS-1542148).

Chapter 3, in full, is a reprint of the unpublished article, “Mitigating scattering effects in light-based 3D printing using machine learning”, S. You, J. Guan, J. Alido, H.H. Hwang, L. Kwe, R. Ro, H. Su, S. Chen. The dissertation author was the primary investigator and author of this paper. This work was supported in part by National Institutes of Health (R01EB021857, R21 AR074763, R33HD090662) and National Science Foundation (CMMI-1907434). Part of the work is performed at San Diego Nanotechnology Infrastructure (SDNI) of UCSD, a member of the National Nanotechnology Coordinated Infrastructure (NNCI), which is supported by NSF (Grant ECCS-1542148).

Chapter 4, in full, is a reprint of the published article, “Projection Printing of Ultrathin Structures with Nanoscale Thickness Control”, S. You, W. Zhu, P.Wang, S.Chen. *ACS Applied Materials and Interfaces*, 2019. The dissertation author was the primary investigator and author of this paper. This work was supported in part by National Institutes of Health (R21HD090662, R01EB021857) and National Science Foundation (CMMI-1547005 and CMMI-1644967). Part of the work is performed at San Diego Nanotechnology Infrastructure (SDNI) of UC San Diego, a member of the National Nanotechnology Coordinated Infrastructure (NNCI), which is supported by the National Science Foundation (Grant ECCS-1542148).

VITA

2015 Bachelor of Science, Zhejiang University

2016 Master of Science, University of California San Diego

2019 Doctor of Philosophy, University of California San Diego

PUBLICATIONS

[1] **S. You**, C. Kuang, Z. Rong, X. Liu, Eliminating deformations in fluorescence emission difference microscopy, Opt. Express. 22 (2014) 26375.

[2] **S. You**, C. Kuang, Z. Rong, X. Liu, Z. Ding, Isotropic superresolution imaging for fluorescence emission difference microscopy, Appl. Opt. 53 (2014) 7838.

[3] B. Ge, Y. Ma, C. Kuang, D. Zhang, K.C. Toussaint, **S. You**, X. Liu, Resolution-enhanced surface plasmon-coupled emission microscopy, Opt. Express. 23 (2015) 13159.

[4] L. Xue, C. Kuang, Y. Fang, **S. You**, Y. Ma, X. Liu, Axial nanodisplacement measurement based on the double-helix point spread function generated using radially polarized beams with vortex phase modulation, Jpn. J. Appl. Phys. 54 (2015) 082501.

[5] **S. You**, C. Kuang, K.C. Toussaint, R. Zhou, X. Xia, X. Liu, Iterative phase-retrieval method for generating stereo array of polarization-controlled focal spots, Opt. Lett. 40 (2015) 3532.

[6] **S. You**, C. Kuang, S. Li, X. Liu, Z. Ding, Three-dimensional super-resolution imaging for fluorescence emission difference microscopy, AIP Adv. 5 (2015) 084901.

[7] S. Liu, **S. You**, Y. Fang, Y. Wang, C. Kuang, X. Liu, Effects of polarization and phase modulation on the focal spot in 4Pi microscopy, J. Mod. Opt. 63 (2016) 1145–1157.

[8] **S. You**, C. Kuang, B. Zhang, Resolution criteria in double-slit microscopic imaging experiments, Sci. Rep. 6 (2016) 33764.

[9] D.B. Berry, **S. You**, J. Warner, L.R. Frank, S. Chen, S.R. Ward, P. Reviewed, S. Diego, S. Diego, E. Engineers, A 3D Tissue-Printing Approach for Validation of Diffusion Tensor Imaging in Skeletal Muscle, Tissue Eng. Part A. 23 (2017) 980–988.

[10] **S. You**, J. Li, W. Zhu, C. Yu, D. Mei, S. Chen, Nanoscale 3D printing of hydrogels for cellular tissue engineering, J. Mater. Chem. B. 6 (2018) 2187–2197.

[11] W. Zhu, S.-H. Pyo, P. Wang, **S. You**, C. Yu, J. Alido, J. Liu, Y. Leong, S. Chen, Three-Dimensional Printing of Bisphenol A-Free Polycarbonates, ACS Appl. Mater. Interfaces. 10 (2018) 5331–5339.

[12] W. Zhu, K.R. Tringale, S.A. Woller, **S. You**, S. Johnson, H. Shen, J. Schimelman, M. Whitney, J. Steinauer, W. Xu, T.L. Yaksh, Q.T. Nguyen, S. Chen, Rapid continuous 3D printing of customizable peripheral nerve guidance conduits, Mater. Today. 21 (2018) 951–959.

[13] **S. You**, K. Miller, S. Chen, Microstereolithography, in: Biofabrication and 3D Tissue Modeling, 2019: pp. 1–21.

[14] **S. You**, W. Zhu, P. Wang, S. Chen, Projection Printing of Ultrathin Structures with Nanoscale Thickness Control, ACS Appl. Mater. Interfaces. 11 (2019) 16059–16064.

[15] **S. You**, P. Wang, J. Schimelman, H.H. Hwang, S. Chen, High-fidelity 3D printing using flashing photopolymerization, Addit. Manuf. 30 (2019) 100834.

[16] **S. You**, J. Guan, J. Allido, H.H. Hwang, R. Yu, L. Kwe, H. Su, S. Chen. Mitigating scattering effects in light-based 3D printing using machine learning. (under review)

[17] D. Wangpraseurt, **S. You**, F. Azam, G. Jacucci, O. Gaidarenko, M. Hildebrand, M. Kuhl, AG. Smith, MP. Davey, DD. Deheyn, S. Chen, S. Vignolini. Bionic printed corals. (under review)

[18] C. Yu, K. Miller, J. Schimelman, P. Wang, W. Zhu, X. Ma, M. Tang, **S. You**, D. Lakshmipathy, F. He, S. Chen. An integrated 3D bioprinting and orthogonal bioconjugation approach for precision tissue engineering. (under review)

[19] HH. Hwang, **S. You**, X. Ma, L. Kwe, G. Victorine, N. Lawrence, H. Shen, X. Wan, W. Zhu, S. Chen. High-throughput 3D-bioprinting in well plates. (under review)

US PATENTS

[1] **S. You**, S. Chen. High-fidelity 3D printing using flashing photopolymerization. (provisional disclosure)

[2] S. Chen, D. Deheyn, **S. You**, D. Wangpraseurt. Bionic 3D printed corals. (provisional disclosure)

ABSTRACT OF DISSERTATION

Manipulating Light-Matter Interactions in Photopolymerization-based Microscale 3D Printing

by

Shangting You

Doctor of Philosophy in Nanoengineering

University of California San Diego, 2019

Professor Shaochen Chen, Chair

Functional microdevices such as micro-robotics, tissue engineering scaffolds, and lab-on-a-chip are finding promising application across many industries, such as energy, environment, medicine, defense, and consumer products, due to their high performance and miniaturized size. These devices often have complex 3D geometry across multiple length scales to achieve their functionalities, and their performance is strongly dependent on the accuracy and precision of these features.

Microscale 3D printing is an emerging free-form additive manufacturing technique for

fabricating functional microdevices. Among various types of 3D printing methods, photopolymerization-based 3D printing is the most promising technique, because of its fine resolution, fast speed, and ability to fabricate structures with high quality.

Despite numerous instances of successful fabrication of functional microdevices using photopolymerization-based 3D printing, this technique still faces many challenges to produce micro-architectures in high fidelity and high resolution. It is important to study and refine our ability to manipulate light-matter interactions in the photopolymerization process during printing.

One significant challenge in fabricating microdevices using photopolymerization-based 3D printing is that the functional materials used in their construction can be light scattering, thus deteriorating final fabrication fidelity and resolution. In this dissertation, two methods are developed to overcome this issue: one method uses flashing photopolymerization approach to avoid the effect of light scattering, and the other method uses a machine learning approach to compensate for the effect of light scattering.

Furthermore, photopolymerization-based 3D printing technique has an issue of anisotropic resolution, where the axial resolution can be much worse than the lateral resolution due to the nature of light's propagation. To address this, a projection printing method using patterned evanescent fields was developed. This approach could be a promising solution to improving the axial resolution.

Chapter 1 Introduction

1.1 Motivation

Functional microdevices, such as microrobots,[1–3] microfluidic devices,[4–6] microsensors,[7–9] electronic and photonic devices,[10–12] tissue engineering scaffolds,[13–17] drug delivery vessels [18,19] are having increasingly significant impact on many important industrial sectors such as energy, environment, defense, medicine, and consumer products. They are promising tools for various applications because of their high performance and miniaturized size. These devices often have complex 3D geometry across multiple length scales to achieve their functionalities, and their performance is strongly dependent on the accuracy and precision of their features.

To date, a variety of technologies have been developed to fabricate functional parts and devices. However, precise 3D fabrication at micro- and nano-scale remains challenging simply due to the size of the desired features. Traditional fabrication technologies such as machining is commonly used in macro-scale fabrication, however, it is not adequate for micro and nanoscale fabrication. Molding can rapidly replicate either macro-scale and micro-scale structures, however they are limited to simple 3D geometries without overhanging or hollow structures. Modern micro- and nano-scale fabrication technologies such as photolithography, soft lithography, physical vapor deposition, chemical vapor deposition, electron beam lithography, focused ion beam lithography, are often 2D in nature for thin film and surface patterning.

3D printing has emerged as a powerful additive free-form 3D fabrication technology in the past decades because of its low cost, simplicity, and versatility. Additionally, this technology does not employ extreme environmental conditions such as vacuum, high temperature, or ionizing radiation, and is thus capable of handling delicate materials such as hydrogels and biological proteins. Among various types of 3D printing techniques, photopolymerization-based 3D printing stands out because of its fine resolution, fast fabrication speed, and good structural quality of the resultant constructs.

In order to meet the growing requirement of precise fabrication of functional microdevices with micro- and nano-scale features, fabrication fidelity and resolution of photopolymerization-based 3D printing need to be further improved. Therefore, the following chapters will be devoted to developing novel approaches to study and manipulate light-matter interaction in photopolymerization-based micro 3D printing. These studies aim at developing advanced methods to improve the fabrication fidelity and resolution of photopolymerization-based micro 3D printing.

1.2 3D Printing Techniques

Generally, there are two additive 3D fabrication approaches. One is to selectively deposit the building materials to the desired location, and the other is to selectively deliver energy to the desired location to trigger phase changes in a building material.

Typical 3D printing techniques that selectively deposit the building materials to the desired location, such as fused filament fabrication,[20] powder bed 3D printing,[21] and ink-jet 3D printing,[22] utilize an inkjet head or a nozzle, which can move in 3D and precisely deliver the material to the desired location in a drop-by-drop or strand-by-strand manner.[23] The deposited material can quickly solidify to support the entire structure. By scanning through the designed object, a 3D structure is thus fabricated. However, these methods come with some disadvantages. The inkjet head or nozzle limits the size of a single drop or strand. As a result, the fabrication resolution is typically limited to around 50 microns. Interfaces between adjacent drops or strands are inevitable in these methods, thus the structural quality is compromised. In addition, when using this technique to fabricate cell-laden biomedical microdevices such as tissue engineering scaffolds, the shear stress caused by the nozzle can lower the cell viability.[24]

3D printing techniques that selectively deliver energy to the desired location typically use light energy to induce sintering,[25] photopolymerization/photocrosslinking,[24] photoreduction,[26] and so on. The most common techniques are based on photopolymerization. Photopolymerization-based 3D printing utilizes photosensitive materials, which can polymerize and solidify upon light exposure. By spatially controlling the exposure dose, a desired 3D structure can be fabricated, and because light can be precisely manipulated on the micro- and nano-scale, photopolymerization-based 3D printing can therefore achieve micron or sub-micron scale resolution. In addition, when printing biomedical microdevices in this manner, much higher cell viabilities can be achieved.[24] Therefore, photopolymerization-based 3D printing techniques have been widely used for fabricating functional microdevices.

1.3 Photopolymerization-based 3D Printing

Photopolymerization-based 3D printing is a light-assisted 3D additive fabrication technology. This technology utilizes photosensitive materials, which can solidify upon light exposure. The light to induce photopolymerization is typically ultraviolet (UV) or blue light. By spatially controlling the exposure dose, a desired 3D structure can be fabricated.

The prevailing polymerization mechanism in photopolymerization is based on free radical photopolymerization,[27] where free radicals interact with reactive end groups to form polymers. The basic structure of the active group is $CH_2=CR_1R_2$, as the π-bond in the carbon-carbon double bond allows it to be rearranged when exposed to a free radical. Photoinitiators are used to create free-radicals upon light exposure. Once initiated, the active polymer chain begins to propagate until termination.

There are different methods to deliver light energy to the desired position, based on which we can classify the photopolymerization-based 3D printing techniques into three categories: point-scanning methods, plane-projection methods, and volumetric photopolymerization methods.

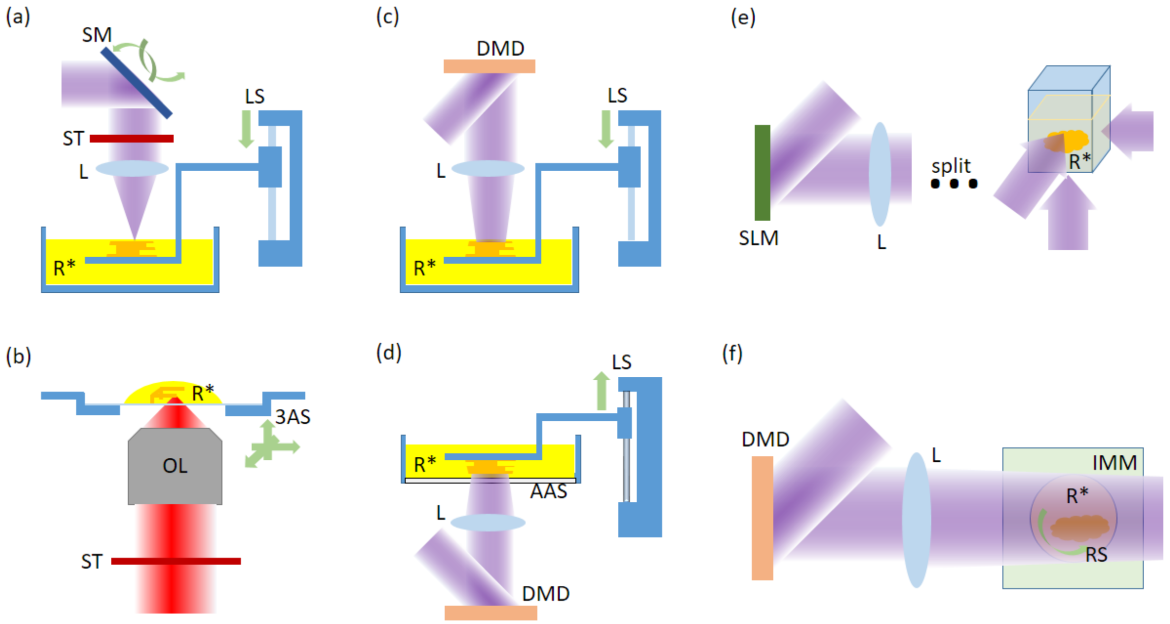

Figure 1.1| Typical setups of various types of photopolymerization-based 3D printing techniques. (a) Single-photon point-scanning method (side view). (b) Two-photon point-scanning method (side view). (c) Layer-by-layer plane-projection method (side view). (d) Continuous plane projection method (side view). (e) Holographic volumetric photopolymerization method (side view). (f) Tomographic volumetric photopolymerization method (top view). SM: scanning mirrors; ST: shutter; L: lens; OL: high numerical aperture objective lens; R*: photosensitive resin; LS: linear stage; 3AS: 3-axis stage; RS: rotary stage; DMD: digital micromirror device; SLM: spatial light modulator; AAS: anti-adhesion substrate; IMM: refractive-index-matched medium.

1.3.1 Point-scanning Methods

The idea of point-scanning methods is to use a lens to focus the beam, thus photopolymerization happens only at the focal point. A desired 3D structure can be made by scanning the focal point through the volume of the whole design. The most popular point-scanning methods include single-photon point-scanning method and two-photon point-scanning method, and recently super-resolution point-scanning method has also been reported.

Single-photon point-scanning method

As shown in Figure 1.1(a), typical single-photon point-scanning method uses a lens to focus the UV laser beam. The focused UV laser then induces photopolymerization at its focal point. A set of X-Y Galvo scanning mirrors are used to steer the beam to scan on the plane, and a linear stage control the z position of the fabrication platform. The on/off state of the laser beam is manipulated by a computer-controlled shutter. Hence, photopolymerization can happen only at desired positions. During fabrication, the platform first moves to a position which is slightly under the liquid surface, then translates in a 2D horizontal plane, thus forming a thin layer of 2D solid structure made from the liquid solution. Then the platform moves the structure down to a certain distance in z-direction, allowing a thin layer of unpolymerized solution to cover the top of the polymerized structure. Another round of 2D translational scanning follows, and a new layer of 2D structure is stacked on top of the previous layer. Therefore, a 3D structure can be fabricated by this layer-by-layer scanning process.[28]

Two-photon point-scanning method

Two-photon point-scanning method utilizes two-photon photopolymerization to polymerize prepolymer. Two-photon polymerization refers to photopolymerization initiated by two-photon absorption. The wavelength of the photons used in two-photon polymerization is twice as long as in single-photon polymerization. Therefore, near-infrared light is typically used in two-photon point-scanning method.

As shown in Figure 1.1(b), a two-photon photopolymerization system is typically built on a microscope platform, where a high numerical aperture microscope objective lens is used to tightly focus the laser beam, and the prepolymer is loaded on the 3-axis microscope platform. Two-photon polymerization requires extremely high power density. Thus an ultrafast pulsed laser should be used, and the laser beam should be tightly focused by a high numerical aperture objective lens.[29][30] Sub-micro resolution down to 100 nm can be achieved by two-photon stereolithography, which is much finer than single-photon stereolithography.

An important feature of two-photon point-scanning method is that it can establish a focal point inside the volume of a prepolymer solution, instead of being limited to the just the surface. The prepolymer solution, which consists of monomer and photoinitiator, has a high absorbance in UV range but very low absorbance in visible and near infrared (IR) range. As a result, unlike in single-photon point-scanning method where the UV light can only polymerize the surface of prepolymer solution; in two-photon stereolithography, the near IR light can penetrate into the prepolymer solution and induce two-photon polymerization at a point inside the solution. Compared to single-photon stereolithography, there is no invasive part dipping into the prepolymer. Therefore, solid state prepolymer solutions such as soft-baked negative photoresists are also applicable to this technique.

Super-resolution point-scanning method

Optical microscopy and lithography technologies are subjected to the diffraction limit due to the wave nature of light. Therefore, the resolution limit of these technologies was considered to be around half a wavelength for centuries. Although two-photon and multi-photon approaches are capable of reaching sub-diffraction-limited resolution, microscopy techniques with resolution far beyond the diffraction limit were not developed until the 1990s. These techniques, termed as super-resolution microscopy, include stimulated-emission-depletion microscopy (STED), photoactivated localization microscopy (PALM), structured illumination microscopy (SIM), and so on.[31–33]

Inspired by STED microscopy, STED-type super-resolution 3D printing methods have been developed.[34–37] In a typical STED-type super-resolution 3D printing setup, two beams are focused to the same point. Photopolymerization can be initiated by one beam, and be depleted by another. The depletion beam goes through a modulator, which is typically a 0-2π vortex phase plate, thus its focal spot is a donut-shaped spot; the focal spot of the initiation beam is a normal Airy spot. Because these two spots are overlapping, the peripheral area of the initiation focal spot is depleted by the depletion beam. Only the area at the center of the donut spot can be effectively initiated. Thus, the effective initiation area is reduced. Therefore, the fabrication resolution is improved.

Super-resolution stereolithography has pushed the fabrication resolution to around 50 nanometers. Recent research has even shown that a resolution of 9 nm was reached.[38]

1.3.2 Plane-projecting Methods

Photolithography is the most important technology in modern semiconductor industry. A typical projection-based exposure system for photolithography contains a UV light source, photomask, lens, and photoresist. The UV light is patterned by the photomask and is then projected onto the photoresist by a lens.

Recent advances of digital light processing (DLP) devices have allowed maskless photolithography. DLP devices include liquid crystal displays (LCD) and digital micromirror devices (DMD).

A DMD is a micro-electro-mechanical system (MEMS), which consists of millions of micro mirrors that can flip to two different angles. By flipping the mirrors, the incoming light can either be directed into the projection light path, or be deflected out of the projection light path. By individually controlling each micro mirror on the DMD chip, a desired pattern can be projected onto the photo-sensitive polymers by optical lenses.

Inspired by maskless photolithography, plane-projection methods using LCD or DMD were invented.[39,40] These methods polymerize a 2D plane at a time, and can produce 3D architecture in a layer-by-layer or continuous manner. Compared to the point-scanning methods, these plane-projection methods provide extremely fast fabrication speeds since it is a parallel process. A complex 3D structure on the millimeter scale can be fabricated in mere seconds. This high throughput feature is very attractive for industrial manufacturing.

Layer-by-layer plane-projection method

In a typical layer-by-layer plane-projection 3D printing setup, photopolymerization happens at the liquid-air interface. As shown in Figure 1.1(c), the prepolymer solution is loaded in a vat. The UV light is modulated by a DLP device and projected from the top of the vat. Hence, photopolymerization happens at the liquid-air interface. During fabrication, a motorized platform first moves to a position slightly under the liquid. A pattern is then loaded on the DLP device and projected onto the prepolymer solution, fabricating a 2D structure in one exposure. The platform then brings down the structure to allow a thin layer of unpolymerized liquid to cover the fabricated structure, and the DLP device loads a new mask for the next layer. It is then followed by another exposure to create another layer of 2D structure. By this layer-by-layer exposure process, a 3D structure is fabricated.

In order to achieve a high quality fabrication, the liquid-air interface should maintain good flatness. Therefore, the meniscus caused by surface tension and any ripples caused by motion should be avoided after the platform moves down to get ready for the next layer.

There are two ways to make a flat surface. One method is that, instead of directly moving to the desired z position, the platform first moves to a z position which is much lower than the target position, then rises back to the target position. This roundabout motion ensures the unpolymerized liquid can efficiently cover the polymerized structure. The liquid will calm down after a few seconds, making a flat surface for the next exposure. Another method is to use a recoating blade. The platform directly moves to the target position, then the recoating blade skims through the liquid surface to help making a thin layer of unpolymerized liquid on top of the fabricated structure. Both ways introduce a time interval between two exposures, therefore, it slows down the whole fabrication process, and also introduces visible "interfaces" between layers due to the discrete motion and exposure.[41]

Continuous plane-projection method

In the continuous plane-projection method, photopolymerization takes place at the liquid-substrate interface. [42,43] As shown in Figure 1.1(d), the prepolymer solution is loaded into a vat, and the UV light is modulated by the DLP device and projected from the bottom of the vat.[44] A transparent anti-adhesion substrate is installed at the bottom of the vat. During fabrication, the platform first moves to a position very close to the anti-adhesion substrate. After exposure, the polymerized structure fills the space between the platform and the anti-adhesion substrate, and adheres to the platform. The motorized platform then moves up to allow a thin layer of unpolymerized liquid to flow into the space above the substrate, and the mask of the next layer is loaded on the DLP device. A second layer of structure can then be fabricated by another exposure. Therefore, a new layer of polymer is fabricated beneath the structure, and eventually a 3D structure is printed in a continuous fashion.

Since the substrate helps to maintain good surface flatness, there is no time interval required between motion and exposure. Hence, the platform motion and UV exposure can both be performed in a continuous manner instead of a layer-by-layer manner. Thus, the fabrication time is significantly reduced. Furthermore, the "interface" between layers is eliminated, resulting in a smooth and layerless surface.

The key factor of continuous production is the anti-adhesion substrate. Fluorinated oil can prevent adhesion.[45] Since oxygen can inhibit photopolymerization,[46] a gas permeable membrane, such as polydimethylsiloxane (PDMS) or Teflon can also be a good anti-adhesion substrate. Simply applying a PDMS layer to passively supply oxygen is a common choice to fabricate small scale (< 10cm) structures.[47] To fabricate large scale (> 10cm) structures, actively supplying oxygen is necessary.[42]

The thickness of the photopolymerization oxygen-inhibition layer is typically around a hundred microns.[42] Such a narrow gap limits the refill speed of the prepolymer, thus limits the fabrication speed. Recent research has introduced optical inhibition using a second wavelength of light, creating an inhibition layer of several hundreds of microns thick, hence greatly improving the fabrication speed.[48]

1.3.3 Volumetric Photopolymerization Methods

Both point-scanning methods and plane-projection methods polymerize material sequentially, therefore, the latterly solidified parts need structural support from the formerly solidified parts. Because of gravity and fluid dynamics, insufficient support can cause deformation of the 3D printed construct, especially in soft materials such as hydrogels. However, these structural supports are often undesired to the 3D printed functional devices.

Volumetric photopolymerization-based 3D printing methods have been developed recently. Instead of sequential polymerization, these methods can polymerize the whole volume simultaneously, thus structural supports are not required. Also, solid state prepolymer can be used, because there is no invasive part dipping into the prepolymer. Typical volumetric methods include holographic method and tomographic method.

Holographic volumetric photopolymerization method

Holographic method uses a phase-only spatial light modulator (SLM) to modulate the laser and generates a 3D holographic image inside the prepolymer materials.[49] A computer generated hologram (CGH) is calculated by iterative algorithm and loaded on the SLM. In a low-numerical-aperture imaging system, the axial (along the light's propagation direction) resolution can be far worse than the lateral (perpendicular to the light's propagation direction) resolution. To overcome this problem, in holographic volumetric 3D printing method, the laser beam is split into three beams that propagate along x, y, and z directions, and then superpose at the resin container, as shown in Figure 1.1(e). Therefore, isotropic resolution can be achieved. During the entire fabrication process, the CGH is unchanged, and there is no motion involved. The whole 3D construct is solidified synchronously by one shot.

The CGH is calculated by iterative algorithm, which is very calculation-intensive and time-consuming. What's more, a common problem associated with CGH is that it has poor intensity uniformity. Visually, there are "speckles" in the image which is supposed to have a uniform light intensity distribution. This results in a coarse surface of the printed structure.

Tomographic volumetric photopolymerization method

Tomographic 3D printing method is the inverse process of computed tomography (CT) imaging. As shown in Figure 1.1(f), tomographic method uses a DMD to project a series of sinograms through the whole prepolymer container, while a rotary stage rotate the container in coordinate with the change of the sinograms. A cuboid secondary container with refractive-index-matched medium (which has the same refractive index as the prepolymer) is used to avoid the cylindrical prepolymer container deflecting light like a lens. The accumulated effect of photopolymerization reconstructs the desired 3D structure. [50,51]

The main problem associate with this method is its poor fabrication fidelity. Unlike all the other photopolymerization-based 3D printing methods mentioned in Section 1.3, which can deliver light energy to the prepolymer and yield a clear and hard-edged 3D energy distribution map either by sequentially scanning or by volumetric exposure; tomographic method yields a blurry and soft-edged 3D energy distribution map in the prepolymer. This is due to the fact that to reconstruct a hard-edged 3D image, the sinograms, which are calculated by Radon transform, contain negative values, which are physically invalid because light energy is always non-negative. As a result, the 3D image reconstructed by the sinograms without negative values become blurry and soft-edged. By carefully tuning the exposure dose to match the photopolymerization threshold, the desired targeted structure can be fabricated. However, compared to those methods with hard-edged energy distribution map, this method is far more sensitive to the fluctuation of exposure dose, thus fabrication fidelity compromises.

1.3.4 Summary

As an actively developing technology, various photopolymerization-based 3D printing methods have been invented. Each method has its own pros, cons, and unique features.

Fabrication resolution

Two-photon point-scanning method and super-resolution point-scanning method have the best performance in resolution, which typically can be as fine as 100 nm or even a few tens of nanometers. Single-photon point-scanning method, layer-by-layer plane-projection method, and continuous plane-projection method can achieve resolution of a few microns. The typical resolution reported for holographic volumetric photopolymerization method and tomographic volumetric photopolymerization method is a few tens of microns.

Fabrication speed

Here we use “typical time to fabricate a sample of 1 cm^3 volume” to compare the fabrication speed of different methods. Both holographic volumetric photopolymerization method and tomographic volumetric photopolymerization method take a few tens of seconds to complete. Continuous plane-projection method typically takes around 2 minutes, and layer-by-layer plane-projection method takes around 10 minutes. Single-photon point-scanning method takes a few hours. Two-photon and super-resolution point-scanning methods will take a few weeks to finish this same task.

Structural quality

Structural quality is important to the sample's mechanical properties. Samples of poor structural quality are more likely to break, and will last a shorter time. Tomographic volumetric photopolymerization method and continuous plane-projection method have the best structural quality performance, and holographic volumetric photopolymerization method is slightly worse due to the holographic speckles. Layer-by-layer plane-projection method create interfaces between layers, thus the structural quality is worse than continuous plane-projection method. All point-scanning methods create interfaces between lines, and have poor structural quality.

Overall, plane-projection 3D printing methods have a good balance among resolution, speed, and structural quality, hence it is the most promising tool for 3D printing functional microdevices.

1.4 Fabrication Resolution of Plane-projecting Methods

The fabrication resolution is a critical index to evaluate a 3D printing method. Because of the propagating nature of light, in a wide-field optical microscope, it is easier to achieve fine resolution in lateral direction (perpendicular to the propagation direction of light) than in axial direction (along the propagation direction of light). Similarly, plane-projecting methods also feature anisotropic fabrication resolution. We can use the *lateral resolution* and the *axial resolution* to characterize the fabrication resolution of plane-projecting 3D printing methods.

Lateral resolution determines the finest feature size on the X-Y plane, whereas axial resolution determines the finest overhanging layer thickness in the Z direction. Ideally, the lateral resolution should be determined by the size of micromirror on the DMD and the magnification of the projecting optics, while the axial resolution should be determined by the vertical stage's positioning resolution. However, there are a few factors that can also affect the lateral resolution and the axial resolution, including the Abbe diffraction limit, aberration, material absorption, light scattering, molecular diffusion, and so on. The influence of these factors can be negligible in macro-scale 3D printing, yet they have substantial influence on the resolution for micro-scale 3D printing.

1.4.1 Diffraction Limit

Though an optical projection system with greater de-magnification results in finer lateral resolution, infinitely fine resolution is not achievable. Abbe diffraction limit is a resolution limit applies to optical system due to the wave nature of light. A light beam cannot be focused into an infinitely small point by optical systems. Instead, an Airy disk will be formed. The diameter of the Airy spot can be estimated by Equation (1.1), where λ is the wavelength of light, and NA is the numerical aperture of the lens. According to Rayleigh's criteria, the resolution limit of the optical system is half of the diameter of the Airy disk, as given in Equation (1.2).

$$D_{Airy} = \frac{1.22\lambda}{NA} \tag{1.1}$$

$$d_{xy} = \frac{0.61\lambda}{NA} \tag{1.2}$$

A common plane-projection type 3D printer uses near UV light. A small numerical aperture lens is used in order to have enough field-of-view. Assume that $\lambda = 405$ nm, $NA = 0.05$, then the resolution limit is calculated as $d_{xy} = 4.05$ µm.

A finer diffraction resolution limit can be achieved by using a lens of higher numerical aperture or using a light source of shorter wavelength. Besides, super-resolution methods can bypass the diffraction limit. [36,37]

1.4.2 Optical Aberrations

Optical aberration is an important factor that can affect the resolution. There are two classes of aberrations, including monochromatic aberrations and chromatic aberrations. Both aberrations result in imperfect imaging, thus the resolution is deteriorated.

A well-designed objective lens, which contains multiple lens elements, can reduce the influence of aberrations, but also greatly increase the cost. Applying a smaller aperture to the imaging lenses can also reduce the aberrations, however the Abbe diffraction limit worsens. Using a narrow-spectrum light source such as single-color LED or laser is another way to avoid chromatic aberrations.

1.4.3 Material Absorption

Material's light absorption plays an important role in affecting the axial resolution. Light decays exponentially along the propagation direction due to absorption, as shown in Equation (1.3), where I_0 is the initial light intensity, I is the light intensity at the calculating position, α is the absorption coefficient, and z is the travel length of light. The light penetration depth is defined as the inverse of the absorption coefficient as Equation (1.4).

$$I = I_0 e^{-\alpha z} \tag{1.3}$$

$$d_z = \frac{1}{\alpha} \tag{1.4}$$

Prepolymer material subjected to exposure above the photopolymerization threshold will polymerize. As the light intensity decays along the propagation direction, photopolymerization only happens in the surface layer. Here we define the curing depth as the same as the light penetration depth d_z, which is also the axial resolution of the 3D printer.

Material absorption can also affect the lateral resolution. Upon light exposure, a layer of a certain thickness is polymerized. If the curing depth is greater than the optical depth of focus, then the out-of-focus plane will also polymerize, resulting in a deteriorated lateral resolution.

Equation (1.4) indicates that, in order to improve the axial resolution (i.e., to decrease d_z), the absorption coefficient of the prepolymer material α should be increased. This can be achieved by using high-absorption photoinitiators, increasing the photoinitiator concentration, or doping light-absorbing additives. [52] Common prepolymer materials have a curing depth of around 100 μm ~ 1 mm. By doping the material with absorptive additives, the curing depth can be reduced to tens of microns.

In order to prevent lateral resolution deterioration caused by out-of-focus plane polymerization, the curing depth should be smaller than the depth of focus. The depth of focus can be calculated by Equation (1.5), where δ is the required resolution, and NA is the numerical aperture.

$$d_{DoF} = \frac{\delta}{NA} \tag{1.5}$$

If the projection optics has a numerical aperture of 0.05, and 5 μm lateral resolution is required, then the depth of focus d_{DoF} is 100 μm. Hence, the material absorption should be strong enough to ensure the curing depth $d_z < d_{DoF} = 100$ μm.

1.4.4 Light Scattering

Light scattering can significantly deteriorate the fabrication resolution and fidelity. An optically clear media allows projecting a sharp pattern, however, an opaque media can scatter light and blur the projected pattern.

Although optically clear materials are desirable for photopolymerization-based 3D printing, some optically scattering materials are widely used in making functional devices. For example, micro/nano particles are added into the polymer to achieve specific physical properties; cells can also been incorporated to achieve biological activity. These particles can strongly scatter light. Besides, the polymers such as some hydrogels themselves can be intrinsically scattering.

The effect of light scattering is difficult to eliminate if an opaque material is used. A common practice to mitigate is to increase the material absorption by doping light absorptive additives.

1.4.5 Molecular diffusion

Although free radicals are only generated within the light illuminated region, the free radicals and propagating chains can diffuse out of the illuminated region and cause unwanted polymerization. According to Fick's laws of diffusion, the diffusion length can be estimated as Equation (1.6), where D is the diffusivity and t is the free-radical lifetime.

$$L = 2\sqrt{Dt} \tag{1.6}$$

In order to reduce the diffusion length, we can either use high viscosity materials which feature lower diffusivity, or dope free radical quencher such as 2,2,6,6-Tetramethylpiperidine 1-oxyl (TEMPO) to reduce the free radical lifetime. [53]

Besides the diffusion of free radical and propagating chain, the diffusion of oxygen also plays an important role.[46] As a photopolymerization inhibitor, oxygen is consumed by combining with free radicals or propagating chains, and is supplied from the ambient atmosphere. Those oxygen molecules diffused into the prepolymer solution from surrounding atmosphere create an uneven distribution of oxygen concentration, hence spatially uneven inhibition occurs. As a result, the fabrication fidelity is worsen.

1.5 Research Objectives

Although plane-projection photopolymerization-based 3D printing technique can reach micron scale resolution in the lateral direction under optimal condition, there are still some challenges with this technique.

One major challenge is the resolution deterioration caused by light scattering. The best fabrication resolution can only be reached when using a resin optimized for fabrication, however this is usually not the case when using functional materials. Functional materials can be light-scattering, either due to the polymer's properties, or due to the functional impurity such as micro/nano particles, biological cells, and so on. Light scattering can deteriorate the fabrication fidelity and resolution.

Another challenge is the poor axial resolution. Light projection method naturally comes with poor axial resolution. Though the lateral resolution is at micron scale, the axial resolution is at hundred-micron scale. Such anisotropic resolution make it difficult to make fine structures along the axial direction.

The following chapters are dedicated to address the light scattering issue and axial resolution issue in plane-projection photopolymerization-based 3D printing by manipulating light-matter interaction.

In Chapter 2, a flashing photopolymerization method is developed to improve the fabrication fidelity and resolution, where the prepolymer material is clear liquid before polymerization and become opaque solid after polymerization.

In Chapter 3, an artificial intelligence assisted approach is developed to improve the fabrication fidelity and resolution, where the prepolymer material is light scattering before polymerization.

In Chapter 4, a projection printing technique using patterned evanescent field is developed. By making use of the sub-micron scale penetration depth of evanescent field, this technique can be a good solution to improve the axial resolution of plane-projection 3D printing.

Acknowledgements

Chapter 1, in part, is adapted from the published book chapter, "Microstereolithography", S. You, K. Miller, S. Chen. *Biofabrication and 3D Tissue Modeling*, 2019. The dissertation author was the primary investigator and author of this book chapter.

Reference

[1] H. Zeng, P. Wasylczyk, D.S. Wiersma, A. Priimagi, Light Robots: Bridging the Gap between Microrobotics and Photomechanics in Soft Materials, Adv. Mater. 30 (2018) 1703554.

[2] W. Zhu, J. Li, Y.J. Leong, I. Rozen, X. Qu, R. Dong, Z. Wu, W. Gao, P.H. Chung, J. Wang, S. Chen, 3D-Printed Artificial Microfish, Adv. Mater. 27 (2015) 4411–4417.

[3] A. Servant, F. Qiu, M. Mazza, K. Kostarelos, B.J. Nelson, Controlled In Vivo Swimming of a Swarm of Bacteria-Like Microrobotic Flagella, Adv. Mater. 27 (2015) 2981–2988.

[4] J. Liu, H.H. Hwang, P. Wang, G. Whang, S. Chen, Direct 3D-printing of cell-laden constructs in microfluidic architectures, Lab Chip. 16 (2016) 1430–1438.

[5] A.K. Au, W. Huynh, L.F. Horowitz, A. Folch, 3D-Printed Microfluidics, Angew. Chemie Int. Ed. 55 (2016) 3862–3881.

[6] T.A. Duncombe, A.M. Tentori, A.E. Herr, Microfluidics: reframing biological enquiry, Nat. Rev. Mol. Cell Biol. 16 (2015) 554–567.

[7] J. Tavakoli, Y. Tang, Hydrogel Based Sensors for Biomedical Applications: An Updated Review, Polymers (Basel). 9 (2017) 364.

[8] L. Li, Y. Shi, L. Pan, Y. Shi, G. Yu, Rational design and applications of conducting polymer hydrogels as electrochemical biosensors, J. Mater. Chem. B. 3 (2015) 2920–2930.

[9] Q. Huang, J. Lee, F.T. Arce, I. Yoon, P. Angsantikul, J. Liu, Y. Shi, J. Villanueva, S.

Thamphiwatana, X. Ma, L. Zhang, S. Chen, R. Lal, D.J. Sirbuly, Nanofibre optic force transducers with sub-piconewton resolution via near-field plasmon–dielectric interactions, Nat. Photonics. 11 (2017) 352–355.

[10] S. Bianchi, G. Vizsnyiczai, S. Ferretti, C. Maggi, R. Di Leonardo, An optical reaction micro-turbine, Nat. Commun. 9 (2018) 4476.

[11] Z. Xie, Y. Lefier, M.A. Suarez, M. Mivelle, R. Salut, J.-M. Merolla, T. Grosjean, Doubly Resonant Photonic Antenna for Single Infrared Quantum Dot Imaging at Telecommunication Wavelengths, Nano Lett. 17 (2017) 2152–2158.

[12] I. Liberal, N. Engheta, Near-zero refractive index photonics, Nat. Photonics. 11 (2017) 149–158.

[13] A. Memic, A. Navaei, B. Mirani, J.A.V. Cordova, M. Aldhahri, A. Dolatshahi-Pirouz, M. Akbari, M. Nikkhah, Bioprinting technologies for disease modeling, Biotechnol. Lett. 39 (2017) 1279–1290.

[14] W. Zhu, K.R. Tringale, S.A. Woller, S. You, S. Johnson, H. Shen, J. Schimelman, M. Whitney, J. Steinauer, W. Xu, T.L. Yaksh, Q.T. Nguyen, S. Chen, Rapid continuous 3D printing of customizable peripheral nerve guidance conduits, Mater. Today. 21 (2018) 951–959.

[15] J. Koffler, W. Zhu, X. Qu, O. Platoshyn, J.N. Dulin, J. Brock, L. Graham, P. Lu, J. Sakamoto, M. Marsala, S. Chen, M.H. Tuszynski, Biomimetic 3D-printed scaffolds for spinal cord injury repair, Nat. Med. 25 (2019) 263–269.

[16] J.H. Wen, L.G. Vincent, A. Fuhrmann, Y.S. Choi, K.C. Hribar, H. Taylor-Weiner, S. Chen, A.J. Engler, Interplay of matrix stiffness and protein tethering in stem cell differentiation, Nat. Mater. 13 (2014) 979–987.

[17] J. Vanderburgh, J.A. Sterling, S.A. Guelcher, 3D Printing of Tissue Engineered Constructs for In Vitro Modeling of Disease Progression and Drug Screening, Ann. Biomed. Eng. 45 (2017) 164–179.

[18] A. Vashist, A. Vashist, Y.K. Gupta, S. Ahmad, Recent advances in hydrogel based drug delivery systems for the human body, J. Mater. Chem. B. 2 (2014) 147–166.

[19] C.B. Fox, Y. Cao, C.L. Nemeth, H.D. Chirra, R.W. Chevalier, A.M. Xu, N.A. Melosh, T.A. Desai, Fabrication of Sealed Nanostraw Microdevices for Oral Drug Delivery, ACS Nano. 10 (2016) 5873–5881.

[20] I. Zein, D.W. Hutmacher, K.C. Tan, S.H. Teoh, Fused deposition modeling of novel scaffold architectures for tissue engineering applications, Biomaterials. 23 (2002) 1169–1185.

[21] P.K. Gokuldoss, S. Kolla, J. Eckert, Additive Manufacturing Processes: Selective Laser Melting, Electron Beam Melting and Binder Jetting—Selection Guidelines, Materials (Basel). 10 (2017) 672.

[22] D.L. Cohen, E. Malone, H. Lipson, L.J. Bonassar, Direct Freeform Fabrication of Seeded Hydrogels in Arbitrary Geometries, Tissue Eng. 12 (2006) 1325–1335.

[23] M. Vaezi, H. Seitz, S. Yang, A review on 3D micro-additive manufacturing technologies, Int. J. Adv. Manuf. Technol. 67 (2013) 1721–1754.

[24] W. Zhu, X. Ma, M. Gou, D. Mei, K. Zhang, S. Chen, 3D printing of functional biomaterials for tissue engineering, Curr. Opin. Biotechnol. 40 (2016) 103–112.

[25] S. Kumar, Selective laser sintering: A qualitative and objective approach, JOM. 55 (2003) 43–47.

[26] S. Maruo, T. Saeki, Femtosecond laser direct writing of metallic microstructures by photoreduction of silver nitrate in a polymer matrix, Opt. Express. 16 (2008) 1174.

[27] J.M.G. Cowie, Valeria Arrighi, Polymers: Chemistry and Physics of Modern Materials, 3rd ed., CRC Press, 2007.

[28] Y. Lu, S.C. Chen, Micro and nano-fabrication of biodegradable polymers for drug delivery, Adv. Drug Deliv. Rev. 56 (2004) 1621–1633.

[29] S. Maruo, O. Nakamura, S. Kawata, Three-dimensional microfabrication with two-photon-absorbed photopolymerization, Opt. Lett. 22 (1997) 132.

[30] W. Zhang, S. Chen, Femtosecond laser nanofabrication of hydrogel biomaterial, MRS Bull. 36 (2011) 1028–1033.

[31] S.W. Hell, J. Wichmann, Breaking the diffraction resolution limit by stimulated emission: stimulated-emission-depletion fluorescence microscopy, Opt. Lett. 19 (1994) 780.

[32] E. Betzig, G.H. Patterson, R. Sougrat, O.W. Lindwasser, S. Olenych, J.S. Bonifacino, M.W. Davidson, J. Lippincott-Schwartz, H.F. Hess, Imaging Intracellular Fluorescent Proteins at Nanometer Resolution, Science (80-.). 313 (2006) 1642–1645.

[33] M.G.L. Gustafsson, Surpassing the lateral resolution limit by a factor of two using structured illumination microscopy, J. Microsc. 198 (2000) 82–87.

[34] R. Wollhofen, J. Katzmann, C. Hrelescu, J. Jacak, T.A. Klar, 120 nm resolution and 55 nm structure size in STED-lithography, Opt. Express. 21 (2013) 10831.

[35] T.L. Andrew, H.-Y. Tsai, R. Menon, Confining Light to Deep Subwavelength Dimensions to Enable Optical Nanopatterning, Science (80-.). 324 (2009).

[36] L. Li, R.R. Gattass, E. Gershgoren, H. Hwang, J.T. Fourkas, Achieving λ/20 Resolution by One-Color Initiation and Deactivation of Polymerization, Science (80-.). 324 (2009).

[37] T.F. Scott, B.A. Kowalski, A.C. Sullivan, C.N. Bowman, R.R. McLeod, Two-Color Single-Photon Photoinitiation and Photoinhibition for Subdiffraction Photolithography, Science

(80-.). 324 (2009) 913–917.

[38] Z. Gan, Y. Cao, R. a Evans, M. Gu, Three-dimensional deep sub-diffraction optical beam lithography with 9 nm feature size., Nat. Commun. 4 (2013) 2061.

[39] A. Bertsch, S. Zissi, J.Y. Jézéquel, S. Corbel, J.C. André, Microstereophotolithography using a liquid crystal display as dynamic mask-generator, Microsyst. Technol. 3 (1997) 42–47.

[40] C. Sun, N. Fang, D.M. Wu, X. Zhang, Projection micro-stereolithography using digital micro-mirror dynamic mask, Sensors Actuators A Phys. 121 (2005) 113–120.

[41] J.-W. Choi, R. Wicker, S.-H. Lee, K.-H. Choi, C.-S. Ha, I. Chung, Fabrication of 3D biocompatible/biodegradable micro-scaffolds using dynamic mask projection microstereolithography, J. Mater. Process. Technol. 209 (2009) 5494–5503.

[42] J.R. Tumbleston, D. Shirvanyants, N. Ermoshkin, R. Janusziewicz, A.R. Johnson, D. Kelly, K. Chen, R. Pinschmidt, J.P. Rolland, A. Ermoshkin, E.T. Samulski, J.M. Desimone, Continuous liquid interface production of 3D objects, Science (80-.). 347 (2015) 1349–1352.

[43] R. Liska, M. Schuster, R. Inführ, C. Turecek, C. Fritscher, B. Seidl, V. Schmidt, L. Kuna, A. Haase, F. Varga, H. Lichtenegger, J. Stampfl, Photopolymers for rapid prototyping, J. Coatings Technol. Res. 4 (2007) 505–510.

[44] A. Chiappone, E. Fantino, I. Roppolo, M. Lorusso, D. Manfredi, P. Fino, C.F. Pirri, F. Calignano, 3D printed PEG-based hybrid nanocomposites obtained by sol-gel technique, ACS Appl. Mater. Interfaces. 6 (2016) 5627–5633.

[45] D.A. Walker, J.L. Hedrick, C.A. Mirkin, Rapid, large-volume, thermally controlled 3D printing using a mobile liquid interface, Science (80-.). 366 (2019) 360–364.

[46] T.Y. Lee, C.A. Guymon, E.S. Jönsson, C.E. Hoyle, The effect of monomer structure on oxygen inhibition of (meth)acrylates photopolymerization, Polymer (Guildf). 45 (2004) 6155–6162.

[47] W. Zhu, K.R. Tringale, S.A. Woller, S. You, S. Johnson, H. Shen, J. Schimelman, M. Whitney, J. Steinauer, W. Xu, T.L. Yaksh, Q.T. Nguyen, S. Chen, Rapid continuous 3D printing of customizable peripheral nerve guidance conduits, Mater. Today. (2018).

[48] M.P. de Beer, H.L. van der Laan, M.A. Cole, R.J. Whelan, M.A. Burns, T.F. Scott, Rapid, continuous additive manufacturing by volumetric polymerization inhibition patterning, Sci. Adv. 5 (2019) eaau8723.

[49] M. Shusteff, A.E.M. Browar, B.E. Kelly, J. Henriksson, T.H. Weisgraber, R.M. Panas, N.X. Fang, C.M. Spadaccini, One-step volumetric additive manufacturing of complex polymer structures, Sci. Adv. 3 (2017) eaao5496.

[50] B.E. Kelly, I. Bhattacharya, H. Heidari, M. Shusteff, C.M. Spadaccini, H.K. Taylor, Volumetric additive manufacturing via tomographic reconstruction, Science (80-.). 363 (2019) 1075–1079.

[51] P.N. Bernal, P. Delrot, D. Loterie, Y. Li, J. Malda, C. Moser, R. Levato, Volumetric Bioprinting of Complex Living-Tissue Constructs within Seconds, Adv. Mater. 31 (2019) 1904209.

[52] B. Grigoryan, S.J. Paulsen, D.C. Corbett, D.W. Sazer, C.L. Fortin, A.J. Zaita, P.T. Greenfield, N.J. Calafat, J.P. Gounley, A.H. Ta, F. Johansson, A. Randles, J.E. Rosenkrantz, J.D. Louis-Rosenberg, P.A. Galie, K.R. Stevens, J.S. Miller, Multivascular networks and functional intravascular topologies within biocompatible hydrogels, Science (80-.). 364 (2019) 458–464.

[53] A.P. Zhang, X. Qu, P. Soman, K.C. Hribar, J.W. Lee, S. Chen, S. He, Rapid Fabrication of Complex 3D Extracellular Microenvironments by Dynamic Optical Projection Stereolithography, Adv. Mater. 24 (2012) 4266–4270.

Chapter 2 High-fidelity 3D Printing using Flashing Photopolymerization

Abstract

Photopolymerization-based 3D printing has emerged as a promising technique to fabricate 3D structures. However, during the printing process, polymerized materials such as hydrogels often become highly light-scattering, thus perturbing incident light distribution and thereby deteriorating the final print resolution. To overcome this scattering-induced resolution deterioration, we developed a novel method termed flashing photopolymerization (FPP). Our FPP approach is informed by the fundamental kinetics of photopolymerization reactions, where light exposure is delivered in millisecond-scale flashes, as opposed to continuous light exposure. During the period of flash exposure, the prepolymer material negligibly scatters light. The material then polymerizes and opacifies in absence of light, therefore the exposure pattern is not perturbed by scattering. Compared to the conventional use of a continuous wave (CW) light source, the FPP fabrication resolution is improved. FPP also shows little dependency on the exposure, thus minimizing trial-and-error type optimization. Using FPP, we demonstrate its use in generating high-fidelity 3D printed constructs.

2.1 Introduction

Photopolymerization-based 3D printing techniques [1–5] are powerful tools in 3D freeform structure fabrication–they are able to fabricate micro- and nano- scale complex geometries that would otherwise be challenging to achieve with traditional fabrication methods, such as machining or molding. Among the various types of photopolymerization-based 3D printing techniques, light-projection-based 3D printing methods, such as continuous liquid interface production (CLIP),[1] projection micro-stereolithography (PμSL),[2] and dynamic optical projection stereolithography (DOPsL) [6] employ a digital light processing (DLP) technique to project arbitrary patterns onto a prepolymer solution, achieving both a fine resolution and fast fabrication speed.[7] Photopolymerization-based 3D printing has found numerous promising applications in consumer products as well as biomedical engineering such as implantation,[8] imaging,[9] tissue culture,[10,11] drug delivery,[12] and so on.[13–16] However, despite these successful demonstrations of 3D polymeric structure fabrication, this technique faces significant challenges to fabricate functional devices with micron-sized features when using materials that are not optimized for fabrication. For example, water-containing hydrogel scaffolds for biomedical applications often demand a complex 3D architecture with micron-scale features in order to capture the dynamic interactions between the cells and microenvironment, yet most hydrogel materials can hardly be fabricated at a very fine resolution.

To achieve a high resolution in photopolymerization-based 3D printing, the proper light exposure dose must be determined. Insufficient exposure doses cannot photopolymerize the material, while excessive exposure doses can lead to polymerization beyond the desired regions. Generally, the proper exposure dose window is very narrow and needs to be identified for each desired structure and prepolymer material; usually done through manual trial-and-error. This optimization process is time-consuming and costly, and often the resultant fabrication resolution achieved is suboptimal compared to both the desired designed dimensions and the printer's optical resolution.

This resolution deterioration is mainly caused by three factors, the first of which is light scattering. Optically-clear media allow for sharp patterns of high-fidelity, but the same patterns would be inevitably blurred or have suboptimal features in an optically-scattering media. The second factor is optical depth of focus—depending on the printing media, light can penetrate and polymerize up to a certain depth from the initial plane of incidence. If this cure depth is greater than the optical depth of field, then the out-of-focus plane may experience unwanted polymerization. According to ray optics theory, an imaging system with a lens of numerical aperture of 0.05 and a resolution requirement of 5 μm will have a depth of focus of 100 μm. The cure depth is determined by the absorption of the material, typically ranging from 100 μm to a few millimeters. [17,18] By doping the media with light absorbers, the cure depth can be significantly reduced, minimizing resolution deterioration. The third is molecular diffusion, related to free-radical generation and propagation. Although free radicals are only generated within the light-illuminated region, free radicals and propagating chains can diffuse out of the light-illuminated areas and thus cause unwanted polymerization. According to Fick's laws of diffusion, the diffusion length can be estimated as $L = 2\sqrt{Dt}$, where D is the diffusivity and t is the free-radical lifetime,[19] where the diffusion coefficient of common free radicals are reported to be around 1 x 10^{-5} cm^{-2}/s in both polar and nonpolar solvents, [20,21] and free radical lifetimes has been reported to be at the scale of 10 milliseconds. [22] Thus, the free radical diffusion length is at the scale of a few microns, but by doping free radical quenchers, the diffusion length can be reduced. [6] These three factors may all be negligible in fabricating a macro-scale device, yet they have substantial influence in microstructure fabrication or biological structure fabrication, where required feature sizes are on the order of microns as well. Among these three factors, light scattering represents a significant challenge, and can be difficult to mitigate since it is a material-dependent property.

Depending on the prepolymer's formulation and homogeneity, it may be optically clear prior to the start of fabrication, yet light scattering can increase as the material begins to polymerize.

Some polymers, such as poly(methyl methacrylate) (PMMA), are as transparent as glass, thus barely suffer from the light scattering problem. Some others, notably hydrogels such as poly(ethylene glycol) diacrylate (PEGDA) hydrogel and di(ethylene glycol) dimethacrylate (DEGDMA) hydrogel, are initially a transparent liquid before polymerization, but once polymerized, they become translucent like agarose, thus can be scattering.

Ideally, light exposure should be avoided as scattering increases, however current light-projection-based 3D printing techniques employ a continuous wave (CW) light source, such as a mercury lamp, laser, or light emitting diode (LED), to photopolymerize the prepolymer solution. With such CW sources, the light exposure, polymerization propagation, and increased scattering (opacification) all begin to overlap during the printing process, compounding the inevitability of scattering-induced photopolymerization of undesired regions, thus resulting in low print fidelity.

To address these challenges, we take advantage of how free-radical photopolymerization is a multi-step process, where light exposure conditions only affect free radical generation, [23,24] while the propagation of polymerizing chains can continue to take place even in dark conditions (i.e. after light illumination). Scherzer et. al. used real-time Fourier-transform infrared (FTIR) spectroscopy to investigate the photopolymerization process of tripropylene glycol diacrylate (TPGDA) and found that chain propagation continues to proceed a few seconds after a short (~ 100 ms) and intense light exposure dose, eventually reaching a conversion rate similar to that when using a CW exposure.[25] Only a small fraction of the monomers in solution was consumed during the exposure period, while the majority was consumed during the dark period thereafter.

Here, we report a light-projection-based 3D printing system that uses flashing exposures for photopolymerization, henceforth referred to as flashing photopolymerization (FPP). With FPP, we chronologically separate three key events: light exposure, polymerization, and opacification.

First, we apply a flashing exposure to generate a large amount of free radicals in the desired pattern; this is the light exposure step. Second, after light exposure has ceased, the prepolymer solution undergoes polymerization and opacification in the dark. In this way, the prepolymer is only exposed to light while it is negligibly scattering, thus minimizing scattering-induced resolution deterioration.

In this report, we first present the setup of the FPP 3D printer as well as examples of FPP-printed constructs. Next, we conducted resolution comparisons between CW and FPP and show how polymerization can increase scattering. Lastly, we model and simulate the photopolymerization process to explain the mechanism of FPP.

2.2 High Fidelity 3D Printing

The schematic of the FPP 3D printer is shown in Figure 2.1(a). The system uses a xenon flash tube as the light source, which is connected to an electronically-triggered controller unit. Using an optical lens setup, a digital micro-mirror device (DMD) projects the photomask image onto and through a transparent anti-adhesion substrate made of polydimethylsiloxane (PDMS, Sylgard 184, Dow Corning) coated on a glass vat containing the prepolymer solution. A motorized stage is used to control the motion of the sample-supporting platform. Finally, a computer with custom software controls and synchronizes these mechanisms.

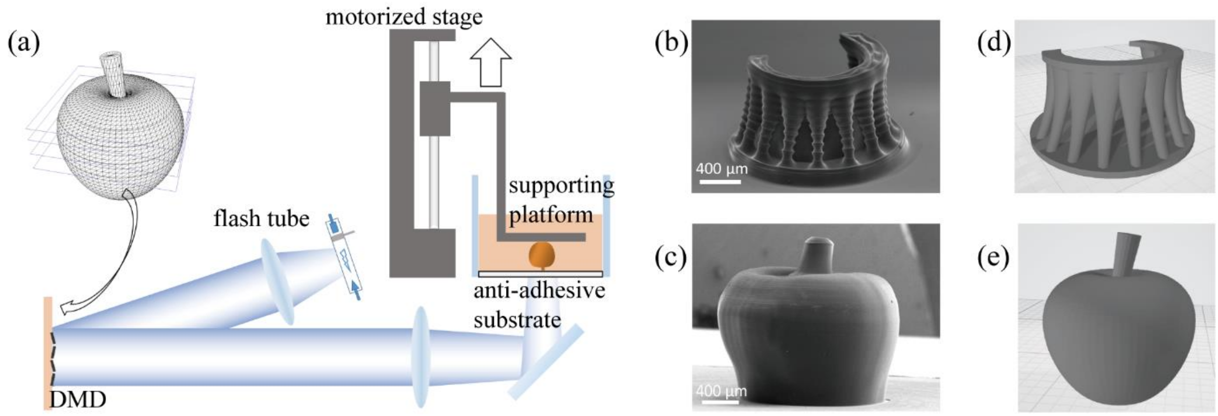

Figure 2.1| Flashing photopolymerization 3D printing. (a) Schematic of the FPP 3D printing system. (b) SEM image of a micro "altar" printed by FPP with 100 µm layer thickness. Scale bar = 400 µm. (c) SEM image of a micro "apple" printed by FPP with 20 µm layer thickness. Scale bar = 400 µm. (d) and (e) are the original 3D models of (b) and (c), respectively.

The 3D printing process is as follows: a digitally-designed 3D model is sliced into 2D cross-sectional images. The supporting platform is lowered to maintain a very narrow spacing (typically between 10 to 100 microns) between the supporting platform and the anti-adhesion substrate before printing. During printing, the xenon flash tube is triggered to flash at a specified energy; the resulting first layer photopolymerizes and attaches to the supporting platform. The motorized stage then raises the supporting platform by one-layer thickness of typically 10-100 microns so that unpolymerized material can refill the subsequent vacant space between the anti-adhesion substrate and the previously-polymerized layer(s). A new 2D image slice can be loaded onto the DMD, and the flash tube flashes to solidify this new layer. By repeating these steps, a 3D object can be printed in a layer-by-layer manner.

In general, there is a tradeoff between print speed and quality, usually mediated by layer thickness. Printing with larger layer thicknesses allows for faster print times, albeit at the expense of more inter-layer artifacts and a generally coarser quality, while printing with smaller layer thicknesses will produce better fabrication quality over a longer period of time. We demonstrate this with the 3D-printing of two representative structures using 100% PEGDA (Mn = 575 Da) and 4% (w/v) Irgacure 784, depicted in Figure 2.1. Figure 2.1(b) shows the scanning electron microscopy (SEM) image of an altar-like structure printed with a 100-µm-layer thickness, and Figure 2.1(c) shows the SEM image of an apple-like structure printed with 20-µm-layer thickness, which has a much smoother surface compared to the altar.

To compare the resolution differences between the FPP and CW printing modes, we designed a photomask with sharp, fine lines culminating in a spoke-like pattern. The photomask was printed on the same instrument using a UV-LED for CW and a xenon flash tube for FPP modes and with an aqueous hydrogel prepolymer solution containing 50% (v/v) PEGDA mixed with 4% (w/v) lithium phenyl-2,4,6-trimethylbenzoylphosphinate (LAP) as the photoinitiator. To simplify testing and analysis, we limited the printed structure to a single 250-µm thick layer, where different exposure doses were used to polymerize the structure. For the continuous UV-LED, we used a series of different energy outputs but kept the illumination time constant, whereas for the flash tube we used a series of different total energies but delivered in a single flash exposure for each. We evaluated resolution in this case by determining the unresolved fraction, that is, the ratio between the unresolved diameter and the outer diameter of the spoke-pattern. Here, a smaller unresolved fraction would mean a better resolution.

To calibrate the exposure dose, we used a series of different LED output powers and a series of different flash energies to polymerize a volume of prepolymer solution. At low exposure doses, the material is unable to polymerize, but as we increased the energy, at a certain value the spoke-pattern was able to polymerize – we defined this value as the minimum *unit exposure dose*. Note that the unit exposure dose represents different energies in the CW vs. FPP modes as they are significantly different in both duration time and electromagnetic spectrum. From this, we defined a *relative exposure dose* E_r the ratio between the actual exposure energy and the unit exposure dose. We used $E_r = \{1, 1.26, 1.59, 2, 2.52, 3.18, 4\}$ across both the CW and FPP modes to polymerize our spoke pattern structure and assess the unresolved fractions for each mode. Figures 2.2(a) and 2.2(b) show bright-field microscopy images of the resultant structures for the CW exposure and FPP exposure modes, respectively. We noted two trends: 1) that the peripheral parts of the spoke pattern are often well-resolved due to their large relative spacing, while the centers are difficult to resolve due to their small relative spacing; and 2) that a higher total exposure dose leads to a larger unresolved area. The outer diameter of the spoke is 1.9 mm, and the unresolved diameter is less than 0.4 mm for all samples. The relation between the exposure energy and unresolved fraction is plotted in Figure 2.2(c). As can be seen from the plot, the FPP exposure mode always has a better resolution than that of the continuous mode. For the CW mode, it is clear that the unresolved fraction is strongly-dependent on the exposure dose, while for the FPP exposure mode, the unresolved fraction is insensitive to the exposure energy. When $E_r = 1$, the unresolved region resulting from FPP is 82% as large as that of when using CW. When $E_r = 4$, the unresolved region resulting from FPP is 23% as large as that of when using CW. These results show that using FPP can achieve better capability in resolving fine structures than using CW, and by using a flashing light source, the tolerance window of exposure dose is significantly broadened while simultaneously increasing fabrication resolution, thus significantly simplifying the optimization process.

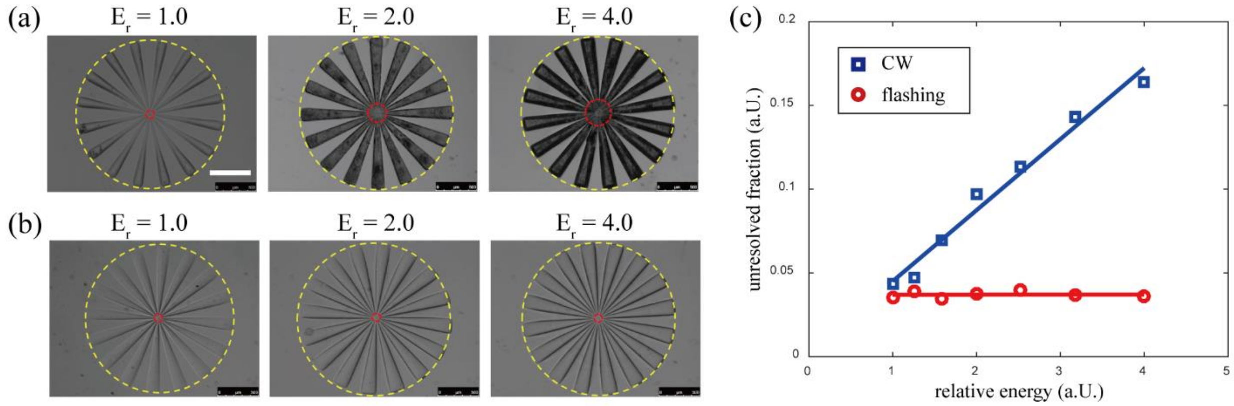

Figure 2.2| Resolution test for the CW exposure mode and FPP exposure mode. (a) Patterns printed with CW exposure at different relative energies. (b). Patterns printed with FPP exposure at different relative energies. (c) Relation between the relative energy and unresolved fraction. Yellow and red circles in (a) and (b) indicate the outer diameter and the unresolved diameter, respectively. Scale bar = 500 µm.

2.3 Theory and Mechanism

2.3.1 Material Scattering

Scattering is a significant factor in resolution deterioration, and there are three main factors that determine optical scattering in polymers. The first factor is the size of the molecules themselves – in a homogeneous polymer system, Rayleigh scattering dominates, where the intensity is proportional to the molecular weight of the polymer.[23] The second factor is the degree of crystallinity, where some polymers can form micron-size crystallites which induce strong Mie scattering.[26] The third factor is phase separation. Typically, a polymer has porous microstructures if it is polymerized from a monomer in solution because local solubility decreases as the polymer chain length increases. As polymerization continues, system homogeneity decreases as a result of phase separation, making it highly scattering.[27] In photopolymerization-based 3D printing, all three of these effects may occur and compound – light exposure induces molecular weight increase and thus Rayleigh scattering also increases. As the liquid-state prepolymer starts to solidify, crystallites also begin forming, thus causing further light scattering. In cases where the prepolymer contains solvents (e.g. hydrogels), the scattering phenomenon can be even stronger due to the resultant phase separation. Altogether, opacification of the material leads to nonspecific exposure and polymerization in undesired areas, resulting in deteriorated fabrication resolution.

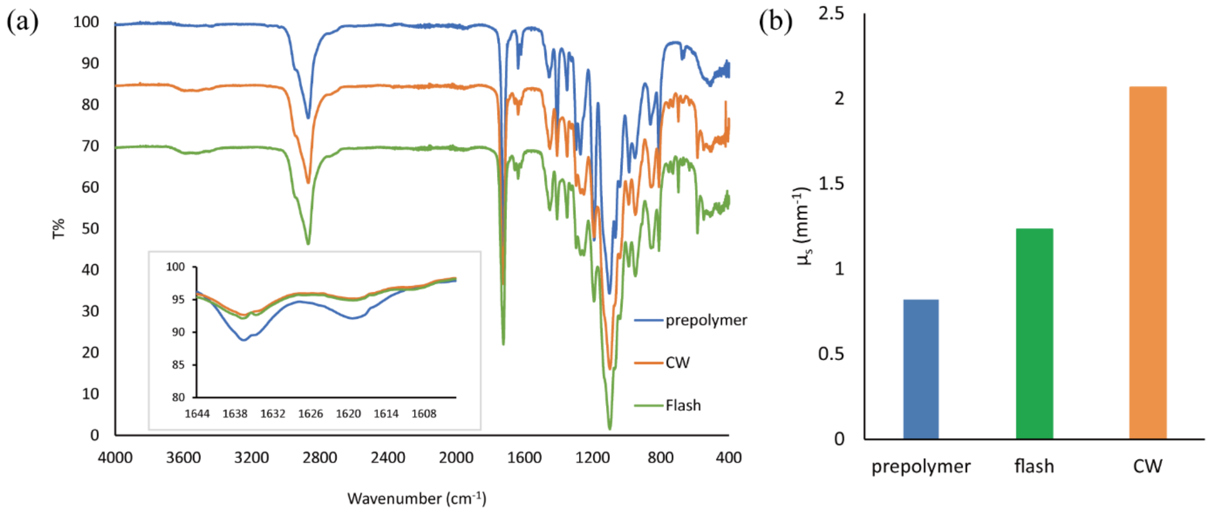

Figure 2.3| Scattering changes during polymerization. (a) FTIR spectrum of pure PEGDA (Mn = 575), dehydrated PEGDA slab polymerized with FPP exposure, and dehydrated PEGDA slab polymerized by CW exposure. Inset: zoom-in view at around 1630 cm^{-1}. (b) Scattering coefficient of PEGDA prepolymer solution, PEGDA slab polymerized with FPP exposure, and PEGDA slab polymerized by CW exposure at 365 nm.

In order to demonstrate that the material opacifies as it polymerizes, we fabricated slab samples with 50% PEGDA and 4% LAP via both CW and FPP methods and measured their monomer conversion rates and scattering coefficients at 365 nm. A FTIR spectroscope was used to measure the infrared (IR) transmittance of the unpolymerized PEGDA, the slabs polymerized via CW, and the slabs polymerized via FPP, the results of which are shown in Figure 2.3(a). As compared to unpolymerized PEGDA, the alkene groups were consumed after exposure as shown in the reduction of absorption peak of C=C bond around 1630 cm^{-1}.[28,29] The conversion rate of PEGDA polymer after CW and FPP exposure was calculated to be 27.5% and 22.2%, respectively.

Separately, a UV-Vis-NIR spectroscope with integrating sphere was used to measure the scattering property of the same three sample types. The scattering coefficients were calculated with the Inverse Adding-Doubling (IAD) algorithm, which is widely used in calculating the scattering coefficient and absorption coefficient of thick biological tissue. [30,31] The scattering coefficients at 365 nm were calculated to be 0.82 mm^{-1}, 1.23 mm^{-1}, and 2.07 mm^{-1} for the prepolymer sample, slab polymerized via FPP, and slab polymerized via CW exposure, respectively (Figure 2.3(b)). This shows that as the PEGDA prepolymer undergoes photopolymerization either by CW or FPP exposure, its scattering coefficient increases. A high-speed camera was used to record this opacification in real-time to further validate the opacification phenomenon, shown in Figure 2.S4.

2.3.2 Photopolymerization Kinetics

Using FPP we can chronologically separate the light exposure event from downstream polymerization and opacification effects, the mechanism of which can be explained by photopolymerization kinetics. The free-radical photopolymerization process can be divided into three stages: 1) photoinitiation, where upon exposure to light, a photoinitiator molecule is homolytically-cleaved into two free radicals. These react with monomers and then become active propagating chains. 2) The second stage is propagation, where the initial chains continue to react with monomers and grow longer. 3) The third is termination, where an active chain stops propagating after combining with a free radical or another propagating chain.[32]

The initiation rate is proportional to the photoinitiator quantum yield Φ and photon absorption quantity per unit volume per unit time N_{abs}. The reaction rate of chain propagation r_p is proportional to reactive functional group concentration $[M]$, propagating chain concentration $[P^*]$, and chain propagation rate coefficient k_p. The reaction rate of chain termination is proportional to the square of propagating chain concentration *[P*]* and chain termination rate coefficient k_t. The initiation rate, propagation rate and termination rate are given by Equations (2.1)-(2.3). [23]

$$r_i = 2\Phi N_{abs} \tag{2.1}$$

$$r_p = k_p[M][P*] \tag{2.2}$$

$$r_t = k_t[P*]^2 \tag{2.3}$$

The change of reactive functional group concentration and propagating chain concentration are given by Equations (2.4), (2.5).

$$\frac{\partial[M]}{\partial t} = -r_p \tag{2.4}$$

$$\frac{\partial[P*]}{\partial t} = r_i - r_t \tag{2.5}$$

As the prepolymer solution becomes more viscous, both the propagation kinetic constant and termination kinetic constant decrease during polymerization reaction. According to the well-established diffusion-controlled free-radical polymerization model,[28,33–37] the propagation rate coefficient k_p and the termination rate coefficient k_t can be determined by Equations (2.6) and (2.7), [28,37]

$$k_p = \frac{1}{\dfrac{1}{k_{p0}} + \dfrac{1}{k_{p,D}}} \tag{2.6}$$

$$k_t = \frac{1}{1/k_{t,SD} + 1/k_{t,TD}} + k_{t,RD} \tag{2.7}$$

where k_{p0} is the propagation rate coefficient without diffusion control; $k_{p,D}$ characterizes the diffusion-controlled part of the propagation reaction; $k_{t,SD}$ is the segmental-diffusion-controlled termination rate coefficient; $k_{t,TD}$ is the translational-diffusion-controlled termination rate coefficient; $k_{t,RD}$ is the reaction-diffusion-controlled termination rate coefficient. Additional equations and constants to model the photopolymerization process are available in the Experimental Section.

Here we use the model described above to numerically solve the photopolymerization kinetics problem in two scenarios. For both scenarios, the material system is 100% PEGDA with 4% (w/v) Irgacure 784 photoinitiator. Sample thickness is 100 microns. The photoinitiator has an absorbance A = 1.6 at 365 nm at 1 cm thickness at 0.1% concentration, thus A = 0.64 at 100 micron thickness at 4% concentration. We assume that the quantum efficiency of the photoinitiator is 1. In the first scenario, there is a low-intensity CW exposure lasting for 5 seconds. We simulated the photopolymerization kinetics under the light illumination intensity at 1.1 $\mathrm{mW\cdot cm^{-2}}$, 2.2 $\mathrm{mW\cdot cm^{-2}}$, or 4.3 $\mathrm{mW\cdot cm^{-2}}$. In the second scenario, there is a flashing exposure, which lasts for 10 milliseconds. We simulated the average flashing intensity at 106.5 $\mathrm{W\cdot cm^{-2}}$, 117.2 $\mathrm{W\cdot cm^{-2}}$, or 127.8 $\mathrm{W\cdot cm^{-2}}$. (See Table S1 for the relation between illumination intensity and free radical generation rate).

The simulation results are shown in Figure 2.4(a) and (b), respectively. The shaded area in Figure 2.4 indicates the light exposure period. The material properties and kinetic parameters of PEGDA have been studied previously [28] and are summarized in the Experimental Section.

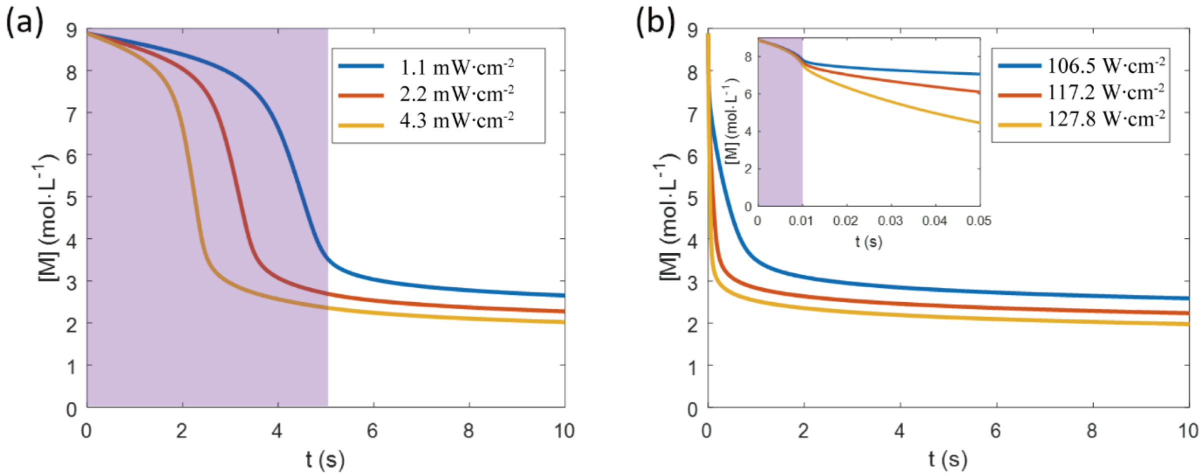

Figure 2.4| PEGDA photopolymerization simulation of the CW exposure mode and the FPP exposure mode. (a) Unconverted functional group concentration versus time. The system is subject to a 5-second light exposure under the light illumination intensity at 1.1 mW·cm^{-2}, 2.2 mW·cm^{-2}, or 4.3 mW·cm^{-2}. (b) Unconverted functional group concentration versus time. The system is subject to a 10-millisecond light exposure at 106.5 W·cm^{-2}, 117.2 W·cm^{-2}, or 127.8 W·cm^{-2}. The inset of (b) is a zoom-in view in time scale. The shaded area indicates the light exposure period.

From Figure 2.4, we can see that both scenarios reach a similar final conversion rate, showing that even a short exposure is sufficient to photopolymerize the monomer. The difference is that in the CW exposure scenario, polymerization and opacification begins and continues to occur while the light is still on, and the aforementioned scattering effects will deflect light outside of the desired areas. In the FPP scenario, the material can ‘safely’ polymerize and opacify in darkness, with no light to scatter into undesired areas.

2.4 Conclusions

We have successfully developed a flashing photopolymerization (FPP) method for photopolymerization-based 3D printing. By using a brief flash exposure instead of a continuous exposure, the material remains optically clear during the exposure period, thus minimizing light scattering and resulting in finer fabrication resolution. Both theoretical analysis and experimental demonstration have revealed the different scattering effects associated with CW vs. FPP exposure modes. By chronologically separating the light exposure event from the polymerization and opacification events, one can significantly improve the fidelity of 3D-printed structures. This is particularly significant for microscale 3D printing where scattering effects can have significant impacts on the feature sizes necessary for microstructure formation, such as hydrogel 3D printing for bioengineering.

2.5 Experimental Section

Materials

PEGDA (Mn = 575 Da) was purchased from Sigma-Aldrich. Irgacure 784 was purchased from Ciba Specialty Chemicals, now a subsidiary of BASF. LAP was synthesized in-house following previously-published methods.[38] The xenon flash tube was purchased from Xenon Flash Tubes.

Simulation of photopolymerization

The propagation and termination kinetic of the system is related to the degree of conversion, as shown in Equations (2.8)-(2.12), [28,37]

$$X = ([M]_0 - [M]) / [M]_0 \tag{2.8}$$

$$k_{\mathrm{p},D} = \frac{k_{\mathrm{p},D0}}{e^{cX}} \tag{2.9}$$

$$k_{t,TD} = \frac{k_{t,TD0}}{e^{cX}} \tag{2.10}$$

$$k_{t,SD} = k_{t,SD0} \tag{2.11}$$

$$k_{t,RD} = C_{RD} k_p (1 - X) \tag{2.12}$$

where X is the degree of conversion; $[M]$ is the unconverted functional group (C=C double bond) concentration, $[M]_0$ is the initial unconverted functional group concentration; c is the relative viscosity coefficient; $k_{p,D0}$ is the diffusion-controlled propagation rate coefficient at zero conversion; $k_{t,TD0}$ and $k_{t,SD0}$ are the translational-diffusion-controlled termination rate coefficient and the segmental-diffusion-controlled termination rate coefficient at zero conversion; C_{RD} is the reaction-diffusion proportion parameter.

The material properties and kinetic parameters of PEGDA (Mn = 250) determined by Wu, et. al, are listed in Table 2.1. [28] Matlab was used to perform the numerical simulation.

Table 2.1. Material properties and kinetic parameters of PEGDA

$[M_0]$	8.88 mol·L^{-1}	c	34.149
k_{p0}	1860 L·mol^{-1}·s^{-1}	$k_{p,D0}$	8.994 x 10^{11} L·mol^{-1}·s^{-1}
$k_{t,SD}$	4.39 x 10^{6} L·mol^{-1}·s^{-1}	$k_{t,TD0}$	1.002 x 10^{7} L·mol^{-1}·s^{-1}
C_{RD}	1.0146		

Infrared spectrum measurement

IR spectrum measurements were performed on a Perkin Elmer Spectrum Two FTIR spectroscope. Polymerized samples were dried to eliminate the influence of the spectrum of water; first by snap-freeze in liquid nitrogen, then dried by lyophilization (Labconco Freezone, lyophilize at -55 °C for 3 days).

Scattering coefficient measurement

Three samples were prepared for the measurement in a UV-Vis-NIR spectroscope (Perkin Elmer, Lambda 1050). The prepolymer solution (50% PEGDA, 4% LAP) is loaded in a 1 mm wide glass container. The FPP sample is polymerized by a single flash (20 J) into a 1 mm slab. The CW sample is polymerized by UV-LED (0.4 mW cm^{-2}, 10 s) into a 1 mm slab.

By using the integrating sphere, the diffusive reflectance R_d, total reflectance R_t, diffusive transmittance T_d, and total transmittance T_t at 365 nm wavelength are measured. Then we used Inverse Adding-Doubling (IAD) algorithm to calculate the scattering coefficient of the samples. The executable program of IAD algorithm was acquired from https://omlc.org/software/iad/index.html, copyright 2017 Scott Prahl.

Acknowledgements

Chapter 2, in full, is a reprint of the published article, “High-fidelity 3D printing using flashing photopolymerization”, S. You, P. Wang, J. Schimelman, H.H. Hwang, S. Chen. *Additive Manufacturing*, 2019. The dissertation author was the primary investigator and author of this paper. This work was supported in part by National Institutes of Health (R21AR074763, R33HD090662, and R01EB021857) and National Science Foundation (NSF) (CMMI-1644967). Part of the work is performed at San Diego Nanotechnology Infrastructure (SDNI) of UCSD, a member of the National Nanotechnology Coordinated Infrastructure (NNCI), which is supported by NSF (Grant ECCS-1542148).

Supplementary Information

Figure 2.S1 shows close-up views of the images in Figure 2.2. Visual observation makes it clear that the fabrication resolution of the CW mode decreases as exposure dose increases. By comparison, the FPP mode can maintain fine resolution even at excessive exposure doses.

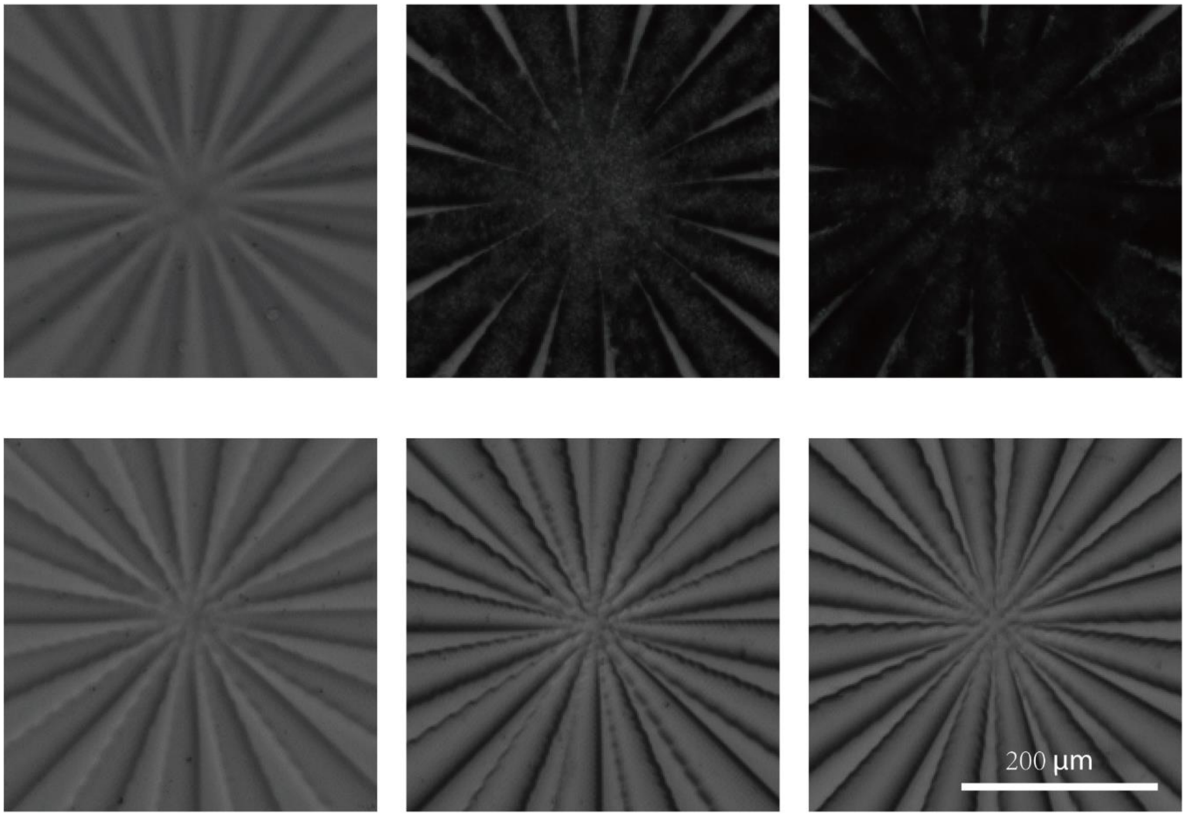

Figure 2.S1| Zoom-in view of images in Figure 2.2. First row: patterns printed with CW exposure. Second row: patterns printed with FPP.

The slab samples for scattering measurement in Figure 2.3 have different visual appearances. The CW sample is much more opaque than the FPP sample. Figure 2.S2 shows the appearance of the two samples.

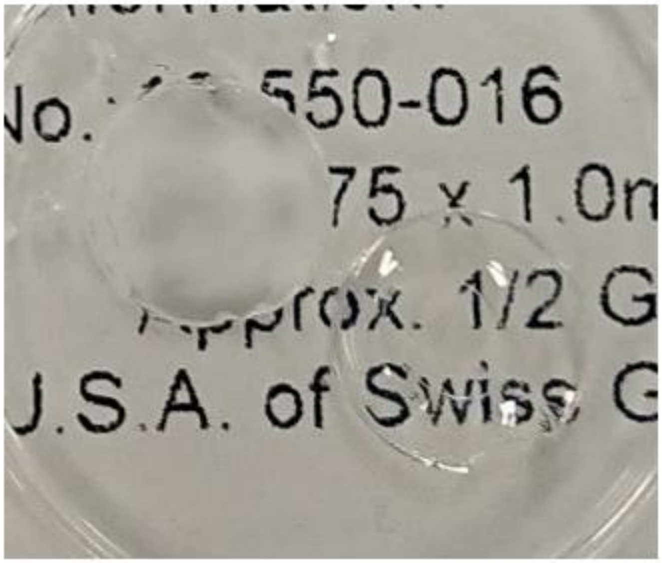

Figure 2.S2| Appearance of the slab samples. The upper-left disc is made by CW exposure, and the lower-right disc is made by FPP exposure.

In order to visualize the opacification during photopolymerization in real-time, a high-speed camera was used to record the change of Tyndall effect on a photopolymerizable material. The material is aqueous 50% (v/v) PEGDA with 4% (w/v) LAP added as the photoinitiator. The prepolymer solution was loaded in a cuvette, and a He-Ne laser beam (633 nm) was shone through the solution such that the beam path and its shape was visible to the high-speed camera (Figure 2.S3). Finally, either a UV-LED light source (365 nm) or a xenon flash tube was set up near the cuvette to photopolymerize the PEGDA solution.

The UV-LED was record to have a light intensity of 12 mW cm^{-2} at the cuvette. The xenon flash tube has a broad emission spectrum encompassing from UV to NIR, with an electrical energy per flash of 40 J. However, we did not have a suitable instrument to measure the actual light intensity of the flash illumination at the cuvette. The high-speed camera was set to record at 500 fps, with a 2 ms exposure time for each frame. The image was recorded at monochromatic 16-bit bit-depth, and the gray scale value ranged from 0 to 65535. The original recorded grey scale value was used as the intensity in Figure 2.S4 (b) and (d). The beginning and ending time of exposure was determined based on the subtle change of background brightness, since the long pass filter does not completely block the light from the LED or flash tube.

We used either a 2.3-second CW exposure from the UV-LED or a single flashing exposure from the xenon flash tube to polymerize the prepolymer solution. The change of shape of the laser beam inside the PEGDA was recorded, as shown in Figure 2.S4(a) for CW exposure and in Figure 2.S4(c) for FPP exposure. The intensity profiles along the green arrows were plotted in Figure 2.S4(b) for CW exposure and in Figure 2.S4(d) for FPP exposure.

As was expected, light scattering increased during photopolymerization in both cases. In the CW exposure case, scattering steadily increases during the 2.3-second exposure, and at the end of exposure period the material is highly scattering, with scattering still continuing to increase even after the exposure period. In the FPP exposure case, the first 50 milliseconds of the recorded video was strongly interfered with by the intense flashing, and laser beam shape was unable to be observed, but at the end of the flash (t = 50 ms), the material scattering has increased only slightly. The scattering keeps increasing in the next several hundreds of milliseconds.

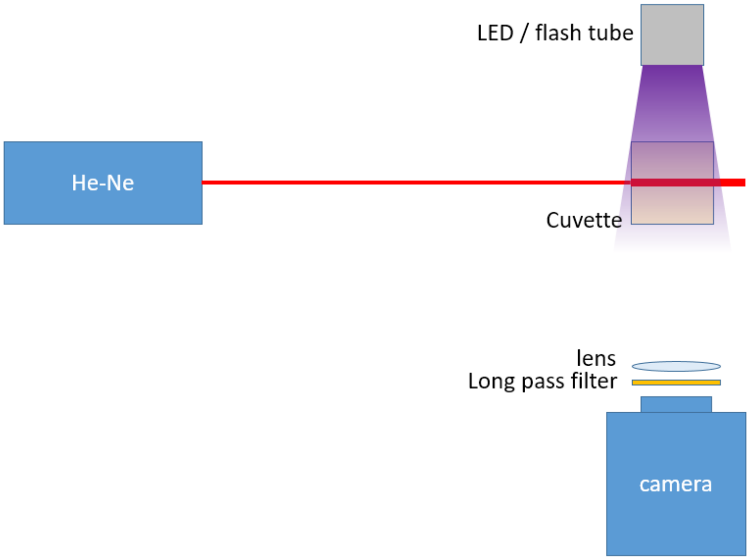

Figure 2.S3| Optical setup for visualizing the opacification during polymerization.

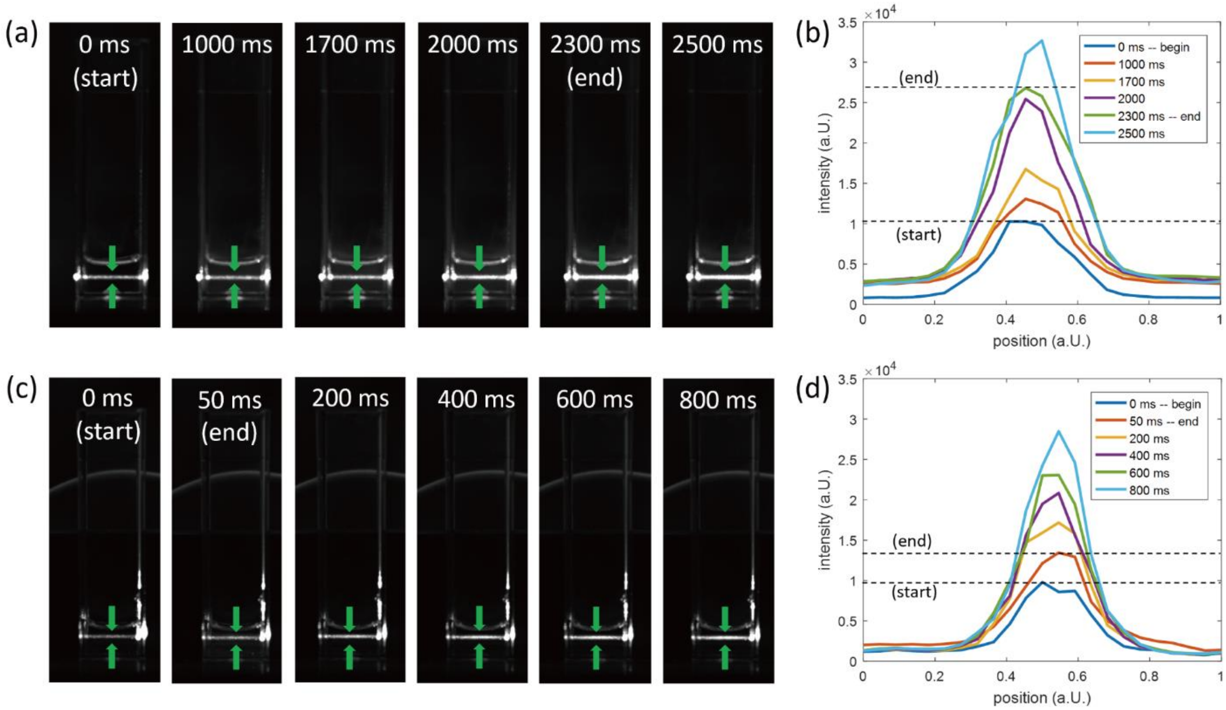

Figure 2.S4| Scattering changes during polymerization. (a) Images of Tyndall effect at different time point of CW exposure. (b) Intensity profile of the laser beam along the green arrows in (a). (c) Images of Tyndall effect at different time points of FPP exposure. (d) Intensity profile of the laser beam along the green arrows in (c).

In the simulation, the type and concentration of photoinitiator, and the illumination intensity are given, thus the free radical generation rate can be calculated, then the kinetics simulation can be performed with Equations (2.1) – (2.11). Here is the method to convert the illumination intensity into free-radical generation rate.

The free radical generation rate r_i is proportional to the quantity of photons absorbed per unit time per unit volume N_{abs}, and to the quantum efficiency Φ:

$$r_i = 2\Phi N_{abs} \tag{2.S1}$$

According to Beer-Lambert law, the molar quantity of photons absorbed, N_{abs} per unit volume is related to the material absorbance A, light power intensity I, sample thickness L, and photon frequency ν:

$$N_{abs} = (1 - 10^{-A}) \cdot \frac{I}{N_A h\nu} \cdot \frac{1}{L} \tag{2.S2}$$

where N_A and h are Avogadro constant and Plank constant.

The material absorbance A is determined by the molar extinction coefficient ε, the photoinitiator concentration C (neglecting monomer absorption), and the sample thickness L.

$$A = \frac{\varepsilon CL}{\ln(10)} \tag{2.S3}$$

Combining Equations (2.S1) – (2.S3), the free radical generation rates at different illumination intensities can be calculated. Table 2.S1 lists the corresponding free radical generation rates associated with the light illumination intensities used in the simulation.

Table 2.S1| Free radical generation rates and corresponding illumination intensity.

Free Radical Generation Rate	Light Intensity
0.0005 mol L^{-1} s^{-1}	1.1 mW cm^{-2}
0.001 mol L^{-1} s^{-1}	2.2 mW cm^{-2}
0.002 mol L^{-1} s^{-1}	4.3 mW cm^{-2}
50 mol L^{-1} s^{-1}	106.5 W cm^{-2}
55 mol L^{-1} s^{-1}	117.2 W cm^{-2}
60 mol L^{-1} s^{-1}	127.8 W cm^{-2}

Reference

[1] J.R. Tumbleston, D. Shirvanyants, N. Ermoshkin, R. Janusziewicz, A.R. Johnson, D. Kelly, K. Chen, R. Pinschmidt, J.P. Rolland, A. Ermoshkin, E.T. Samulski, J.M. DeSimone, Continuous liquid interface production of 3D objects, Science. 347 (2015) 1349–1352.

[2] C. Sun, N. Fang, D.M. Wu, X. Zhang, Projection micro-stereolithography using digital micro-mirror dynamic mask, Sensors and Actuators A: Physical. 121 (2005) 113–120.

[3] R. Gauvin, Y.-C. Chen, J.W. Lee, P. Soman, P. Zorlutuna, J.W. Nichol, H. Bae, S. Chen, A. Khademhosseini, Microfabrication of complex porous tissue engineering scaffolds using 3D projection stereolithography, Biomaterials. 33 (2012) 3824–3834.

[4] L.-H. Han, J.A. Easley, C.J. Ellison, S. Chen, Fluorinated Colloidal Emulsion of Photochangeable Rheological Behavior as a Sacrificial Agent to Fabricate Organic, Three-Dimensional Microstructures, Langmuir. 26 (2010) 6108–6110.

[5] P. Soman, B.T.D. Tobe, J.W. Lee, A.A.M. Winquist, I. Singec, K.S. Vecchio, E.Y. Snyder, S. Chen, Three-dimensional scaffolding to investigate neuronal derivatives of human embryonic stem cells, Biomedical Microdevices. 14 (2012) 829–838.

[6] A.P. Zhang, X. Qu, P. Soman, K.C. Hribar, J.W. Lee, S. Chen, S. He, Rapid Fabrication of Complex 3D Extracellular Microenvironments by Dynamic Optical Projection Stereolithography, Advanced Materials. 24 (2012) 4266–4270.

[7] W. Zhu, X. Ma, M. Gou, D. Mei, K. Zhang, S. Chen, 3D printing of functional biomaterials for tissue engineering, Current Opinion in Biotechnology. 40 (2016) 103–112.

[8] W. Zhu, K.R. Tringale, S.A. Woller, S. You, S. Johnson, H. Shen, J. Schimelman, M.

Whitney, J. Steinauer, W. Xu, Rapid continuous 3D printing of customizable peripheral nerve guidance conduits, Materials Today. (2018).

[9] D.B. Berry, S. You, J. Warner, L.R. Frank, S. Chen, S.R. Ward, A 3D tissue-printing approach for validation of diffusion tensor imaging in skeletal muscle, Tissue Engineering Part A. 23 (2017) 980–988.

[10] W. Zhu, X. Qu, J. Zhu, X. Ma, S. Patel, J. Liu, P. Wang, C.S.E. Lai, M. Gou, Y. Xu, K. Zhang, S. Chen, Direct 3D bioprinting of prevascularized tissue constructs with complex microarchitecture, Biomaterials. 124 (2017) 106–115.

[11] X. Qu, W. Zhu, S. Huang, Y.-S. Li, S. Chien, K. Zhang, S. Chen, Relative impact of uniaxial alignment vs. form-induced stress on differentiation of human adipose derived stem cells, Biomaterials. 34 (2013) 9812–9818.

[12] J.-F. Xing, M.-L. Zheng, X.-M. Duan, Two-photon polymerization microfabrication of hydrogels: an advanced 3D printing technology for tissue engineering and drug delivery, Chemical Society Reviews. 44 (2015) 5031–5039.

[13] H.N. Chia, B.M. Wu, Recent advances in 3D printing of biomaterials, Journal of Biological Engineering. 9 (2015) 4.

[14] T.E. Brown, K.S. Anseth, Spatiotemporal hydrogel biomaterials for regenerative medicine, Chemical Society Reviews. 46 (2017) 6532–6552.

[15] P. Soman, D.Y. Fozdar, J.W. Lee, A. Phadke, S. Varghese, S. Chen, A three-dimensional polymer scaffolding material exhibiting a zero Poisson's ratio, Soft Matter. 8 (2012) 4946.

[16] P. Soman, J.W. Lee, A. Phadke, S. Varghese, S. Chen, Spatial tuning of negative and positive Poisson's ratio in a multi-layer scaffold, Acta Biomaterialia. 8 (2012) 2587–2594.

[17] A. del Campo, C. Greiner, SU-8: a photoresist for high-aspect-ratio and 3D submicron lithography, Journal of Micromechanics and Microengineering. 17 (2007) R81–R95.

[18] S. You, W. Zhu, P. Wang, S. Chen, Projection Printing of Ultrathin Structures with Nanoscale Thickness Control, ACS Applied Materials & Interfaces. 11 (2019) 16059–16064.

[19] R.B. Bird, W.E. Stewart, E.N. Lightfoot, Transport phenomena, John Wiley & Sons, 2007.

[20] M. Terazima, Y. Nogami, T. Tominaga, Diffusion of a radical from an initiator of a free radical polymerization: a radical from AIBN, Chemical Physics Letters. 332 (2000) 503–507.

[21] R.L. Donkers, D.G. Leaist, Diffusion of Free Radicals in Solution. TEMPO, Diphenylpicrylhydrazyl, and Nitrosodisulfonate, The Journal of Physical Chemistry B. 101 (1997) 304–308.

[22] W. Reed, L. Guterman, P. Tundo, J.H. Fendler, Polymerized surfactant vesicles: kinetics and mechanism of photopolymerization, Journal of the American Chemical Society. 106 (1984) 1897–1907.

[23] C.E. Carraher Jr, Introduction to polymer chemistry, CRC press, 2017.

[24] J.M.G. Cowie, V. Arrighi, Polymers: chemistry and physics of modern materials, CRC press, 2007.

[25] T. Scherzer, U. Decker, Real-time FTIR–ATR spectroscopy to study the kinetics of ultrafast photopolymerization reactions induced by monochromatic UV light, Vibrational Spectroscopy. 19 (1999) 385–398.

[26] J.-C. Auger, R.G. Barrera, B. Stout, Scattering efficiency of clusters composed by aggregated spheres, Journal of Quantitative Spectroscopy and Radiative Transfer. 79–80 (2003) 521–531.

[27] A. Seeboth, D. Lötzsch, E. Potechius, Phase transitions and phase separations in aqueous polyether systems, Colloid Polym Sci. 279 (2001) 696–704.

[28] J. Wu, Z. Zhao, C.M. Hamel, X. Mu, X. Kuang, Z. Guo, H.J. Qi, Evolution of material properties during free radical photopolymerization, Journal of the Mechanics and Physics of Solids. 112 (2018) 25–49.

[29] Y.-H. Hsueh, W.-C. Liaw, J.-M. Kuo, C.-S. Deng, C.-H. Wu, Hydrogel Film-Immobilized Lactobacillus brevis RK03 for γ-Aminobutyric Acid Production, International Journal of Molecular Sciences. 18 (2017) 2324.

[30] M. Mesradi, A. Genoux, V. Cuplov, D. Abi Haidar, S. Jan, I. Buvat, F. Pain, Experimental and analytical comparative study of optical coefficient of fresh and frozen rat tissues, Journal of Biomedical Optics. 18 (2013) 117010.

[31] S.A. Prahl, M.J.C. van Gemert, A.J. Welch, Determining the optical properties of turbid media by using the adding–doubling method, Applied Optics. 32 (1993) 559.

[32] C.N. Bowman, C.J. Kloxin, Toward an enhanced understanding and implementation of photopolymerization reactions, AIChE Journal. 54 (2008) 2775–2795.

[33] M.D. Goodner, H.R. Lee, C.N. Bowman, Method for determining the kinetic parameters in diffusion-controlled free-radical homopolymerizations, Industrial & Engineering Chemistry Research. 36 (1997) 1247–1252.

[34] M.D. Goodner, C.N. Bowman, Modeling primary radical termination and its effects on autoacceleration in photopolymerization kinetics, Macromolecules. 32 (1999) 6552–6559.

[35] M.R. Gleeson, J.T. Sheridan, Nonlocal photopolymerization kinetics including multiple termination mechanisms and dark reactions Part I Modeling, Journal of the Optical Society of America B. 26 (2009) 1736.

[36] M.D. Goodner, C.N. Bowman, Development of a comprehensive free radical photopolymerization model incorporating heat and mass transfer effects in thick films, Chemical Engineering Science. 57 (2002) 887–900. doi:10.1016/S0009-2509(01)00287-1.

[37] M. Buback, Free-radical polymerization up to high conversion. A general kinetic treatment, Die Makromolekulare Chemie. 191 (1990) 1575–1587.

[38] B.D. Fairbanks, M.P. Schwartz, C.N. Bowman, K.S. Anseth, Photoinitiated polymerization of PEG-diacrylate with lithium phenyl-2,4,6-trimethylbenzoylphosphinate: polymerization rate and cytocompatibility, Biomaterials. 30 (2009) 6702–6707.

Chapter 3 Mitigating Scattering Effects Using Machine Learning

Abstract

When using light-based 3D printing methods to fabricate functional micro-devices, unwanted light scattering during the printing process is a significant challenge to achieve high resolution fabrication. We report the use of a deep neural network (NN)-based machine learning (ML) technique to mitigate the scattering effect, where our NN was employed to study the highly-sophisticated relationship between the input digital masks and their corresponding output 3D printed structures. Furthermore, the NN was used to model an inverse 3D printing process, where it took desired printed structures as inputs and subsequently generated grayscale digital masks that optimized the light exposure dose according to the desired structures' local features. Verification results showed that using NN-generated digital masks yielded significant improvements in printing fidelity compared to using masks identical to the desired structures.

3.1 Introduction

Light-based 3D printing methods using digital light processing (DLP) technique,[1,2] such as projection micro-stereolithography (PμSL),[3] dynamic optical projection stereolithography (DOPsL),[4] continuous liquid interface production (CLIP)[5] and microscale continuous optical bioprinting (μCOB),[6] have emerged as promising tools for fabricating functional devices such as tissue engineering scaffolds,[6,7] implantable medical devices,[8,9] microfluidic devices,[10] microsensors,[11] and micro robots[12] for a variety of applications in medicine, manufacturing, and consumer products due to their rapid fabrication speed and micron-scale fabrication resolution. For these applications, high-fidelity fabrication for the 3D printed part as compared to its intended design is highly-desired. However, functional devices are often made of a mixture of polymeric materials and functional elements such as cells,[7,10] micro/nano particles,[11,12] and micelles. These elements often scatter the incoming light during the photopolymerization process, and additionally the polymer materials themselves may have turbidity, form crystallites, or even micropores during and/or after polymerization, which can also give rise to light scattering. [13] Such light scattering ultimately reduces fidelity in the final product due to suboptimal polymerization of both the intended and unintended design areas. (**Figure 3.S1**) Therefore, it is challenging to achieve high-fidelity and fine resolution in printing turbid materials using light-based 3D printing methods. Generally, the fabrication resolution and fidelity achievable in turbid materials are worse than in optically-clear materials, thus it would take more effort to optimize proper exposure dosages during printing. Such process optimization adds significant cost and time for product development, making it especially onerous in the case of 3D bioprinting where expensive cells are involved in the printing process to make biological tissues.

In most implementations of light-based 3D printing, binary digital masks identical to the desired structures are used. We will term these "identical masks," where in binary fashion, a 1 (shaded white) represents light exposure and 0 (shaded black) represents no light exposure. However, directly applying these binary identical masks will not produce the exact copies of the desired structures due to challenges such as the aforementioned light scattering effect, thus motivating us to modulate the input mask in ways that might sufficiently compensate. With advances in DLP techniques, patterns utilizing grayscale values (ranging from 0 to 255 instead of binary 0 & 1) can be employed in light-based 3D printing. We expect that by using grayscale masks which are not necessarily identical to the desired patterns could compensate or counterbalance the effect of scattering, thus resulting in 3D printed structures as designed. Unfortunately, the light scattering properties of the prepolymer materials are complicated (e.g. vary during printing and over time), making it difficult to *a priori* model the scattering and photopolymerization behavior of these materials as well as calculate the grayscale digital masks for 3D printing.

Recent advances of machine learning technologies based on deep neural networks (NNs) have successfully demonstrated their capability in assisting industrial manufacturing.[14] For example, researchers have reported the use of NN-based machine learning (ML) technique to help optimize the processing parameters of inkjet-based 3D printing[15] and fused filament fabrication (FFF)-based 3D printing.[16,17] However, to the best of our knowledge, using ML to assist in light-based 3D printing has not yet been reported. Moreover, it is far more complicated for NN to optimize a 2D image than to optimize a few scalar parameters.

Here we report the use of deep NN-based ML to study the 3D printing behavior of light scattering materials and to generate grayscale digital masks to mitigate the effect of scattering in light-based 3D printing. A NN is trained to model the inverse process of 3D printing, where the input is the desired structure, and the output is the grayscale digital mask. We used 300 mask-structure pairs, which were produced by an in-house DLP-based 3D printer, to train the NN. Masks generated by the NN were then used to 3D print the desired target structures. Finally, we compared the printed structures created from NN-suggested masks to the structures printed from traditional identical masks. The results show that higher fabrication resolution and better fidelity can be achieved by our ML assisted approach.

3.2 Experimental Setup

3.2.1 Modeling DLP-based 3D Printing

Figure 3.1a shows the setup of a DLP-based 3D printer in this work. A light source of 405 nm wavelength illuminates the digital micromirror device (DMD). The DMD chip consists of 4 million of micro-mirrors, which can be individually controlled to flip toward two different directions, thus displaying a pattern. The reflected light is patterned by the DMD, and is projected onto the liquid state prepolymer solution by lenses. A computer is used to control the DMD to display the cross-sections at different position of the 3D model. Upon light exposure, the photosensitive material polymerizes, forming a thin layer of solid structure. The motorized stage brings the solidified part up by a layer thickness, which is typically tens to hundreds of microns, then unpolymerized material refills the gap. The DMD then displays the next cross-section and photopolymerizes the next layer. By repeating this process, a 3D construct is thus printed. Figure 3.1b and 1c show the scanning electron microscopy (SEM) images of the printed structures using this 3D printer.

The whole multi-layer 3D printing process can be discretized into multiple single-layer prints, which is the focus of this study.

There are several tunable variables for a single-layer print: 1) the digital mask determines the shape of the exposed area; 2) the exposure duration, and 3) the light intensity define the exposure dose. We can combine these variables into a “generalized digital mask”, where the grayscale value of any given pixel on the digital mask represents the local exposure dose.

We abstracted the 3D printer as a nonlinear time-invariant system. The input of the system is the digital mask, which is a 512 x 512 pixel grayscale image, where the grayscale value represents the local exposure dose. The output of the system is the single-layer 3D printed structure, which is represented by a 512 x 512 binary image, where a 1 represents a solidified area and 0 represents a void area.

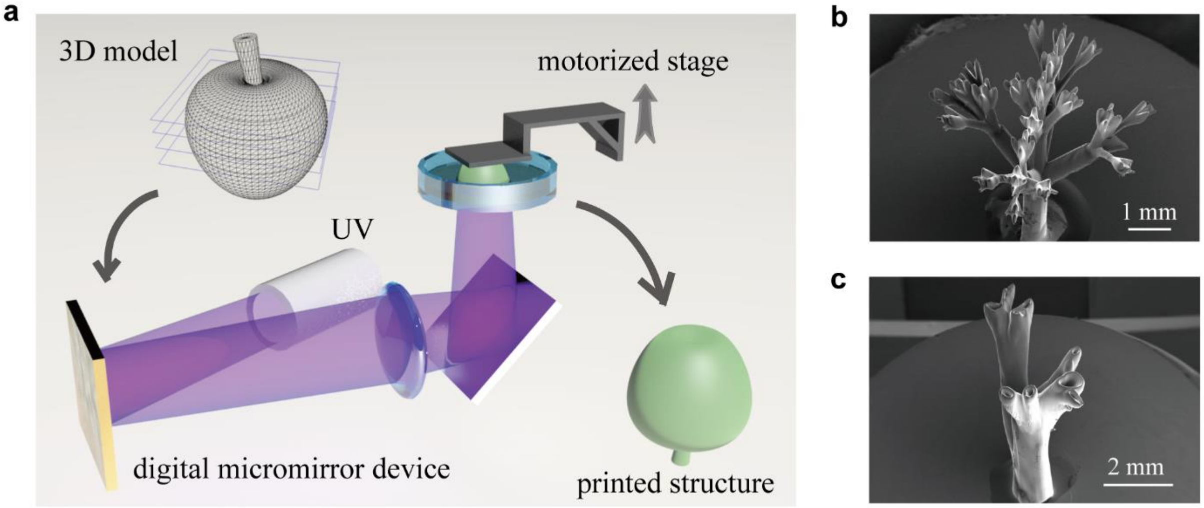

Figure 3.1| Schematic of the 3D printer and the printed structures. a The DLP-based 3D printer setup. **b** SEM image of a printed 3D "fractal tree". **c** SEM image of a printed 3D "blood vessel".

3.2.2 Neural Network

The NN models the inverse process of 3D printing, which takes a 512 x 512 binary image (the desired printed structure) as an input and generates a 512 x 512 grayscale image (the digital mask) as the output (**Figure 3.2**a). We used mask-structure pairs from the 3D printer to train the NN. The digital masks are grayscale images of an assortment of random shapes, e.g. checkerboards, discs, and rectangles (Figure 3.S2). The 3D printer then used these masks to print their corresponding structures. The exposure duration was fixed to 5 seconds. During printing, the actual light intensity of the maximum grayscale value (255) was measured to be 5.6 mW/cm^2, and 0 mW/cm^2 for the minimum grayscale value (0). The light source was a light emitting diode (LED) centered at 405 nm wavelength. The prepolymer material was 50% (V/V) poly(ethylene glycol) diacrylate (PEGDA, Mn = 575) aqueous solution, with 1% (w/V) lithium phenyl-2,4,6-trimethylbenzoylphosphinate (LAP) as photoinitiator, and 0.1% (w/V) glass microbeads (diameter = 4 µm) as scattering particles. The microscope images of the printed structures are then processed into binary images with the use of custom code. We collected 300 mask-structure pairs, which were then augmented to 900 pairs by random rotation about the image center. The detailed training method is available in the Method section.

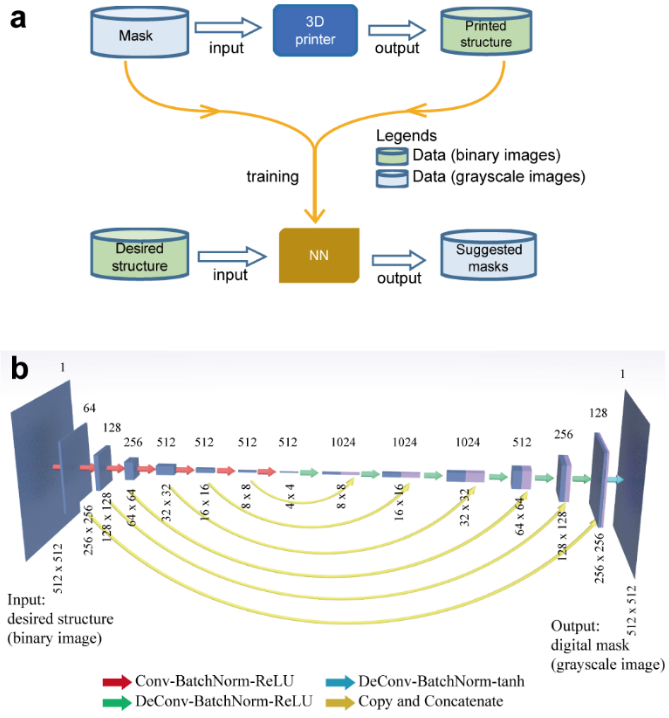

Figure 3.2| Data flow and architecture of the neural network. a The 3D printer takes the digital masks as input, and output the printed structure. The neural network takes the desired structure as input, and output the suggested digital mask. The input and output of the 3D printer are used to train the neural network. **b** The neural network has a 14-layer convolutional neural network architecture with U-Net style skip connections. The rectangles represent the feature maps, with their feature resolution denoted at the bottom, and their feature channel number denoted on the top.

The architecture of our NN is adapted from the generator design in image-to-image style transfer which is an encoder-decoder fully convolutional network with U-Net style skip connections[18–20], a schematic depiction of which is shown in Figure 3.2b. We also introduced partially cycle-consistent image-to-image translation loss to better meet our task characteristics which will be explained in the Method section. The NN consists of 14 building blocks, where each building block is a convolution or deconvolution layer followed by batch normalization[21] and the activation function. The convolution layers in the first seven building blocks are set with stride

2 to down-sample the features, while the deconvolution layers in the last seven building blocks up-sample the feature using stride 2 to recover the output image to the original resolution. The activation function of the first thirteen building block is a rectifier linear unit (ReLU) function[22]. The last building block uses a hyperbolic tangent function (tanh) as the activation function in order to restrict the output value in the range of -1 and 1, which is then linearly mapped to the grayscale value ranging from 0 to 255. There are also skip connections that copy the feature maps from the down-sampling process and append to the corresponding feature maps of up-sampling process, allowing the network to learn more precise local information.

3.3 Methods

Our objective is to find proper masks according to any target structure. Intuitively, we can achieve this objective by training the NN alone with the mask-structure data pairs we have made. The trained NN will learn to mimic the mapping from our dataset. However, we have limited data to train the NN, which prevents our NN from generalizing well on the entire structure space.

To address this challenge, we introduce a slave NN which learns the mapping of the 3D printer (the mapping from the mask to the structure). The slave NN has a similar architecture as the master NN as shown on Figure 3.2b, and the difference is that the last layer of the slave NN has two output channels and the tanh is replaced with a softmax function. We train the master NN, which models the inverse process of 3D printing (i.e., from the structure to the mask), based on not only the data generated by the actual 3D printer but also the extra information provided by the slave NN, thus we can allow the master NN to fit to a broader and smoother distribution of data.

We formulate the training process of the NN as solving a minimization problem with the following objective function. For simplicity in expression, we define a function S: X → Y, which represents the slave NN that learns the mapping from any grayscale mask x to the binary structure y. In the optimal case, the slave NN behaves exactly as the 3D printer, which is denoted as S^*. Similarly, we denote M: Y → Z as the transformation of master NN that learns a mapping from the desired binary structure y to a suggested grayscale mask z.

We first look at the slave NN. Since we want the slave NN to mimic the behavior of a 3D printer, i.e. we want the output of S to be as close as the output of S^* for the same input x, the ideal objective function for the slave NN can be expressed as **Equation (3.1)**

$$L^*_{Slave} = E_x[loss(S(x), S^*(x))] \tag{3.1}$$

where $loss$ can be any loss function.

However, we only have limited access to the 3D printer S^* due to the cost and time, and we decide therefore only to use the data pre-generated by S^* for training, which are the 300 mask-structure pairs. We denote the training dataset as (X,Y), such that any (x,y) chosen from (X,Y) satisfies $S^*(x) = y$. According to this data set, we can come up with a new objective function as **Equation (3.2)**

$$L_{Slave} = E_{x,y}[loss(S(x), y)] \tag{3.2}$$

This objective (Equation (2)) is ultimately the same as the ideal objective (Equation (3.1)) if we have unlimited data. However, due to the limited amount of data we have, we expect the trained S to have relatively high variance. This variance can be a form of useful noise to help generalize the master NN, which will be trained using this slave NN.

Next, we are looking at the master NN. We define the ideal objective equation for optimizing the master NN as **Equation (3.3)**

$$L^*_{Master} = E_y[loss(S^*(M(y)), y)] \tag{3.3}$$

We can see that M is trained to minimize the error between the actual output structure and the desired structure. Again, we use data set (X,Y) instead of S^* during training. According to this data set, we can come up with a new objective function as **Equation (3.4)**

$$L_{Master,1} = E_{x,y}[loss(M(y), x)] \tag{3.4}$$

In the optimal case $M(y) = x$. Since we know $S^*(x) = y$, we will have $S^*\big(M(y)\big) = y$ for the y's in set Y. This means the new objective leads to the same optimized M as the ideal objective (Equation (3)). However, we will have a severe generalization issue with this new objective. Imagine a small disturbance is applied to the input y, a well generalized $M(y)$ will then output an image $\tilde{x}$ close to x. However, notice that S^* can potentially be very non-linear, which means that $S^*(\tilde{x})$ can be very different from $S^*(x)$ even though $\tilde{x}$ is very close to x. We may then interpret this effect as having relatively high variance if $S^*(\tilde{x})$ is not smooth enough. Due to this issue, we need to find a way to better generalize M.

Let's take a look at another way to address the ideal master NN objective (Equation (3.3)) which is to replace S^* by its approximation, S. The objective becomes **Equation (3.5)**

$$L_{Master,2} = E_y[loss(S(M(y)), y)] \tag{3.5}$$

This objective has the benefit of generalizing well thanks to the information previously learned from S. The disadvantage is the cumulated error in the term $S(M(y))$. Notice that both S and M in this objective are neural networks and will potentially have some error even after convergence. If we use this $L_{Master,2}$ as objective, the calculation of $S(M(y))$ will suffer from the error of both S and M, making the trained M biased according to the error from S.

Since the two feasible master NN objective functions either have small bias or small variance, we decide to combine them together. The resulting objective combining $L_{Master,1}$ and $L_{Master,2}$, (Equation (4,5)), becomes **Equation (3.6)**

$$L_{Master} = E_y[loss(S(M(y)), y)] + \lambda * E_{x,y}[loss(M(y), x)] \tag{3.6}$$

where λ is a tunable weight term to control the tradeoff between bias and variance. Notice that the first term is also a cycle-consistent loss, which is empirically proved to add performance to the network when the data set is having this cycle-consistency property[23–25].

We decide to train S and M simultaneously instead of fully training S before starting to train M. Our final objective function for both master NN and slave NN therefore is the combination of Equation (3.2) and Equation (3.6).

$$L = E_y[loss(S(M(y)), y)] + \lambda_1 * E_{x,y}[loss(M(y), x)] + \lambda_2 * E_{x,y}[loss(S(x), y)] \tag{3.7}$$

The advantage of training the master and slave NN simultaneously using **Equation (3.7)** is demonstrated in **Figure 3.S3**, where only training the master NN with Equation (4) is used for comparison.

Following this approach, we can interpret S as a gradually reducing noise term, and this noise will make the output of S to bounce around the ground truth after convergence. We find this noise useful to generalize M to fit the distribution of varying output of S and avoid overfitting M to a deterministic output of S. We decide not to apply other commonly used noises, like adding Gaussian noise to the input or applying dropout to the network weights during training [26], while updating M. In terms of S, we add Gaussian noise to the input with zero mean, initial standard deviation 0.1, and 0.97 decay rate at each iteration.

In terms of hyperparameter choices, we use L1 norm as loss function for comparing grayscale images, and we use cross-entropy loss for the loss between binary images. The tradeoff weight λ_1 is set to 0.1 and λ_2 is 1.

Consider the small amount of training data we had access to, we implemented data augmentation techniques to better train the networks. Typical image processing tasks use hierarchical algorithm [27] or use data augmentation to improve the learning of many invariance properties such as shift invariance, rotational invariance, and deformation invariance[19,20,28]. We augment our data by applying rotation and flipping with respect to the image center. In our implementation, the 300 pairs of data were augmented to 900 pairs following this method.

We trained both networks under PyTorch[29] framework with mini-batch stochastic gradient descent (SGD) using Adam solver[30]. The batch size is set to 10 due to the memory limit (8 GB). The momentum parameters are set to (0.9, 0.999), and the learning rate is 0.00001. All network model weights and biases are initialized using random samples from normal distribution with zero mean and 0.02 standard deviation. The whole training process took six and a half hours on a personal computer with a GTX 1070Ti discrete graphics processing unit (GPU). Once trained, the NN takes only a few seconds to calculate an output digital mask on a personal computer, and the speed is about ten times faster when utilizing the GPU. The training error curve is shown in **Figure 3.S4**.

3.4 Results and Discussion

To evaluate our ML method, we designed several target structures that were never used in the course of training the NN. The NN-suggested digital masks for these targets, after which we then used our 3D printer to print the structures using these masks and compare them to the targets.

As shown in **Figure 3.3**, the NN-suggested masks (Figure 3.3b) are not necessarily identical to the desired structure (Figure 3.3a). Compared to the traditional “identical masks”, the NN-suggested masks show significant use of grayscale variation and local feature deformation. 3D printing using the NN-suggested masks resulted in structures (Figure 3.3c) that more closely match our desired structures. We find that the NN-suggested mask is able to compensate for the scattering effect by ‘stretching out’ at the corners and ‘squeezing in’ at the edges, as shown in Figure 3.3d. The NN’s behavior matches our human intuition of how we would counter the scattering effect.

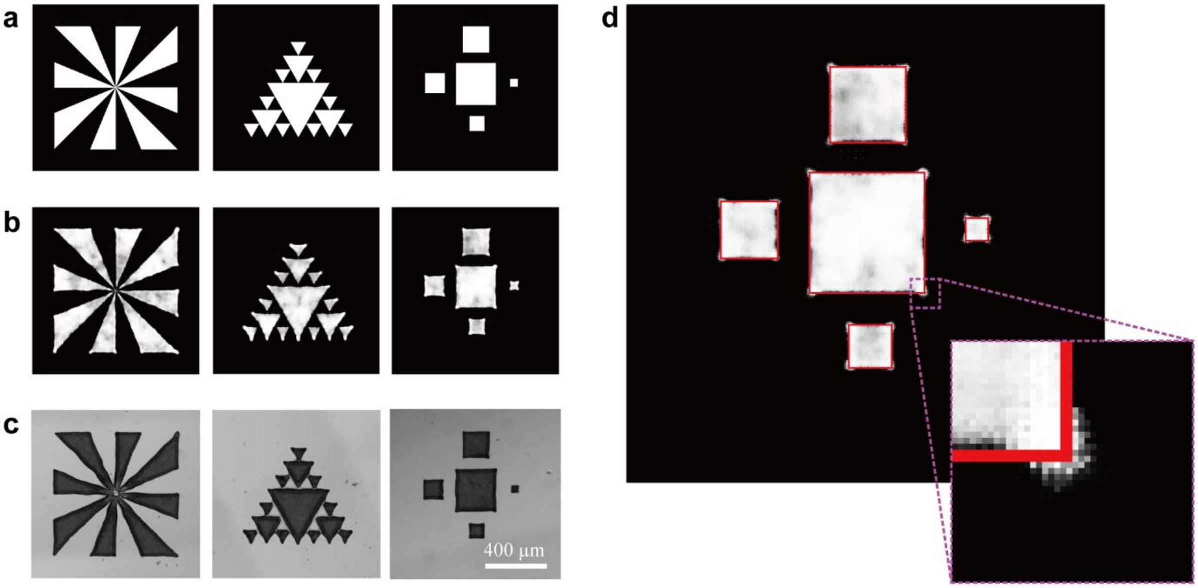

Figure 3.3| Comparison of the targets, the NN-suggested masks, and the microscopic images of the printed structures. a The target structures. **b** The NN-suggested masks for the targets. **c** The actual printed structures using the masks from **b**. **d** The NN-suggested mask overlaid with its target (shown as red contour).

More importantly, using the NN-suggested mask, we can reach a printing fidelity that cannot be achieved by using traditional “identical masks”. Traditionally, people tend to optimize the printing process by only tuning the exposure dose but keep using “identical mask”. To showcase the fidelity achievable with our method, we 3D printed and then compared the same target shape using both the NN-suggested masks as well as the traditional “identical masks.” For the traditional “identical masks,” we used exposure doses of 50% (2.8 mW/cm^2), 75% (4.2 mW/cm^2), and 100% (5.6 mW/cm^2) to simulate how an operator might optimize the 3D printing by tuning the global exposure dose.

Figure 3.4 shows the printed results of several targets using traditional “identical masks” at different exposure doses, or using the NN suggested masks. These targets include simple geometries as well as complex shapes. For all of these targets, the NN suggested masks yield the best printing fidelity, and are able to fabricate the most fine features such as sharp corners.

Figure 3.5 shows the overlaid contours of part of the printed structures in Figure 3.4. White contours represent the target structure; red contours represent the structures printed using NN-suggested masks; and the blue, green, and yellow contours represent the structures printed using the “identical masks” at 50%, 75%, and 100% exposure doses, respectively. Compared to the targets, the blue (50% dose) structures are shrunken considerably compared to the target (Figure 3.5d), indicating under-exposure condition; while the yellow (100% dose) structures are expanded well beyond the target structure (Figure 3.5f), indicating over-exposure. The green 75% dose structures expand at the edges but also shrink at the corners, thus indicating over-exposure at some locations and under-exposure at others (Figure 3.5e). This suggests that by using an “identical mask”, we cannot achieve proper exposure across the entire printing area.

The NN-suggested masks digitally individualize the local exposure dose depending on the local feature, hence an optimized map of exposure doses can be achieved across the entire printing area. We can see from Figure 3.5a-g that the red (AI-suggested) contours best match the targets. Significantly, fine features such as sharp corners seem particularly well-preserved. Thus, the NN-suggested masks outperform the “identical masks”.

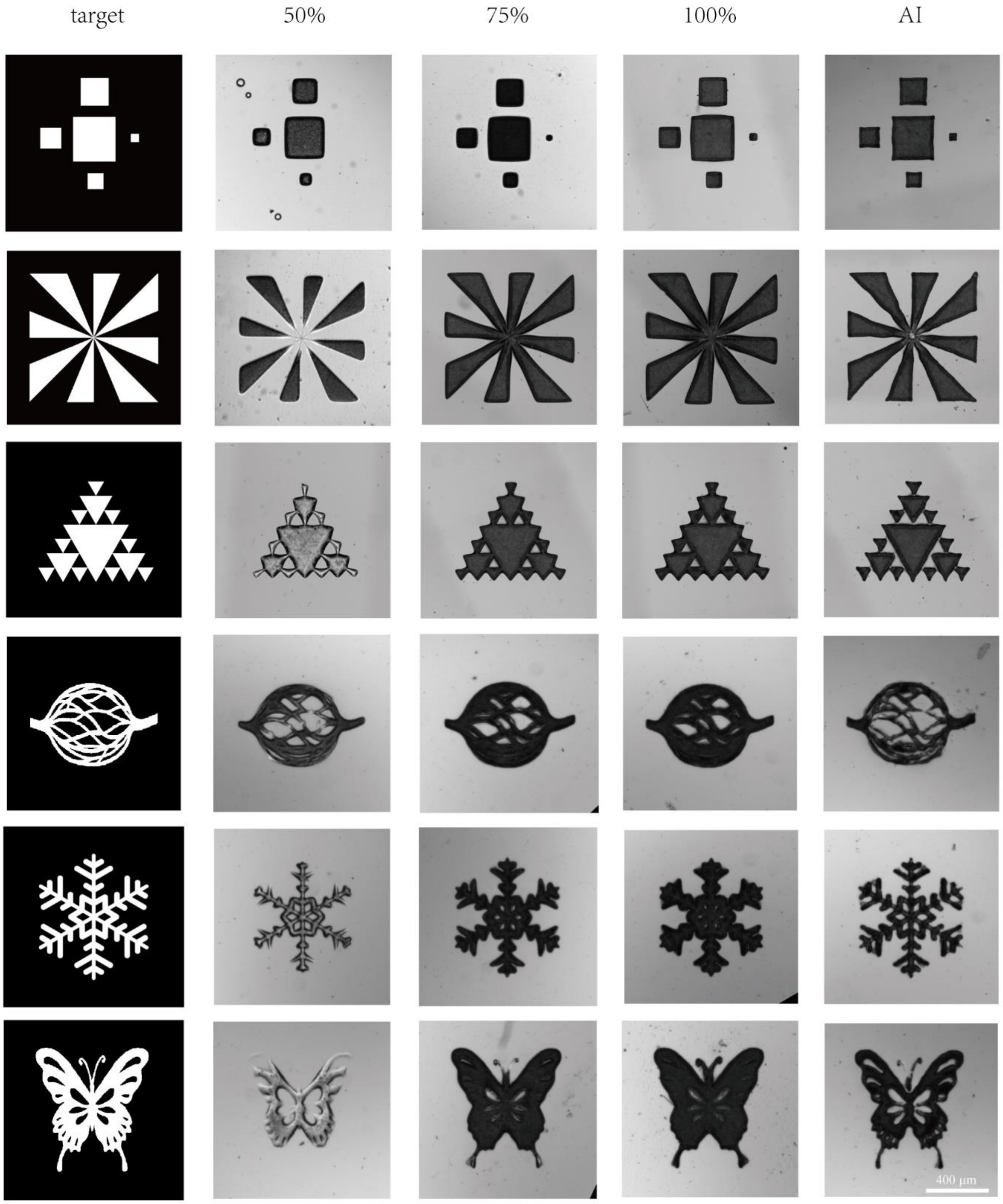

Figure 3.4| Printed structures using NN-suggested masks and identical masks. The first column is the target structures (designs). The second to forth columns are the printing result using the identical masks at 50%, 75%, and 100% exposure dose. The fifth column uses the NN-suggested masks.

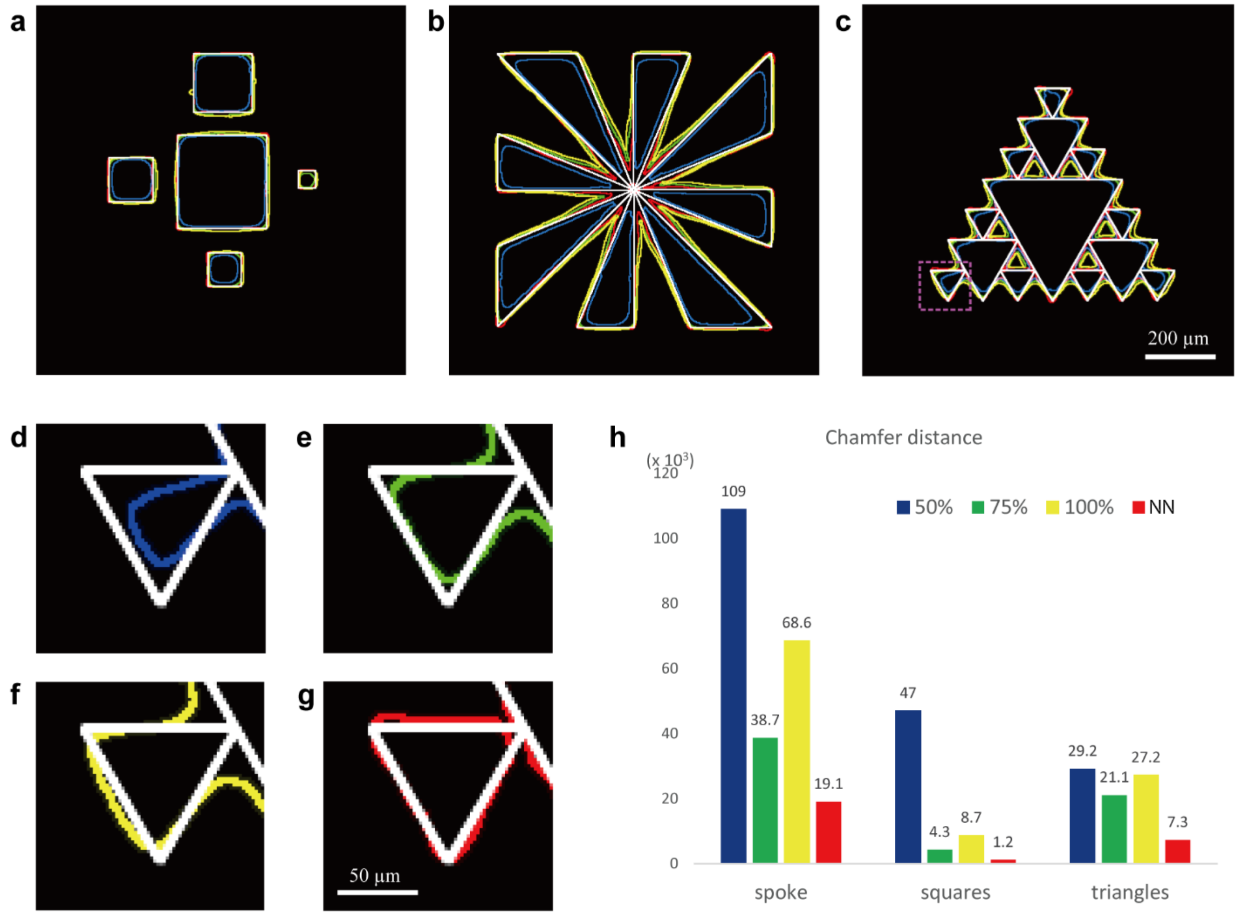

Figure 3.5| Printed structures using NN-suggested masks and identical masks. a-c are overlaid contours of the structures printed under different conditions. The white contours are the target structures. The red contours are the structures printed using NN-generated mask. The yellow, green, and blue contours represent the structures printed using identical masks with 100%, 75%, and 50% exposure dose, respectively. **d-g** are zoom-in views in the dashed frame in C, where the contours of the structures printed under four different conditions are isolated. **h** Chamfer distances between the printed structures and the desired targets.

In order to quantitatively evaluate the printing fidelity of the printed structures shown in Fig 3.5a-c, we compare those printed structures with their targets using Chamfer distance defined by **Equation (3.8)**[31].

$$Chamfer(P,Q) = \sum_{p\in P} \min_{q\in Q} \|p-q\|_2^2 + \sum_{q\in Q} \min_{p\in P} \|p-q\|_2^2 \tag{3.8}$$

In Equation (3.8), P and Q are the two binary images (or, two sets of non-zero pixels) we compare, p and q are the positions of individual non-zero pixels from the corresponding sets.

If a pair of images have a greater similarity, they have a smaller Chamfer distance. The calculated Chamfer distances between the 12 printed structures and their corresponding targets are shown in Figure 3.5h. The index suggests that using the NN-suggested mask, we can achieve better printing fidelity, which matches our qualitative evaluation.

The evaluation results have shown that our ML approach can help to address the scattering issue in light-based 3D printing, achieving a better fabrication fidelity and resolution than traditional non-ML method. It should be noted that the NN we presented does not take the material properties as input variables. Therefore, the NN should be trained individually for different materials. However, we believe that our method and the NN architecture can be applied to different materials to address the scattering problem in light-based 3D printing.

3.5 Conclusions

We have successfully demonstrated the use of ML to assist light-based 3D printing. When using turbid materials to fabricate functional devices, the printing fidelity deteriorates due to light scattering. The NNs allow us to study the relationship between the input digital mask and the actual output printed structure. Using the image-to-image fully convolutional NN that takes the desired structure as input and the grayscale digital mask as output, we succeeded in training the NN with a notably small amount of data (300 original mask-structure pairs). After training, the NN provides a digital mask with digitally optimized light dose map. Compared to traditional “identical masks”, the NN-suggested masks mitigate the scattering effect and enable better fabrication resolution and fidelity. Such intelligent advice empowered by ML could minimize the trial-and-error inherent in optimizing printing parameters, thus significantly reducing the costs across the board for time, labor, resources, customized parts, and time-to-delivery. We expect that this method can be applied to light-based 3D bioprinting, where complex 3D scaffolds embedding live cells with micron-scale features to mimic the native biological tissue are highly desired. This will further create a new paradigm for 3D bioprinting of functional organs and tissues due to expensive cell sources, patient-specific design, and required microscale printing resolution.

Acknowledgements

Chapter 3, in full, is a reprint of the unpublished article, “Mitigating scattering effects in light-based 3D printing using machine learning”, S. You, J. Guan, J. Alido, H.H. Hwang, L. Kwe, R. Ro, H. Su, S. Chen. The dissertation author was the primary investigator and author of this paper. This work was supported in part by National Institutes of Health (R01EB021857, R21 AR074763, R33HD090662) and National Science Foundation (CMMI-1907434). Part of the work is performed at San Diego Nanotechnology Infrastructure (SDNI) of UCSD, a member of the National Nanotechnology Coordinated Infrastructure (NNCI), which is supported by NSF (Grant ECCS-1542148).

Supplementary Information

Scattering elements can strongly affect the fabrication quality of DLP-based 3D printing. Figure 3.S1 shows a comparison between 3D printing of non-scattering material and scattering material under the same fabrication condition. Figure 3.S1a is made of 100% PEGDA (Mn = 575) plus 1% w/V Irgacure 819. Figure 3.S1b is made of 100% PEGDA (Mn = 575), 1% w/V Irgacure 819, and 1% w/V glass microbeads (diameter = 4 μm). The “blood vessel” is hollow in Figure 3.S1a, while it is clogged in Figure 3.S1b due to light scattering.

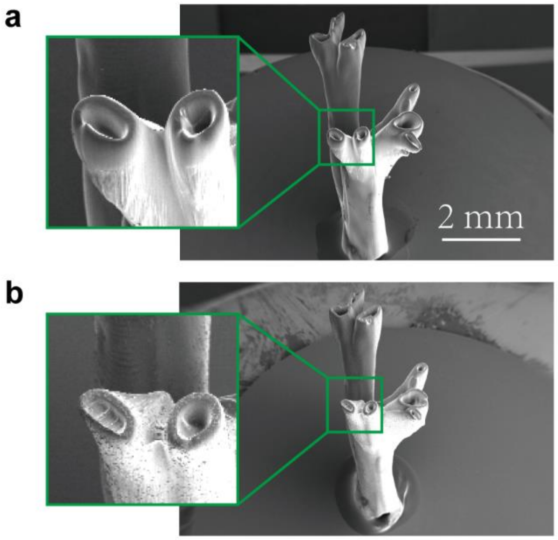

Figure 3.S1| Comparison between 3D printing of non-scattering material and scattering material. a A “blood vessel” structure fabricated with a non-scattering material. **b** A “blood vessel” fabricated with a highly scattering material.

The 300 pairs of digital masks for training are grayscale images of checkerboard shape, disc shapes, and rectangle shapes, as shown in Figure 3.S2. The size, position, and grayscale value of those shapes are all random.

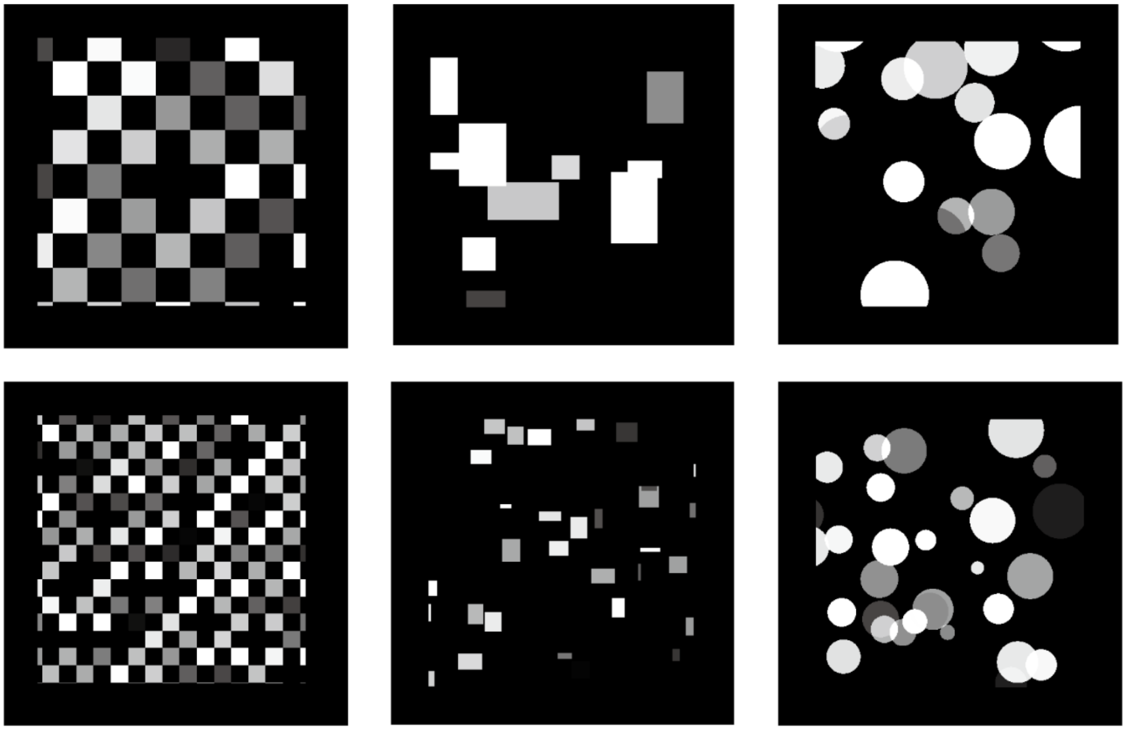

Figure 3.S2| Examples of the training digital masks.

Our ML model consists of two NNs, the master NN and the slave NN. They are trained simultaneously, and the loss function we used is Equation (8), which contains cycle-consistency loss term.

It is quite straight-forward to use only the master NN to perform the same task. In this case, the loss function does not contain cycle-consistency loss term, as Equation (5).

In order to prove the benefit of using our two-NN design, we also did an ablation study with a ML design which only consists of the master NN with the same dataset. Figure 3.S3 compares the performance of these two ML designs. We noticed that the masks generated by the master-only design contains some “ghost images”, which may be due to the poor generalization capability of the master-only design. The contours of the printed structures are shown in the second column, where the white contours are the target, the red ones are the two-NN design, and the cyan ones are the master-only design. We can see that the red contours perform better than the cyan contours. The calculated Chamfer distances also prove that the prints using the master-only design have a greater Chamfer distance than the prints using our two-NN design.

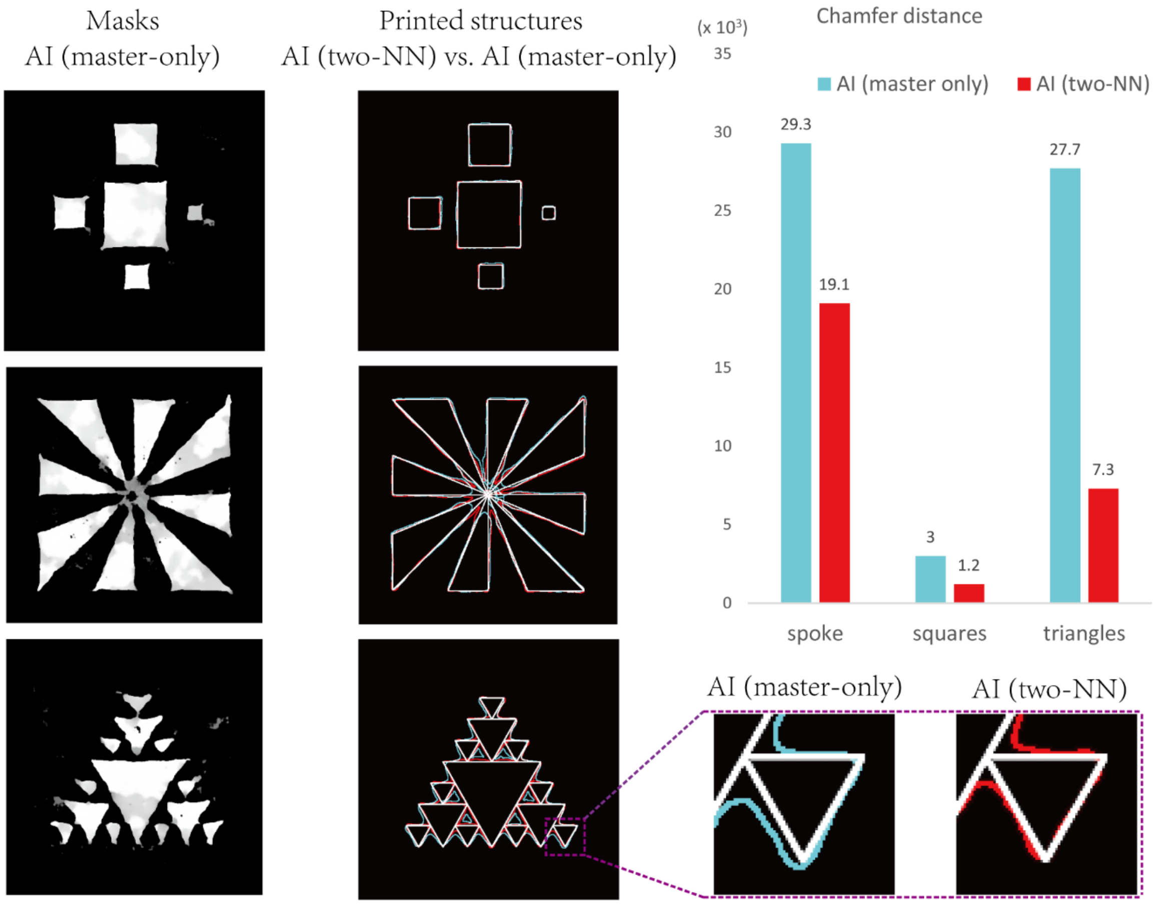

Figure 3.S3| Comparison between the two-NN design and the master-only design. The first column is the masks generated by the master-only design. Those masks generated by the two-NN design can be found in Figure 3.3. The second column is the contours of the printed structures using the two-NN design (red) and the master-only design (cyan), where white contours are the target. The bar chart is the Chamfer distance between the prints using two-NN design and the target (red), and the Chamfer distance between the prints using master-only design and the target (cyan).

The training curve on Figure 3.S4 shows that the network is converging smoothly. We used 33 pairs of test data isolated from the train data to calculate the test errors, and these errors represents that our networks can indeed generalize well on unseen data. Although the error value does not give intuitive results, since the slave NN and master NN errors are calculated differently, we can still find out that the slave NN is converging faster than the master NN. This might prove that the mapping learned by slave NN is a relatively easier transformation compared to what master NN learns.

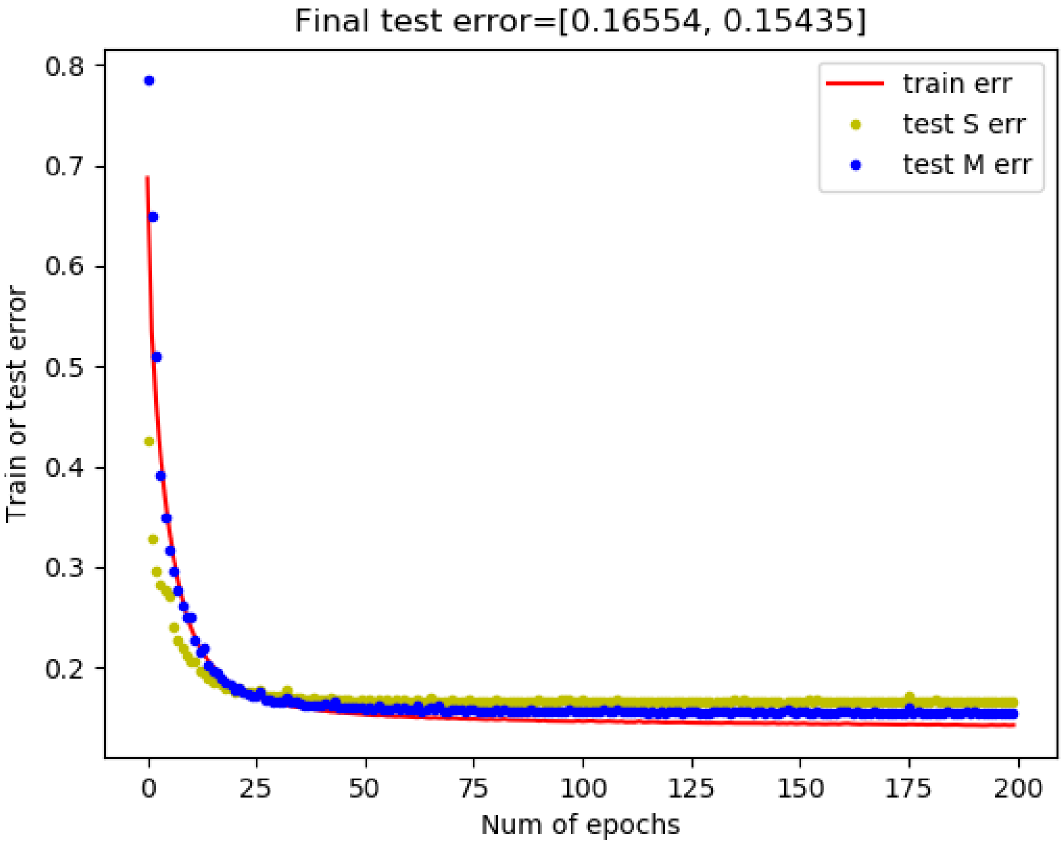

Figure 3.S4| Plot of errors versus episodes. The red line represents the loss calculated for master during training. The yellow and blue dots are errors of slave and master NN calculated using the test set. Final test error shows the value for slave and master NN errors after the last (200) epoch.

Reference

[1] H.H. Hwang, W. Zhu, G. Victorine, N. Lawrence, S. Chen, 3D-Printing of Functional Biomedical Microdevices via Light-and Extrusion-Based Approaches, Small Methods. 2 (2018) 1700277.

[2] W. Zhu, X. Ma, M. Gou, D. Mei, K. Zhang, S. Chen, 3D printing of functional biomaterials for tissue engineering, Current Opinion in Biotechnology. 40 (2016) 103–112.

[3] C. Sun, N. Fang, D.M. Wu, X. Zhang, Projection micro-stereolithography using digital micro-mirror dynamic mask, Sensors and Actuators A: Physical. 121 (2005) 113–120.

[4] A.P. Zhang, X. Qu, P. Soman, K.C. Hribar, J.W. Lee, S. Chen, S. He, Rapid Fabrication of Complex 3D Extracellular Microenvironments by Dynamic Optical Projection Stereolithography, Advanced Materials. 24 (2012) 4266–4270.

[5] J.R. Tumbleston, D. Shirvanyants, N. Ermoshkin, R. Janusziewicz, A.R. Johnson, D. Kelly, K. Chen, R. Pinschmidt, J.P. Rolland, A. Ermoshkin, E.T. Samulski, J.M. DeSimone, Continuous liquid interface production of 3D objects, Science. 347 (2015) 1349–1352.

[6] W. Zhu, X. Qu, J. Zhu, X. Ma, S. Patel, J. Liu, P. Wang, C.S.E. Lai, M. Gou, Y. Xu, K. Zhang, S. Chen, Direct 3D bioprinting of prevascularized tissue constructs with complex microarchitecture, Biomaterials. 124 (2017) 106–115.

[7] X. Ma, X. Qu, W. Zhu, Y.-S. Li, S. Yuan, H. Zhang, J. Liu, P. Wang, C.S.E. Lai, F. Zanella, Deterministically patterned biomimetic human iPSC-derived hepatic model via rapid 3D bioprinting, Proceedings of the National Academy of Sciences. 113 (2016) 2206–2211.

[8] J. Koffler, W. Zhu, X. Qu, O. Platoshyn, J.N. Dulin, J. Brock, L. Graham, P. Lu, J. Sakamoto, M. Marsala, S. Chen, M.H. Tuszynski, Biomimetic 3D-printed scaffolds for spinal cord injury repair, Nature Medicine. 25 (2019) 263–269.

[9] W. Zhu, K.R. Tringale, S.A. Woller, S. You, S. Johnson, H. Shen, J. Schimelman, M. Whitney, J. Steinauer, W. Xu, T.L. Yaksh, Q.T. Nguyen, S. Chen, Rapid continuous 3D printing of customizable peripheral nerve guidance conduits, Mater. Today. 21 (2018) 951–959.

[10] J. Liu, H.H. Hwang, P. Wang, G. Whang, S. Chen, Direct 3D-printing of cell-laden constructs in microfluidic architectures, Lab on a Chip. 16 (2016) 1430–1438.

[11] K. Kim, W. Zhu, X. Qu, C. Aaronson, W.R. McCall, S. Chen, D.J. Sirbuly, 3D optical printing of piezoelectric nanoparticle–polymer composite materials, ACS Nano. 8 (2014) 9799–9806.

[12] W. Zhu, J. Li, Y.J. Leong, I. Rozen, X. Qu, R. Dong, Z. Wu, W. Gao, P.H. Chung, J. Wang, S. Chen, 3D-Printed Artificial Microfish, Advanced Materials. 27 (2015) 4411–4417.

[13] S. You, P. Wang, J. Schimelman, H.H. Hwang, S. Chen, High-fidelity 3D printing using flashing photopolymerization, Additive Manufacturing. 30 (2019) 100834.

[14] T. Wuest, D. Weimer, C. Irgens, K.-D. Thoben, Machine learning in manufacturing: advantages, challenges, and applications, Production & Manufacturing Research. 4 (2016) 23–45.

[15] T. Wang, T.-H. Kwok, C. Zhou, S. Vader, In-situ droplet inspection and closed-loop control system using machine learning for liquid metal jet printing, Journal of Manufacturing Systems. 47 (2018) 83–92.

[16] J.M. Gardner, K.A. Hunt, A.B. Ebel, E.S. Rose, S.C. Zylich, B.D. Jensen, K.E. Wise, E.J. Siochi, G. Sauti, Machines as Craftsmen: Localized Parameter Setting Optimization for Fused Filament Fabrication 3D Printing, Advanced Materials Technologies. (2019) 1800653.

[17] M. Khanzadeh, P. Rao, R. Jafari-Marandi, B.K. Smith, M.A. Tschopp, L. Bian, Quantifying Geometric Accuracy With Unsupervised Machine Learning: Using Self-Organizing Map on Fused Filament Fabrication Additive Manufacturing Parts, Journal of Manufacturing Science and Engineering. 140 (2017) 031011.

[18] P. Isola, J.-Y. Zhu, T. Zhou, A.A. Efros, Image-to-Image Translation with Conditional Adversarial Networks, in: 2017 IEEE Conference on Computer Vision and Pattern Recognition (CVPR), IEEE, Honolulu, HI, 2017: pp. 5967–5976.

[19] O. Ronneberger, P. Fischer, T. Brox, U-Net: Convolutional Networks for Biomedical Image Segmentation, in: N. Navab, J. Hornegger, W.M. Wells, A.F. Frangi (Eds.), Medical Image Computing and Computer-Assisted Intervention – MICCAI 2015, Springer International Publishing, Cham, 2015: pp. 234–241.

[20] J. Long, E. Shelhamer, T. Darrell, Fully Convolutional Networks for Semantic Segmentation, in: 2015: pp. 3431–3440.

[21] S. Ioffe, C. Szegedy, Batch Normalization: Accelerating Deep Network Training by Reducing Internal Covariate Shift, CoRR. abs/1502.03167 (2015).

[22] V. Nair, G.E. Hinton, Rectified Linear Units Improve Restricted Boltzmann Machines, in: Proceedings of the 27th International Conference on International Conference on Machine Learning, n.d.: pp. 807–814.

[23] H. Fan, H. Su, L.J. Guibas, A Point Set Generation Network for 3D Object Reconstruction From a Single Image, in: 2017: pp. 605–613.

[24] T. Zhou, P. Krahenbuhl, M. Aubry, Q. Huang, A.A. Efros, Learning Dense Correspondence via 3D-Guided Cycle Consistency, in: 2016: pp. 117–126.

[25] J.-Y. Zhu, T. Park, P. Isola, A.A. Efros, Unpaired Image-to-Image Translation using Cycle-Consistent Adversarial Networks, ArXiv:1703.10593 [Cs]. (2017).

[26] C. Godard, O. Mac Aodha, G.J. Brostow, Unsupervised Monocular Depth Estimation With Left-Right Consistency, in: 2017: pp. 270–279.

[27] N. Srivastava, G. Hinton, A. Krizhevsky, I. Sutskever, R. Salakhutdinov, Dropout: A Simple Way to Prevent Neural Networks from Overfitting, Journal of Machine Learning Research. 15 (2014) 1929–1958.

[28] A. Krizhevsky, I. Sutskever, G.E. Hinton, ImageNet Classification with Deep Convolutional Neural Networks, in: F. Pereira, C.J.C. Burges, L. Bottou, K.Q. Weinberger (Eds.), Advances in Neural Information Processing Systems 25, Curran Associates, Inc., 2012: pp. 1097–1105.

[29] A. Paszke, S. Gross, S. Chintala, G. Chanan, E. Yang, Z. DeVito, Z. Lin, A. Desmaison, L. Antiga, A. Lerer, Automatic differentiation in PyTorch, (2017).

[30] D.P. Kingma, J. Ba, Adam: A Method for Stochastic Optimization, ArXiv:1412.6980 [Cs]. (2014).

Chapter 4 Projection Printing using Patterned Evanescent Field

Abstract

Spatial control of photon energy has been a central part of many light-based manufacturing processes. We report a direct projection printing method for ultrathin structures with nanoscale thickness control by using a patterned evanescent field. The evanescent field is induced by total internal reflection at the interface between the substrate and a prepolymer solution, and it is patterned by a phase-only spatial light modulator. The ultrathin structure is printed on a high-refractive-index glass substrate through photopolymerization. An iterative algorithm is used to calculate the phase pattern for generating arbitrary holography images and making the image plane to coincide with the interface. The thickness of the pattern is limited by the penetration depth of the evanescent field. Experiment results demonstrated that polymer structures as thin as 200 nanometers can be patterned without significant process optimization. Such fine control in thickness could transform many techniques such as light-based 3D printing and laser direct-write manufacturing.

4.1 Introduction

Light-based fabrication methods such as photolithography,[1] laser direct writing,[2,3] and light projection based 3D printing [4–6] have been playing significant roles in micro- and nano-scale 3D manufacturing in many industrial sectors. Among them, light projection based 3D printing which features fine fabrication resolution and extremely fast fabrication speed has attracted intense research interest.[7,8] The resolution of light projection based 3D printing in lateral direction is determined by the objective lens, which is typically a few microns,[9] and theoretically it can reach the diffraction limit, which is a few hundreds of nanometer. However, its fabrication resolution in the axial direction (along the light propagation direction) cannot match its lateral resolution. The typical axial resolution of light-based 3D printing method ranges from tens to hundreds of microns, depending on the material's light absorption property.[4]

When light propagates in an absorptive medium, it decays exponentially. The axial resolution of light-based 3D printing is determined by the light penetration depth in the photopolymerizable resin. Although doping highly light-absorptive additives does help to improve the axial resolution, the improvement is limited.[8] This has been a bottleneck for 3D printing of finer structures. To address this bottleneck, it is critical to limit the penetration depth of the patterned light field.

When light propagates from one medium to another, it can be partially reflected and partially refracted at the interface. If the first medium has a higher refractive index than the second medium, and the incident angle is greater than the critical angle, the light will be totally reflected back to the first medium. This phenomenon is well known as total internal reflection (TIR).[10] Rigorous solution of Maxwell's equation of electromagnetic wave reveals that, though the light is totally reflected, a thin layer of electromagnetic field still exist in the second medium. This electromagnetic field, named as evanescent field, decays exponentially along the normal direction of the interface, and has a penetration depth at the scale of a wavelength.[10]

This thin evanescent field is very useful in some applications. For example, total internal reflection fluorescence microscopy (TIRFM) [11] uses the evanescent field to excite fluorescence from the specimen. The fluorescence signal comes only from a very thin layer, thus an ultrahigh signal-to-noise ratio can be achieved. Attenuated total reflection infrared spectroscopy (ATR-IR) [12] also uses the evanescent field to measure the infrared absorption spectrum of the samples.

The evanescent field can also be used for fabrication. Periodic patterns in photoresist have been fabricated by the interference of evanescent fields[13–16] or surface plasmonic waves.[17] Although ultrathin patterning can be achieved, arbitrary pattern cannot be generated by these multi-beam interference methods. Metamaterials can be used to manipulate the light field and fabricate ultrathin arbitrary patterning.[18,19] However, using metamaterials will significantly increase the cost and complexity of the system. Laser direct writing technique employs a lens of high numerical aperture to focus the laser beam to achieve a fine resolution. However, the point-scanning process is very time-consuming. Although ~50 nm lateral and ~20 nm axial resolutions has been achieved by femtosecond laser parallel scanning using microlens array on a phase-change film,[20] improvement in the fabrication speed is still limited. The fabricated pattern consists of array of small repeating patterns, and the use of phase-change film compromises the flexibility of this approach. Therefore, a flexible, cost-efficient approach for rapid fabrication of ultrathin arbitrary pattern is highly desired.

In this work, we show that the evanescent field can be patterned through a phase-only spatial light modulator (SLM) and projected to a prepolymer solution for direct printing of designed ultrathin structures. No physical masks is needed, and arbitrary patterns are produced with nanoscale thickness control in a projection fashion within a few seconds of exposure. The lateral resolution is theoretically limited by the diffraction limit. Because this setup requires a relatively long working distance, a high numerical aperture (NA) objective lens cannot be used. For the case of NA = 0.05, the lateral resolution limit is 4 μm. In our experiments, lens aberration dominates because we were using spherical lens instead of aberration-corrected lens, thus the lateral feature size we demonstrated is around 20 microns.

In order to make the image plane coincide with the TIR interface, the image plane cannot be perpendicular to the light incident direction. This tilted image plane is achieved by using holography technique to control the light distribution in 3D. To achieve good image quality and the smooth intensity distribution, we adopt the mixed-region amplitude freedom (MRAF) algorithm [21] to generate an image in a tilted image plane. Various ultrathin patterns with arbitrary shapes are demonstrated.

4.2 Results and Discussion

4.2.1 Polymerization Effect of Evanescent Field

In common light-based fabrication systems, light transmits through the prepolymer resin and gets attenuated exponentially inside the resin due to absorption, according to Beer-Lambert law. The penetration depth of the propagating light field is typically in the range of hundreds of micrometers to a few millimeters at near ultra-violet (350 nm to 400 nm) wavelength.[22] For example, the 0.2% solution of a common photoinitiator, Irgacure 819, in ethonal has a absorbance of 3.0 cm^{-1}. Thus, the penetration depth of 1% Irgacure is calculated as 0.29 mm.

Total internal reflection creates an evanescent field, which decays exponentially. The penetration depth of the evanescent field is given by

$$d = \frac{\lambda}{4\pi}(\mathrm{n}_1^2 \sin^2 \theta_1 - \mathrm{n}_2^2)^{-1/2}, \tag{4.1}$$

where λ is the wavelength, n_1 and n_2 are the refractive indices of the two medias, and θ_1 is the incident angle.

Consider a situation where the refractive indices of the two mediums are 1.85 and 1.4, the wavelength is 400 nm, and the incident angle is 60 °. Then the penetration depth of the evanescent field is 41 nm. Hence, direct patterning with nanoscale thickness control is possible to achieve.

We compared the photopolymerization effect between the propagating field and the evanescent field as shown in Figure 4.1. A 400 nm laser beam was modulated by a SLM and formed a line pattern at the interface between the glass slide and the photopolymerizable resin. Figure 4.1a shows a propagating field interacting with the resin, and Figure 4.1b shows an evanescent field interacting with the resin. The exposure time is 5 seconds for both cases. After exposure, we used isopropanol to remove the uncured resin. Both the glass slide and the equilateral triangular prism used in this experiment have a refractive index of 1.85 (N-SF11 glass). The index-matched medium couples the prism and the glass slide. The photosensitive resin is dipentaerythritol pentaacrylate (DPPA) with 1% Irgacure 819 as the photoinitiator. Figure 4.1c shows a scanning electron microscopy (SEM) image for the patterning result in case (a). Figure 4.1d is an optical profiler image showing the patterning results of case (b). The thickness of the polymer pattern polymerized by the propagating field is around 500 μm, and in comparison, the thickness of the polymer pattern polymerized by the evanescent field is only around 200 nm.

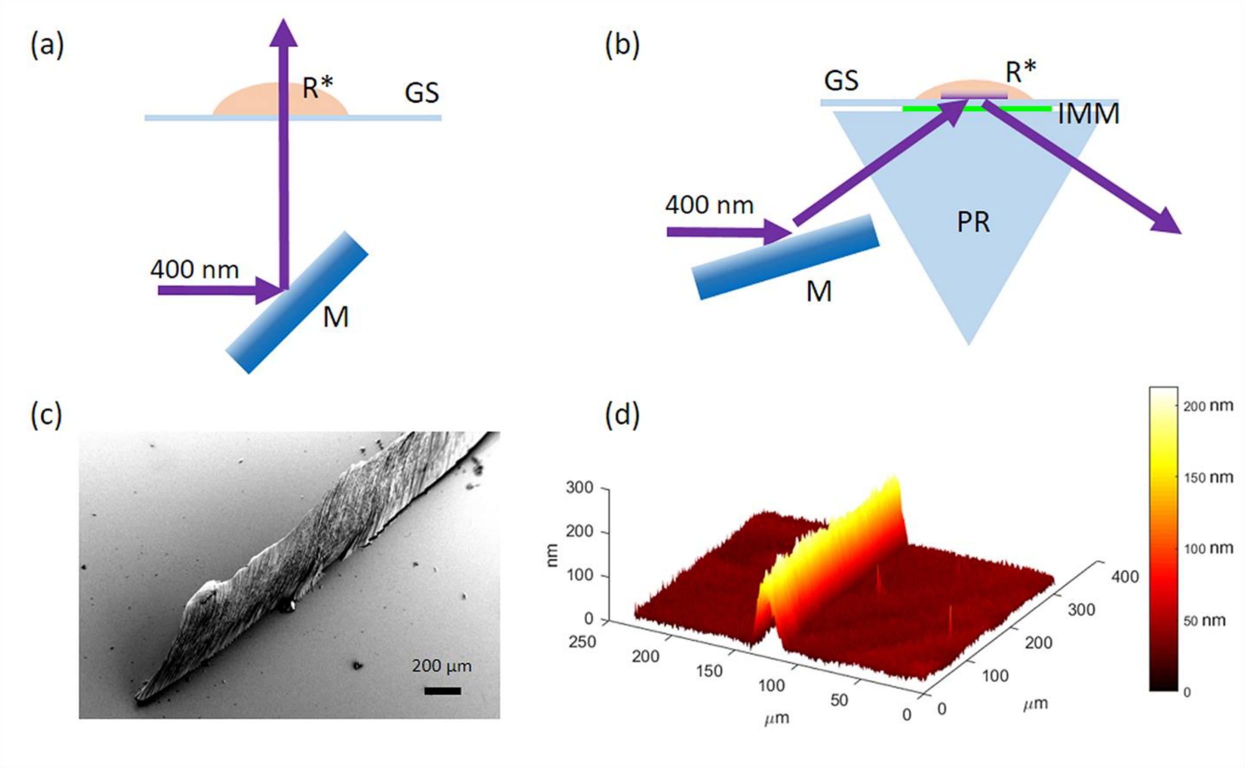

Figure 4.1| Comparison of the polymer pattern thickness between the propagating field and the evanescent field. (a) Schematic showing resin polymerized by the propagating field. (b) Schematic showing resin polymerized by the evanescent field. (c) SEM image of a structure polymerized by the propagating field. (d) Optical profiler image of a structure polymerized by the evanescent field. M: mirror, PR: prism, IMM: index-matched medium, GS: glass slide, R*: photopolymerizable resin.

4.2.2 Direct Printing System Setup

The experimental setup of the ultrathin surface patterning system is shown in Figure 4.2. An ultraviolet laser beam (400 nm, 50 mW) passes through a beam expander and a tunable attenuator, and is modulated by the phase-only SLM. The phase pattern is loaded into the SLM so that the holographic image (intermediate image) can be found near the back focal point of lens *L1*. A diaphragm serves as a spatial filter which only allows the 1st order diffraction image to pass through. Lens *L2* is used to convert the intermediate image to the final image at 1:1 ratio. A mirror is used to redirect the beam so that it passes the prism at a normal incident angle. The equilateral prism is coupled with a glass slide by an index-matched medium. The laser beam irradiates the top surface of the glass slide at an incident angle of 60 °, which leads to TIR. The prepolymer solution on the glass slide is polymerized by the evanescent field from the TIR. A camera is set up above the glass slide to collect the fluorescence excited by evanescent field and to help focusing the final image on the top surface of the glass slide. Note that by using holography method, the intermediate image is tilted by 43.1 °(namely, making a 46.9 °angle to the light propagation direction), and the final image is tilted by 60 ° (namely, making a 30 ° angle to the light propagation direction). Therefore, the final image coincides with the top surface of the glass slide.

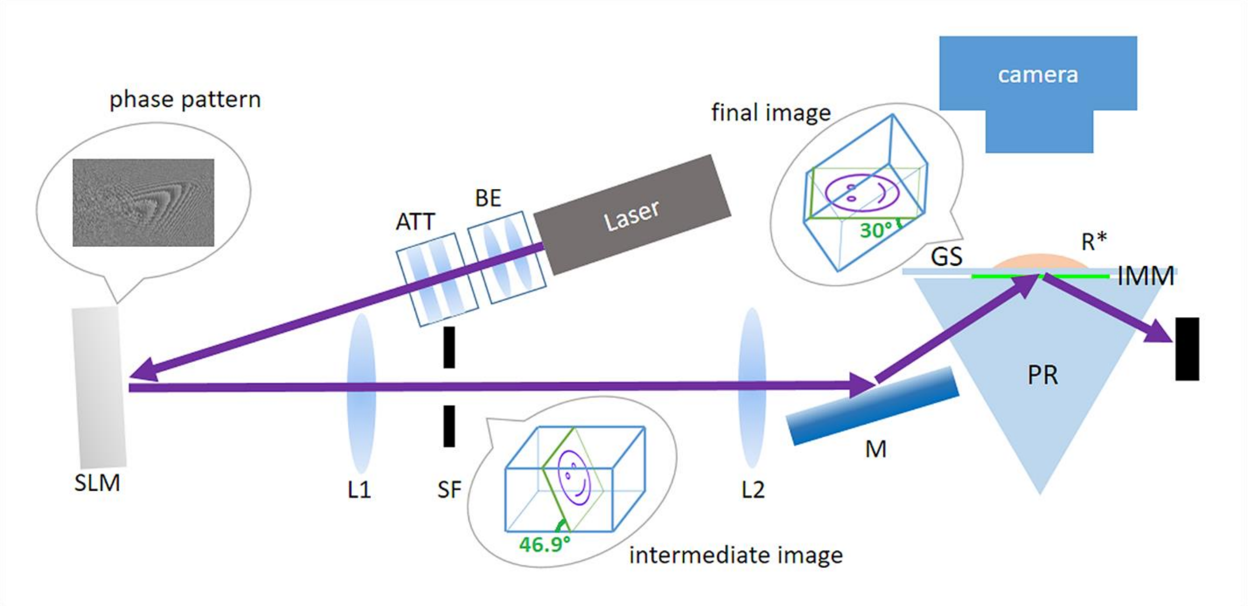

Figure 4.2| The optical setup of the ultrathin surface patterning system. BE: beam expander; ATT: attenuator; SLM: spatial light modulator; L1: lens 1; SF: spatial filter; L2: lens 2; M: mirror; PR: equilateral prism; IMM: index-matched medium; GS: glass slide; R*: photopolymerizable resin.

Both the equilateral prism and the glass slide is made of a high refractive index glass (N-SF11 glass, n = 1.85). An index-matched medium is used to couple the prism and the substrate. Diiodomethane (CH_2I_2) is one of the liquids with the highest known refractive index (n = 1.74) [23], hence it is selected to be the index-matched medium in this work.

The final image should be tilted by 60°. The prism's refractive index is 1.85 at 400 nm wavelength, under paraxial condition, the relation between the tilting angle of the virtual object δ_{obj} and the tilting angle of the final image δ_{img} is $\tan\delta_{img} / \tan\delta_{obj} = n$. Thus, the virtual object of the final image should be tilted by 43.1 °. Since lens *L2* images at 1:1 ratio, the intermediate image should also be tilted by 43.1 °.

This tilted image plane can be achieved by using a tilted lens according to Scheimpflug principle,[24] or by using holography technique to control the light distribution in 3D. We found that a tilted standard spherical lens came with severe aberration, hence a specially designed tilted lens may be required. Therefore, we selected holography method to tilt the image plane.

4.2.3 Holography Algorithm

Iterative Fourier transform algorithms such as Gerchberg–Saxton (GS) algorithm, adaptive-additive (AA) algorithm, and mixed-region amplitude freedom (MRAF) algorithm are commonly used in calculating the phase pattern in computer-generated holography (CGH) .[21,25–29] Among those algorithms, GS algorithm and AA algorithm have shown their capability of shaping the light in 3D .[27,30] However, the intensity profile of the images generated by these algorithms is not smooth. Therefore, multi-exposure by multiple frames of CGH are needed to smoothen the image and to avoid speckles.[31]

MRAF algorithm [21] can achieve better image quality and smoother intensity distribution than other iterative Fourier transform algorithms. Although the original MRAF algorithm can only be applied to creating 2D arbitrary images ,[21] we modified this algorithm so that it is capable of controlling the light distribution in 3D. A 2D image in a tilted plane is fed into the 3D-MRAF algorithm as a 3D target image. The phase pattern can be calculated within half an hour by a common desktop computer.

The key idea of the MRAF algorithm is to divide the image space into a signal region and a noise region. In the signal region, phase freedom is allowed, and the intensity is restricted. In the noise region, both phase freedom and intensity freedom are allowed. In order to extend this idea into a 3D space, we make the 3D signal region as a single layer rectangular sheet (namely, 1 voxel thickness), which contains the target image, and coincides with the tilted image plane (see Figure 4.3: signal region). The rest of the voxels in the image space are noise region.

The schematic of 3D-MRAF algorithm is shown in Figure 4.3. The 3D inclined target image and 3D signal region are first determined according to the desired 2D target. Next, the initial amplitude on the SLM is set to 1 and the initial phase is set as a quadratic function, so that the resulting holography image is a square that covers the signal region.[21] Next, the light field on the SLM is converted into a 3D k-space, and all the non-zero voxels are on the Ewald's surface [27,32] (See Figure 4.3: k-space light field). Then it goes into the iteration.

The iteration is a loop among four complex light fields. Light field U_1 is a 3D light field in the k-space, where non-zero voxels are all on the Ewald's surface. U_1 represents the light field modulated by the SLM. Then the light field U_2 is acquired by applying a 3D Fourier transform to U_1.

Light field U_2 is the holography image of U_1 in image space. U_2 is converted to U_3 by substituting its amplitude with a mixture of its amplitude A_2 and the target A_T (Equation (4.2)). The mixing parameter β is 0 in the noise region, and is a number between 0 and 1 within the signal region.

$$\begin{cases} A_3 = \beta A_T + (1-\beta) A_2 \\ P_3 = P_2 \end{cases} \tag{4.2}$$

Then U_3 is converted to U_4 by applying an inverse Fourier transform.

Light field U_4 is not achievable by an SLM. Therefore, a physical restrain needs to be applied. The amplitude of voxels beyond the Ewald's surface are set to zero, and the amplitude of voxels within the Ewald's surface is set to the initial intensity A_0. The phase of all voxels remain unchanged. By this substitution, we get a new U_1.

This loop is repeated until the maximum count of iteration is met, or the error function between A_2 and A_T is smaller than the threshold. The phase of U_1 is converted back to the 2D space on the SLM: $P_1(x,y)$, which is the output of the algorithm. By using this algorithm, a phase pattern $P_1(x,y)$ can be acquired. The algorithm can be completed within half an hour by a common desktop computer.

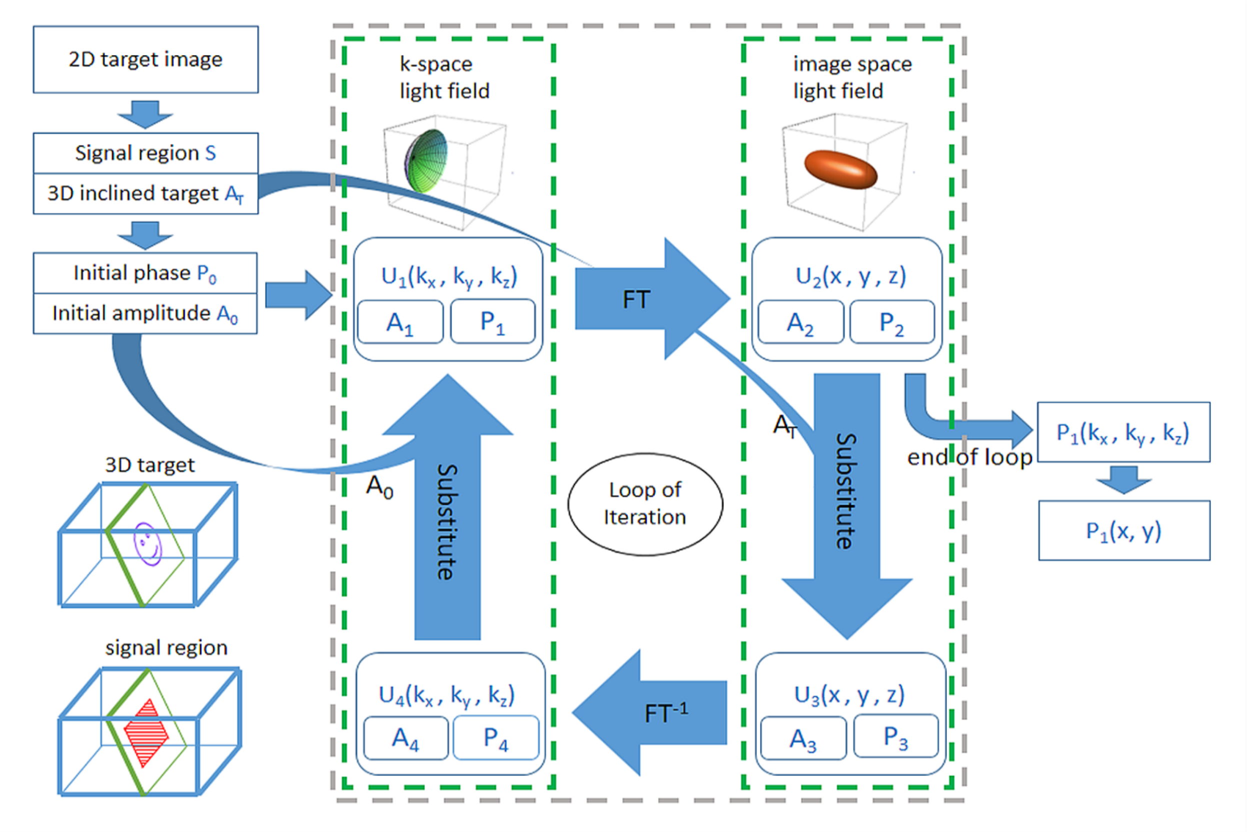

Figure 4.3| Block diagram of the 3D-MRAF algorithm.

4.2.4 Surface Topography of the Printed Patterns

A phase pattern is calculated and loaded on the SLM, then a tilted intermediate image can be formed. The final image is formed at the interface between the glass slide and the prepolymer solution. We used poly(ethelene glycol) diacrylate (PEGDA, Mn = 575) mixed with 1% Irgacure 819 photoinitiator as the prepolymer material. After a few seconds' exposure, ultrathin polymer patterns are formed on the glass slide.

Then we used the optical profiler to measure the surface topography of the patterns. Figures 4.4a and 4.4b show the topographies of a "smiling face". Figures 4.4c and 4.4d show the topography of a "honeycomb". Figure 4.4e and 4.4f show the topographies of a "UCSD" pattern. The thickness of these patterns are around 200 nm.

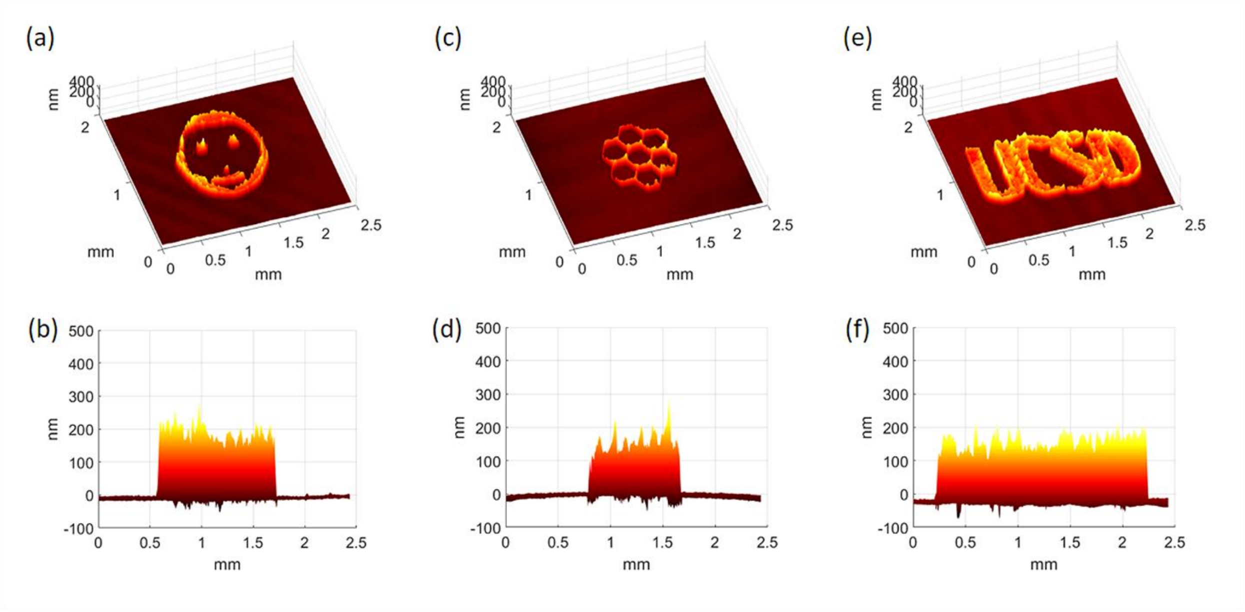

Figure 4.4| The optical profiler images of the patterned structure. (b), (d), and (f) are the side views of (a), (c), and (e), respectively. The thickness of these pattern is around 200 nm.

4.3 Methods

Materias

DPPA was purchased from Sartomer. Irgacure 819 was purchased from Ciba Specialty Chemicals, which is now acquired by BASF. PEGDA was purchased from Sigma Aldrich. CH_2I_2 was purchased from Alfa Aesar. N-SF11 equilateral prism was purchased from Edmund Optics. N-SF11 glass slide was purchased from Volume Precision Glass.

Equipment: The SLM is Holoeye Pluto. The SEM is Zeiss Sigma 500. The optical profiler is Veeco NT1100. The sputter coater is Emitech K575X.

Sample characterization

Samples for SEM imaging were sputter coated by Iridium, then were imaged under 2kV voltage. Samples for optical profiler were imaged without coating. Due to the limitation of the optical profiler which uses white light interference to detect the height profile, height values at steep edges are not able to be detected. In order to make a complete topography, these “bad pixels” are replaced with the average of their surrounding “good pixels”. This processing was performed with Matlab.

Software Program

The program of the 3D-MRAF algorithm was developed by the authors. This program runs in Matlab environment. The light filed is represented by a 1080x1920x128 matrix, thus a computer of 32GB memory can handle this program.

4.4 Conclusions

We have developed a new method that utilizes the patterned evanescent field to create arbitrary structures with nanoscale thickness control without using spin-coating to control the thickness or using a physical photomask for patterning. The phase-only SLM can generate an image that coincides with the TIR interface and prints the structures in a projection fashion. We have demonstrated that arbitrary ultrathin structures as thin as 200 nm can be achieved. However, its lateral resolution is theoretically limited by the diffraction limit. Because this setup requires a relatively long working distance, a high numerical aperture (NA) objective lens cannot be used. Thus, the lateral resolution is limited to a few microns. Due to the aberrations, we could only demonstrate a 20 microns feature size. In order to make the image in-focus on the entire TIR interface, the image plane should not be perpendicular to the light incident direction. The tilted image is generated by the holography method in this work for proof-of-concept purpose. However, the holography method requires an expensive coherent light source. Calculating the phase pattern by the 3D-MRAF algorithm is time-consuming. In practice, it is more favorable to use a tilted lens combined with a digital mirror device (DMD) to pattern the light field. Although the tilted lens needs to be specially designed, better image quality can be achieved, and it does not need the time-consuming algorithm.

Currently two-photon polymerization method is the most popular nanoscale 3D fabrication technique. Although it features extremely fine resolution, its fabrication speed is very slow due to the point-scanning nature.[3] On the other hand, light-projection-based 3D printing methods are facing the bottleneck of poor axial resolution. We expect this evanescent field patterning concept can be applied to light-projection-based 3D printing in the future,[6] offering a fast fabrication speed, sub-micron axial resolution, and micron scale lateral resolution.

Acknowledgements

Chapter 4, in full, is a reprint of the published article, "Projection Printing of Ultrathin Structures with Nanoscale Thickness Control", S. You, W. Zhu, P.Wang, S.Chen. *ACS Applied Materials and Interfaces*, 2019. The dissertation author was the primary investigator and author of this paper. This work was supported in part by National Institutes of Health (R21HD090662, R01EB021857) and National Science Foundation (CMMI-1547005 and CMMI-1644967). Part of the work is performed at San Diego Nanotechnology Infrastructure (SDNI) of UC San Diego, a member of the National Nanotechnology Coordinated Infrastructure (NNCI), which is supported by the National Science Foundation (Grant ECCS-1542148).

Reference

[1] M.J. Madou, Manufacturing Techniques for Microfabrication and Nanotechnology, CRC Press, 2011.

[2] Y. Lu, S.C. Chen, Micro and nano-fabrication of biodegradable polymers for drug delivery, Adv. Drug Deliv. Rev. 56 (2004) 1621–1633.

[3] S. You, J. Li, W. Zhu, C. Yu, D. Mei, S. Chen, Nanoscale 3D printing of hydrogels for cellular tissue engineering, J. Mater. Chem. B. 6 (2018) 2187–2197.

[4] J.R. Tumbleston, D. Shirvanyants, N. Ermoshkin, R. Janusziewicz, A.R. Johnson, D. Kelly, K. Chen, R. Pinschmidt, J.P. Rolland, A. Ermoshkin, E.T. Samulski, J.M. DeSimone, Continuous liquid interface production of 3D objects, Science. 347 (2015) 1349–1352.

[5] A.P. Zhang, X. Qu, P. Soman, K.C. Hribar, J.W. Lee, S. Chen, S. He, Rapid Fabrication of Complex 3D Extracellular Microenvironments by Dynamic Optical Projection Stereolithography, Adv. Mater. 24 (2012) 4266–4270.

[6] B. Lu, H. Lan, H. Liu, Additive manufacturing frontier: 3D printing electronics, Opto-Electron. Adv. 1 (2018) 17000401–17000410.

[7] H.H. Hwang, W. Zhu, G. Victorine, N. Lawrence, S. Chen, 3D-Printing of Functional Biomedical Microdevices via Light-and Extrusion-Based Approaches, Small Methods. 2 (2018) 1700277.

[8] F.P.W. Melchels, J. Feijen, D.W. Grijpma, A review on stereolithography and its applications in biomedical engineering, Biomaterials. 31 (2010) 6121–6130.

[9] W. Zhu, X. Ma, M. Gou, D. Mei, K. Zhang, S. Chen, 3D printing of functional biomaterials for tissue engineering, Curr. Opin. Biotechnol. 40 (2016) 103–112.

[10] M. Born, E. Wolf, Principles of Optics: Electromagnetic Theory of Propagation, Interference and Diffraction of Light, Elsevier, 2013.

[11] K.N. Fish, Total Internal Reflection Fluorescence (TIRF) Microscopy, Curr. Protoc. Cytom. 50 (2009) 12.18.1-12.18.13.

[12] S. G. Kazarian, K.L. Andrew Chan, ATR-FTIR spectroscopic imaging : recent advances and applications to biological systems, Analyst. 138 (2013) 1940–1951.

[13] J.K. Chua, V.M. Murukeshan, S.K. Tan, Q.Y. Lin, Four beams evanescent waves interference lithography for patterning of two dimensional features, Opt. Express. 15 (2007) 3437–3451.

[14] J.C. Martinez-Anton, Surface relief subwavelength gratings by means of total internal reflection evanescent wave interference lithography, J. Opt. Pure Appl. Opt. 8 (2006) S213.

[15] C. Ecoffet, A. Espanet, D.J. Lougnot, Photopolymerization by Evanescent Waves: A New Method to Obtain Nanoparts, Adv. Mater. 10 (1998) 411–414.

[16] Y. Zhou, M.H. Hong, J.Y.H. Fuh, L. Lu, B.S. Lukiyanchuk, Evanescent wave interference lithography for surface nano-structuring, Phys. Scr. T129 (2007) 35–37.

[17] X. Guo, J. Du, Y. Guo, J. Yao, Large-area surface-plasmon polariton interference lithography, Opt. Lett. 31 (2006) 2613–2615.

[18] W. Kong, W. Du, K. Liu, C. Wang, L. Liu, Z. Zhao, X. Luo, Launching deep subwavelength bulk plasmon polaritons through hyperbolic metamaterials for surface imaging with a tuneable ultra-short illumination depth, Nanoscale. 8 (2016) 17030–17038.

[19] L. Liu, K. Liu, Z. Zhao, C. Wang, P. Gao, X. Luo, Sub-diffraction demagnification imaging lithography by hyperlens with plasmonic reflector layer, RSC Adv. 6 (2016) 95973–95978.

[20] Y. Lin, M.H. Hong, T.C. Chong, C.S. Lim, G.X. Chen, L.S. Tan, Z.B. Wang, L.P. Shi, Ultrafast-laser-induced parallel phase-change nanolithography, Appl. Phys. Lett. 89 (2006) 041108.

[21] M. Pasienski, B. DeMarco, A high-accuracy algorithm for designing arbitrary holographic atom traps, Opt. Express. 16 (2008) 2176–2190.

[22] A. del Campo, C. Greiner, SU-8: a photoresist for high-aspect-ratio and 3D submicron lithography, J. Micromechanics Microengineering. 17 (2007) R81–R95.

[23] J.M. Laskar, P. Shravan Kumar, S. Herminghaus, K.E. Daniels, M. Schröter, High refractive index immersion liquid for superresolution 3D imaging using sapphire-based aplanatic numerical aperture increasing lens optics, Appl. Opt. 55 (2016) 3165.

[24] H.M. Merklinger, Focusing the view camera: a scientific way to focus the view camera and estimate depth of field, H.M. Merklinger, Ottawa, Ontario, Canada, 1993.

[25] G.D. Bruce, J. Mayoh, G. Smirne, L. Torralbo-Campo, D. Cassettari, A smooth, holographically generated ring trap for the investigation of superfluidity in ultracold atoms, Phys. Scr. 2011 (2011) 014008.

[26] G. Yang, B. Dong, B. Gu, J. Zhuang, O.K. Ersoy, Gerchberg–Saxton and Yang–Gu algorithms for phase retrieval in a nonunitary transform system: a comparison, Appl. Opt. 33 (1994) 209–218.

[27] S. You, C. Kuang, K.C. Toussaint, R. Zhou, X. Xia, X. Liu, Iterative phase-retrieval method for generating stereo array of polarization-controlled focal spots, Opt. Lett. 40 (2015) 3532.

[28] V.V. Kotlyar, P.G. Seraphimovich, V.A. Soifer, An iterative algorithm for designing diffractive optical elements with regularization, Opt. Lasers Eng. 29 (1998) 261–268.

[29] V.A. Soifer, Methods for computer design of diffractive optical elements, John Wiley & Sons, Inc., 2001.

[30] G. Whyte, J. Courtial, Experimental demonstration of holographic three-dimensional light shaping using a Gerchberg–Saxton algorithm, New J. Phys. 7 (2005) 117.

[31] C. Zhang, Y. Hu, J. Li, Z. Lao, J. Ni, J. Chu, W. Huang, D. Wu, An improved multi-exposure approach for high quality holographic femtosecond laser patterning, Appl. Phys. Lett. 105 (2014) 221104.

[32] G. Shabtay, Three-dimensional beam forming and Ewald's surfaces, Opt. Commun. 226 (2003) 33–37.

Chapter 5 Conclusions and Future Perspectives

5.1 Conclusions

Various methods to improve fabrication fidelity and resolution in photopolymerization-based micro 3D printing via manipulating light-matter interaction are developed.

In Chapter 2, a flashing photopolymerization approach is reported. This method applies to a common scenario where the optically transparent and clear prepolymer solution become optically opaque and scattering after polymerization. In traditional photopolymerization-based 3D printing, the polymerization and the opacification of material occur simultaneously, thus the fabrication is strongly affected by the scattered light. By using flashing photopolymerization, light exposure, polymerization, and opacification are chronologically separated. During the exposure period, the material is not yet opacified, thus resolution deterioration caused by light scattering is avoided. Therefore, the fabrication fidelity and resolution in such material are improved.

In Chapter 3, a machine learning approach is reported. This method applies to a common scenario where functional impurities such as micro/nano particles and cells are doped in the prepolymer solution. These impurities often scatter light and deteriorate fabrication fidelity and resolution. A convolutional neural network is trained to study the relation between the digital photomask and the actual printed structure, and then suggest the optimal photomask for a desired structure. Such NN-suggested photomasks can counterbalance or compensate the effect of light scattering, thus the fabrication fidelity and resolution in such material are improved. Also, the effort spent on optimizing the exposure dose is minimized by using the NN-suggested masks.

In Chapter 4, a printing method using patterned evanescent filed is reported. Though micron scale resolution can be achieved in photopolymerization-based 3D printing, the axial resolution is typically at the scale of a hundred microns. The evanescent field naturally has a very shallow penetration depth, thus can be used to control the curing depth. A method to pattern the evanescent field and induce photopolymerization is reported, where the curing depth is at sub-micron scale. This method can potentially be applied to photopolymerization-based 3D printing, thus greatly improve the axial resolution.

Microscale photopolymerization-based 3D printing techniques are developing rapidly. Various novel methods have been invented in recent years, which have greatly improve the performance of microscale 3D printing.

5.2 Perspectives

In the future, photopolymerization-based 3D printing techniques can evolve in various directions.

High resolution fabrication

High resolution fabrication can enable microdevices in smaller size with better performance. Photonic devices with micron scale feature resolution can only operate at an infrared wavelength. In order to operate at a visible wavelength, sub-micron scale fabrication resolution is necessary. Currently two-photon point-scanning method is the most reliable sub-micron fabrication technique. However, the fabrication speed is slow, and the cost of a femtosecond laser is very high. A low-cost rapid sub-micron scale 3D printing method is highly desired.

High speed and high throughput fabrication

3D printing has been proved to be a good prototyping technique, yet its throughput needs to be further improved for industrial manufacturing. Plane-projection methods and volumetric methods can print much faster than point-scanning methods. Besides, parallel processing approaches using microlens arrays or optical diffractive elements can be another way to improve the throughput of the 3D printing system. [1,2]

3D printing without supporting structures

Supporting structures can improve the mechanical stability during the printing process, and prevent deformation. But these supporting structures can affect the performance of the printed microdevices. Volumetric photopolymerization 3D printing methods can polymerize the whole volume simultaneously, thus supporting structures are not necessary for these methods. However, there are a few issues associated with volumetric photopolymerization methods, such as the "speckle" problem in holography method,[3] and the "soft-edged image" problem in tomography method.[4] More efforts should be paid to the further development of 3D printing methods free of supporting structures.

More material choices

More choices of 3D printing materials can enable more functionality and better performance of the microdevices. Currently most 3D printing materials are polymers. There are only a few reports on 3D printing of other types of materials such as metal, ceramic, and glass.[5,6] These materials can usually have better mechanical, thermal, or electrical performance than polymer materials.

Multi-material 3D printing

Functional microdevices can have multiple types of materials in a construct. A common solution is the “expose-and-flush” method: load material A, expose to light, flush away, load material B, expose to light, flush away… Such “expose-and-flush” cycle is very time-consuming, thus significantly decrease the throughput of the printing system. A multi-wavelength approach to trigger free-radical and cationic photopolymerization orthogonally is recently reported to get rid of this “expose-and-flush” cycle.[7]

Reference

[1] L. Yang, A. El-Tamer, U. Hinze, J. Li, Y. Hu, W. Huang, J. Chu, B.N. Chichkov, Parallel direct laser writing of micro-optical and photonic structures using spatial light modulator, Opt. Lasers Eng. 70 (2015) 26–32.

[2] S. Matsuo, S. Juodkazis, H. Misawa, Femtosecond laser microfabrication of periodic structures using a microlens array, Appl. Phys. A. 80 (2005) 683–685.

[3] M. Shusteff, A.E.M. Browar, B.E. Kelly, J. Henriksson, T.H. Weisgraber, R.M. Panas, N.X. Fang, C.M. Spadaccini, One-step volumetric additive manufacturing of complex polymer structures, Sci. Adv. 3 (2017) eaao5496.

[4] B.E. Kelly, I. Bhattacharya, H. Heidari, M. Shusteff, C.M. Spadaccini, H.K. Taylor, Volumetric additive manufacturing via tomographic reconstruction, Science (80-.). 363 (2019) 1075–1079.

[5] F. Kotz, K. Arnold, W. Bauer, D. Schild, N. Keller, K. Sachsenheimer, T.M. Nargang, C. Richter, D. Helmer, B.E. Rapp, Three-dimensional printing of transparent fused silica glass, Nature. 544 (2017) 337–339.

[6] X. Du, S. Fu, Y. Zhu, 3D printing of ceramic-based scaffolds for bone tissue engineering: an overview, J. Mater. Chem. B. 6 (2018) 4397–4412.

[7] J.J. Schwartz, A.J. Boydston, Multimaterial actinic spatial control 3D and 4D printing, Nat. Commun. 10 (2019) 791.